UNIVERSITY OF CALIFORNIA SAN DIEGO

Stimuli-Responsive Polymers for Actuating Devices

A Dissertation submitted in partial satisfaction of the requirements

for the degree Doctor of Philosophy

in

Materials Science and Engineering

by

Gaoweiang Dong

Committee in charge:

Professor Shengqiang Cai, Chair
Professor Tania Morimoto
Professor Yu Qiao
Professor Michael Tolley

2024

The Dissertation of Gaoweiang Dong is approved, and it is acceptable in quality and form for publication on microfilm and electronically.

University of California San Diego

2024

TABLE OF CONTENTS

LIST OF FIGURES

ACKNOWLEDGEMENTS

To me, a PhD is a journey full of explorations, challenges, efforts, and accomplishments. Many people have played important roles in this journey, and I would like to express my sincere appreciation to them.

Firstly, I would have been nowhere near the goal of the PhD without the advice from Professor Shengqiang Cai. In research, he has always been inspiring me to explore and keep an open mind. In methodology, he has always been training me to be a critical thinker and ask key questions. In life, he has always been supportive of our own decisions and giving good advice. I have learned three things that I value the most from Professor Cai. One is to identify a problem by asking "who cares" and "what's new". The other one is to solve the problem by first breaking down a big problem into many small ones and then prioritizing the most important ones. The last one is to wisely do the experiment by first evaluating the problem using back-of-envelope calculations, and then quickly validating each essential step, finally optimizing each step.

Secondly, I would like to thank Professor Jerry Tustaniwskyj and Professor Huihui Qi whom I had the pleasure to work for nearly 20 academic quarters as a teaching assistant for the MAE senior design class. Professor Tustaniwskyj can always find the most critical problems and evaluate a problem both at a high level and in detail. The communication between us was seamless, and he gave me very good advice in organizing the MAE Senior Day, the end-of-quarter poster event. During my time working with Professor Qi, I made tremendous improvements in teaching and communication professionalism. She worked very hard in providing the best learning experience to the students, and I had many good trainings from her.

Thirdly, I would like to thank all my doctoral dissertation committee members: Professor Tania Morimoto, Professor Yu Qiao, and Professor Michael Tolley for their valuable comments

and suggestions for my research projects. I would also like to thank all my collaborators: Professor Qiguang He, Professor Renkun Chen, Doctor Zhaoqiang Song, Tianshi Feng, Fangchen Zhao, and Zongyu Gao.

Lastly, I would like to thank all the lovely Cai group members and alums, whom I had lots of good discussions with and many unforgettable memories. They are Prof. Qiguang He, Prof. Zhijian Wang, Prof. Yue Zheng, Dr. Zhaoqiang Song, Dr. Yang Wang, Dr. Nada Qari, Dr. Zijun Wang, Dr. Qiang Guo, Chenghai Li, Raja Annapooranan, Robert Chambers, Ram Hemanth Yeerella, Fangchen Zhao, Devyansh Agrawal, Zongyu Gao, and Shengjia Zhang.

Finally, I would like to thank my mother Dr. Xiuhua Gao and father Honglin Dong for their enormous support and my aunt Hongmei Dong, my uncle Dr. Fuqiang Li, my cousin Dr. Jiaxi Li, my cousin Ru Gao. I would also like to thank all my good friends Yicen Yan, Dian Wang, Yihui Zhang, Xinzhi Zou, Zuoqi Zhang, Muning Li, Dr. Jikun Wang, Tao Wang, Dr. Qian Lao, Leiguang Ren, Dr. Sukjun Kim, Dr. Yuhang Fan, Dr. Pengyang Li, Professor Richard N. Zare, Dr. Vijaya Lakshmi Kanchustambham, David Tan, Xiaoxuan Zhang, Zachary Bogard.

Chapter 2, in full, is a reprint of the material as it appears in “Magnetic vitrimer-based soft robotics”, *Soft Matter*, 18.39, 2022, by Gaoweiang Dong, Qiguang He, Shengqiang Cai. The dissertation author was the primary investigator and first author of this paper.

Chapter 3, in full, is a reprint of the material as it appears in “Autonomous thermal modulator based on gold film-coated liquid crystal elastomer”, submitted, by Gaoweiang Dong, Tianshi Feng, Renkun Chen, Shengqiang Cai. The dissertation author was the primary investigator and first author of this paper.

Chapter 4, in full, is a reprint of the material as it appears in “Liquid crystal elastomer for smart compression therapy”, submitted, by Gaoweiang Dong, Fangchen Zhao, Zongyu Gao, Shengqiang Cai. The dissertation author was the primary investigator and first author of this paper.

VITA

2017 Bachelor of Science in Material Chemistry, Beijing Jiaotong University

2019 Master of Science in Materials Science and Engineering, University of California San Diego

2024 Doctor of Philosophy in Materials Science and Engineering, University of California San Diego

PUBLICATIONS

1. **G. Dong**, Q. He, S. Cai, "Magnetic vitrimer-based soft robotics", *Soft Matter*, 18.39, 2022.
2. **G. Dong**, T. Feng, R. Chen, S. Cai, "Autonomous thermal modulator based on gold film-coated liquid crystal elastomer", submitted.
3. **G. Dong**, F. Zhao, Z. Gao, and S. Cai, "Liquid crystal elastomer for smart compression therapy", submitted.
4. Z. Song, **G. Dong**, F. J. Vernerey, S. Cai. "Temperature and rate-dependent fracture in Disulfide vitrimers".

ABSTRACT OF THE DISSERTATION

Stimuli-Responsive Polymers for Actuating Devices

by

Gaoweiang Dong

Doctor of Philosophy in Materials Science and Engineering

University of California San Diego, 2024

Professor Shengqiang Cai, Chair

Actuating devices traditionally rely on rigid components such as links and gears, posing challenges in handling delicate objects and operating in unstructured environments. Advancements in smart materials, particularly stimuli-responsive polymers, offer promising alternatives due to their compliance and controlled mechanical responses to external stimuli. Researchers have made significant progress in exploring stimuli-responsive polymers for actuating devices. These polymers can deform and generate various motions, enabling dynamic functionalities across diverse application areas including robotics, responsive systems, and health care. However, existing materials often present limitations such as high voltage requirements, specific working environments, or slow actuation speeds.

In this dissertation, we first proposed magnetic-responsive vitrimers for soft robotics. These vitrimers incorporate magnetic particles into polymer matrices, enabling controlled deformations and movements in response to magnetic fields. The exchange reaction activity of the dynamic covalent bonds within the vitrimers allows for drastic reconfiguration and self-healing properties. Detailed investigations and experimentation were conducted to demonstrate the feasibility and effectiveness of these vitrimers for soft robotic applications. Secondly, we developed a liquid crystal elastomers-based thermal modulator. The thermal modulators can efficiently alternate between "low thermal resistance" and "high thermal resistance" states in reaction to changes in environmental temperature. The reversible transition induced by the nematic-isotropic phase transition of LCEs enables dynamic adaptation of thermal properties, offering potential applications in energy-efficient building materials and wearable technology necessitating active temperature regulation. Lastly, we studied the application of LCEs for both static and dynamic compression therapy. For static compression stocking, we developed a

polydomain LCE with incorporated PEGDA, exhibiting stress plateau and negligible hysteresis. The LCE-based static stocking accommodates stocking application inconsistencies, various limb sizes, and reduces pressure drop due to leg deswelling. Monodomain LCE was introduced for dynamic compression stockings due to its reversible thermal actuation. The LCE-based dynamic stocking demonstrates intermittent pressure cycles from 20 to 60 mmHg with pressure profile programmability. We further fabricated an untethered and wearable compression device with a Power, Control, Sensing module and batteries, supporting continuous use for up to four hours on a single battery charge.

In summary, this dissertation explores the design, fabrication, and characterization of actuating devices using magnetic-responsive vitrimers and thermal-responsive LCEs. Through comprehensive experimentation and analysis, we demonstrate the versatility and effectiveness of these materials for a range of applications, including soft robotics, thermal management, and compression therapy. We hope our material-based design concept of actuating devices can contribute to various fields, from healthcare to wearable technology.

Chapter 1 Introduction

1.1 Background

The significance of actuating devices lies in their ability to fulfill specific functionalities across diverse applications by effectively converting the mechanical output of actuators into desired actions. These devices are widely employed in fields such as robotics[1], responsive systems[2], and healthcare[3], where adaptability and responsiveness are essential. Traditionally, actuating devices are composed of rigid components such as links and gears, which pose challenges in handling delicate objects and working under unconstructed environments.

In the past few decades, advancements have been made in smart materials to construct actuating devices[4,5]. Stimuli-responsive polymers, characterized by their compliance and ability to exhibit controlled mechanical responses to external stimuli, offer unique advantages over traditional rigid materials. For example, they are capable of deforming and generating various motions such as bending[6], elongation[7], and torsion[8] due to their mechanical response and compliance, enabling actuating devices to achieve dynamic and adaptive functionalities across diverse application areas. Various stimuli-responsive polymers and deformable structures have been explored to address the complexities of modern applications. For instance, electroactive polymers (EAP) such as dielectric elastomer actuators can generate large deformation when high voltage is applied[9]. Light-responsive hydrogels exhibit light-induced volume shrinkage along with rapid recovery[10]. PH-responsive hydrogels show reversible actuation upon varying pH and ionic strength[11]. Humidity-responsive bilayer structures shrink in the lengthwise direction in response to the change in humidity[12]. Despite the considerable success in applying these

materials and structures, several limitations have been acknowledged. For instance, the actuation of EAP often requires high voltages at thousands of volts, which may pose potential safety risks. The PH-responsive and humidity-responsive materials require specific working environments and the actuation speed is based on diffusion speed, which is always slow.

In this thesis, we addressed the above challenges in the scope of materials science and engineering, which focuses on the relationship between structure and properties. We first identify a problem that requires certain properties of the material. And then design the structure of the material to endow the properties. Using the problem of slow response time as an example, the magnetic-responsive material can address the problem and its bandwidth can reach up to tens of hertz[13]. Therefore, a magnetic-responsive material can be developed by incorporating magnetic-responsive particles into the polymer matrix. Using a similar strategy, we identified thermal-responsive polymer as the solution to the problem of limited working environments, where it can accommodate various terrains.

1.2 Magnetic-responsive Vitrimers overview

To enhance the efficiency of magnetic-responsive materials, incorporating polymer materials with magnetic particles has emerged as a particularly appealing and effective strategy[14]. Magnetic particles, typically composed of inorganic matter such as iron oxide (Fe_3O_4) or Neodymium (NdFeB), exhibit significantly larger magnetic moments compared to the magnetic response of molecules[15]. This characteristic enables them to respond to weak stimuli, such as static or alternating magnetic fields, with notable effects, including movement, heat

generation, and magnetic or optical signal production[16]. The resulting composites, are referred to as "magnetic responsive polymers ".

The combination of magnetic particles with polymer materials yields diverse material properties. Firstly, when magnetic particles are integrated into an elastomeric polymer matrix, the resulting materials facilitate controlled deformations such as stretching or contraction of cylindrical structures, bending of elongated samples, chaining of microparticles, or rotation of anisotropic objects. Secondly, materials comprising viscous fluid matrices have garnered attention for applications in magnetic guidance and separation, including sorting and separation tasks[17]. In such cases, a magnetic field gradient is applied at specific locations close to the material and a magnetic gradient-induced pulling exerts on the material.

Extensive research has been conducted on both elastomer-based and fluid-based magnetic soft actuators; however, each type exhibits specific limitations. Elastomer-based magnetic actuators typically demonstrate small actuation strains[18], whereas most fluid-based magnetic actuators exhibit irreversible actuation[19]. To integrate the favorable characteristics of both elastomer-based and fluid-based actuators, researchers have utilized polymer matrices containing dynamic covalent bonds. These bonds enable the network to rearrange under specific stimuli, such as heat and ultraviolet (UV) irradiation[20,21].

Vitrimers are characterized by the dynamic covalent bond in their polymer network. Dynamic covalent bonds have been studied through numerous examples in literature[22–24]. These examples explore different covalent bonds, investigating their potential to modify the structure of

polymer backbones. Among the various applications of reversible chemistry, the concept of self-healing materials stands out as particularly appealing. Such materials possess the remarkable ability to auto-repair and restore their original properties[25,26]. Notably, covalent networks offer the material with enhanced mechanical strength and stability compared to non-covalent interactions, such as hydrogen bonds[27], π–π stacking[28], or metal–ion interactions[29].

Among various dynamic covalent bonds, disulfide bonds emerge as promising candidates for introducing healing functionality at lower temperatures while maintaining a reasonable level of bond strength. The dynamics and reversibility of S–S bond cleavage, leading to the generation of sulfenyl radicals, make disulfide compounds crucial in various fields such as synthetic chemistry and material science[30,31].

1.3 Thermal-responsive liquid crystal elastomers (LCEs) overview

Liquid Crystal Elastomer (LCE), comprising liquid crystal mesogens and polymer networks, has been extensively studied and developed due to its unique mechanical and thermomechanical properties. These include anisotropic mechanical characteristics, large and reversible actuation, optical properties, adhesion properties, and damping properties, offering versatile applications ranging from artificial muscles[32] to biomimetic structures[33] and soft robotics[34]. Recent advancements in LCE research have focused on its reversible actuation mechanism, which is intricately linked to the order-disorder arrangement of mesogens at the microscopic level. The LCE transits from a nematic state where liquid crystal mesogens are well-aligned to an isotropic state where the mesogens are randomly distributed under external stimuli such as heat[35], light[36], or chemicals[37]. LCE research is currently experiencing a resurgence, with

significant progress in material synthesis, structural design, and potential applications, from both scientific and engineering perspectives.

The fabrication of LCE involves two-step polymerization. Loosely crosslinked polymer networks are initially formed through a first crosslinking process. Subsequently, external mechanical stretch is applied to the loosely crosslinked LCE to reorient the arrangement of mesogens. Following this, the sample undergoes a second crosslinking process to fix the arrangement of mesogens[38]. Typically, the alignment of mesogens in the two-step polymerization process remains straightforward, although recent studies have explored techniques such as employing inhomogeneous stretching methods, such as the 3D printing of LCE that creates programmable mesogen alignment in a 2D plane[39,40]. The LCE can be fabricated in a monodomain state where the liquid crystal mesogens are fixed in an aligned state, or in a polydomain state where the liquid crystal mesogens are fixed and randomly aligned.

Monodomain LCE exhibits thermal-responsive behavior and demonstrates reversible actuation. As the temperature of LCE surpasses the nematic-isotropic transition temperature, freestanding LCE can undergo up to a 40% actuation strain[41,42]. Additionally, when the displacement of LCE is fixed, it generates actuation stress with increasing temperature. Joule heating serves as a direct method to induce the nematic-isotropic phase transition of LCE, with various approaches explored in prior studies to supply the necessary heat absorption. These methods include embedding heating elements and designing vascular architectures, with embedding flexible, stretchable heating wires, or conductive inks into LCE offering a

straightforward means to provide Joule heat, enabling programmability, locomotion, and compact design[43,44].

The mechanical properties of polydomain LCE can be altered by increasing temperature. Below the phase transition temperature, a stress plateau is observed on the stress-strain curve of LCE, owing to its soft elasticity. As the temperature surpasses the phase transition threshold, LCE transitions into an amorphous state, behaving like rubber, and the stress plateau disappears.

The nematic-isotropic transition temperature of LCE can be adjusted by changing its chemical composition. This can be achieved through various strategies, such as changing the liquid crystal mesogen[45], adjusting the crosslinking density of the LCE[46], or incorporating a flexible backbone into the polymer network[47]. Such tunability of LCE presents numerous opportunities for applications at human-compatible temperatures, particularly in biomedical devices.

1.4 Dissertation structure

The objective of my dissertation is to design and fabricate actuating devices by employing stimuli-responsive polymers. We first described the design and fabrication process of vitrimer-based magnetic-responsive actuating devices and LCE-based thermal-responsive actuating devices. And then characterized their performance. This dissertation is organized as follows:

Chapter 1: discuss the background of stimuli-responsive polymers to construct actuating devices. Chapter 2: describe how to construct a vitrimer-based magnetic-responsive actuating device for soft robotics. Chapter 3: describes how to construct an LCE-based thermal-responsive

actuating device for autonomous thermal modulation. Chapter 4: describes how to construct a LCE-based thermal-responsive actuating device for compression therapy.

Chapter 5: Summarizes the dissertation and discusses future works.

1.5 Reference

(1) Wang, L.; Iida, F. Deformation in Soft-Matter Robotics: A Categorization and Quantitative Characterization. *IEEE Robot. Automat. Mag.* **2015**, *22* (3), 125–139. https://doi.org/10.1109/MRA.2015.2448277.

(2) Laschi, C.; Mazzolai, B.; Cianchetti, M. Soft Robotics: Technologies and Systems Pushing the Boundaries of Robot Abilities. *Sci. Robot.* **2016**, *1* (1), eaah3690. https://doi.org/10.1126/scirobotics.aah3690.

(3) Hao, Y.; Zhang, S.; Fang, B.; Sun, F.; Liu, H.; Li, H. A Review of Smart Materials for the Boost of Soft Actuators, Soft Sensors, and Robotics Applications. *Chin. J. Mech. Eng.* **2022**, *35* (1), 37. https://doi.org/10.1186/s10033-022-00707-2.

(4) Chen, Z.-J.; Gao, F.; Pan, Y. Novel Door-Opening Method for Six-Legged Robots Based on Only Force Sensing. *Chin. J. Mech. Eng.* **2017**, *30* (5), 1227–1238. https://doi.org/10.1007/s10033-017-0172-7.

(5) Carpentier, J.; Mansard, N. Multicontact Locomotion of Legged Robots. *IEEE Trans. Robot.* **2018**, *34* (6), 1441–1460. https://doi.org/10.1109/TRO.2018.2862902.

(6) Shian, S.; Bertoldi, K.; Clarke, D. R. Dielectric Elastomer Based "Grippers" for Soft Robotics. *Advanced Materials* **2015**, *27* (43), 6814–6819. https://doi.org/10.1002/adma.201503078.

(7) Mazzolai, B.; Margheri, L.; Cianchetti, M.; Dario, P.; Laschi, C. Soft-Robotic Arm Inspired by the Octopus: II. From Artificial Requirements to Innovative Technological Solutions. *Bioinspir. Biomim.* **2012**, *7* (2), 025005. https://doi.org/10.1088/1748-3182/7/2/025005.

(8) Shen, Q.; Wang, T.; Liang, J.; Wen, L. Hydrodynamic Performance of a Biomimetic Robotic Swimmer Actuated by Ionic Polymer–Metal Composite. *Smart Mater. Struct.* **2013**, *22* (7), 075035. https://doi.org/10.1088/0964-1726/22/7/075035.

(9) Keplinger, C.; Sun, J.-Y.; Foo, C. C.; Rothemund, P.; Whitesides, G. M.; Suo, Z. Stretchable, Transparent, Ionic Conductors. *Science* **2013**, *341* (6149), 984–987. https://doi.org/10.1126/science.1240228.

(10) Lee, E.; Kim, D.; Kim, H.; Yoon, J. Photothermally Driven Fast Responding Photo-Actuators Fabricated with Comb-Type Hydrogels and Magnetite Nanoparticles. *Sci Rep* **2015**, *5* (1), 15124. https://doi.org/10.1038/srep15124.

(11) Bassik, N.; Abebe, B. T.; Laflin, K. E.; Gracias, D. H. Photolithographically Patterned Smart Hydrogel Based Bilayer Actuators. *Polymer* **2010**, *51* (26), 6093–6098. https://doi.org/10.1016/j.polymer.2010.10.035.

(12) Shin, B.; Ha, J.; Lee, M.; Park, K.; Park, G. H.; Choi, T. H.; Cho, K.-J.; Kim, H.-Y. Hygrobot: A Self-Locomotive Ratcheted Actuator Powered by Environmental Humidity. *Sci. Robot.* **2018**, *3* (14), eaar2629. https://doi.org/10.1126/scirobotics.aar2629.

(13) Poojary, U. R.; Gangadharan, K. V. Material Modeling of Frequency, Magnetic Field and Strain Dependent Response of Magnetorheological Elastomer. *J Mater Sci* **2021**, *56* (28), 15752–15766. https://doi.org/10.1007/s10853-021-06307-0.
(14) Dong, G.; He, Q.; Cai, S. Magnetic Vitrimer-Based Soft Robotics. *Soft Matter* **2022**, *18* (39), 7604–7611. https://doi.org/10.1039/D2SM00893A.
(15) De Gennes, P.; Hébert, M.; Kant, R. Artificial Muscles Based on Nematic Gels. *Macromolecular Symposia* **1997**, *113* (1), 39–49. https://doi.org/10.1002/masy.19971130107.
(16) Brazel, C. S. Magnetothermally-Responsive Nanomaterials: Combining Magnetic Nanostructures and Thermally-Sensitive Polymers for Triggered Drug Release. *Pharm Res* **2009**, *26* (3), 644–656. https://doi.org/10.1007/s11095-008-9773-2.
(17) Thévenot, J.; Oliveira, H.; Sandre, O.; Lecommandoux, S. Magnetic Responsive Polymer Composite Materials. *Chem. Soc. Rev.* **2013**, *42* (17), 7099. https://doi.org/10.1039/c3cs60058k.
(18) Kuang, X.; Wu, S.; Ze, Q.; Yue, L.; Jin, Y.; Montgomery, S. M.; Yang, F.; Qi, H. J.; Zhao, R. Magnetic Dynamic Polymers for Modular Assembling and Reconfigurable Morphing Architectures. *Advanced Materials* **2021**, *33* (30), 2102113. https://doi.org/10.1002/adma.202102113.
(19) Kim, Y.; Yuk, H.; Zhao, R.; Chester, S. A.; Zhao, X. Printing Ferromagnetic Domains for Untethered Fast-Transforming Soft Materials. *Nature* **2018**, *558* (7709), 274–279. https://doi.org/10.1038/s41586-018-0185-0.
(20) Cheng, Y.; Chan, K. H.; Wang, X.-Q.; Ding, T.; Li, T.; Zhang, C.; Lu, W.; Zhou, Y.; Ho, G. W. A Fast Autonomous Healing Magnetic Elastomer for Instantly Recoverable, Modularly Programmable, and Thermorecyclable Soft Robots. *Advanced Functional Materials* **2021**, *31* (32), 2101825. https://doi.org/10.1002/adfm.202101825.
(21) Matxain, J. M.; Asua, J. M.; Ruipérez, F. Design of New Disulfide-Based Organic Compounds for the Improvement of Self-Healing Materials. *Phys. Chem. Chem. Phys.* **2016**, *18* (3), 1758–1770. https://doi.org/10.1039/C5CP06660C.
(22) Maeda, T.; Otsuka, H.; Takahara, A. Dynamic Covalent Polymers: Reorganizable Polymers with Dynamic Covalent Bonds. *Progress in Polymer Science* **2009**, *34* (7), 581–604. https://doi.org/10.1016/j.progpolymsci.2009.03.001.
(23) Ruff, Y.; Lehn, J. Glycodynamers: Dynamic Analogs of Arabinofuranoside Oligosaccharides. *Biopolymers* **2008**, *89* (5), 486–496. https://doi.org/10.1002/bip.20885.
(24) Otsuka, H.; Muta, T.; Sakada, M.; Maeda, T.; Takahara, A. Scrambling Reaction between Polymers Prepared by Step-Growth and Chain-Growth Polymerizations: Macromolecular Cross-Metathesis between 1,4-Polybutadiene and Olefin-Containing Polyester. *Chem. Commun.* **2009**, No. 9, 1073. https://doi.org/10.1039/b818014h.
(25) Guimard, N. K.; Oehlenschlaeger, K. K.; Zhou, J.; Hilf, S.; Schmidt, F. G.; Barner-Kowollik, C. Current Trends in the Field of Self-Healing Materials. *Macro Chemistry & Physics* **2012**, *213* (2), 131–143. https://doi.org/10.1002/macp.201100442.
(26) Bergman, S. D.; Wudl, F. Mendable Polymers. *J. Mater. Chem.* **2008**, *18* (1), 41–62. https://doi.org/10.1039/B713953P.
(27) Cordier, P.; Tournilhac, F.; Soulié-Ziakovic, C.; Leibler, L. Self-Healing and Thermoreversible Rubber from Supramolecular Assembly. *Nature* **2008**, *451* (7181), 977–980. https://doi.org/10.1038/nature06669.

(28) Burattini, S.; Colquhoun, H. M.; Fox, J. D.; Friedmann, D.; Greenland, B. W.; Harris, P. J. F.; Hayes, W.; Mackay, M. E.; Rowan, S. J. A Self-Repairing, Supramolecular Polymer System: Healability as a Consequence of Donor–Acceptor π–π Stacking Interactions. *Chem. Commun.* **2009**, No. 44, 6717. https://doi.org/10.1039/b910648k.
(29) Burnworth, M.; Tang, L.; Kumpfer, J. R.; Duncan, A. J.; Beyer, F. L.; Fiore, G. L.; Rowan, S. J.; Weder, C. Optically Healable Supramolecular Polymers. *Nature* **2011**, *472* (7343), 334–337. https://doi.org/10.1038/nature09963.
(30) Ritz, D.; Beckwith, J. Roles of Thiol-Redox Pathways in Bacteria. *Annu. Rev. Microbiol.* **2001**, *55* (1), 21–48. https://doi.org/10.1146/annurev.micro.55.1.21.
(31) Wedemeyer, W. J.; Welker, E.; Narayan, M.; Scheraga, H. A. Disulfide Bonds and Protein Folding. *Biochemistry* **2000**, *39* (15), 4207–4216. https://doi.org/10.1021/bi992922o.
(32) Spillmann, C. M.; Naciri, J.; Martin, B. D.; Farahat, W.; Herr, H.; Ratna, B. R. Stacking Nematic Elastomers for Artificial Muscle Applications. *Sensors and Actuators A: Physical* **2007**, *133* (2), 500–505. https://doi.org/10.1016/j.sna.2006.04.045.
(33) Zeng, H.; Wani, O. M.; Wasylczyk, P.; Kaczmarek, R.; Priimagi, A. Self-Regulating Iris Based on Light-Actuated Liquid Crystal Elastomer. *Advanced Materials* **2017**, *29* (30), 1701814. https://doi.org/10.1002/adma.201701814.
(34) Rogóż, M.; Zeng, H.; Xuan, C.; Wiersma, D. S.; Wasylczyk, P. Light-Driven Soft Robot Mimics Caterpillar Locomotion in Natural Scale. *Advanced Optical Materials* **2016**, *4* (11), 1689–1694. https://doi.org/10.1002/adom.201600503.
(35) Ahn, C.; Liang, X.; Cai, S. Inhomogeneous Stretch Induced Patterning of Molecular Orientation in Liquid Crystal Elastomers. *Extreme Mechanics Letters* **2015**, *5*, 30–36. https://doi.org/10.1016/j.eml.2015.09.007.
(36) Bisoyi, H. K.; Li, Q. Light-Driven Liquid Crystalline Materials: From Photo-Induced Phase Transitions and Property Modulations to Applications. *Chem. Rev.* **2016**, *116* (24), 15089–15166. https://doi.org/10.1021/acs.chemrev.6b00415.
(37) Boothby, J. M.; Kim, H.; Ware, T. H. Shape Changes in Chemoresponsive Liquid Crystal Elastomers. *Sensors and Actuators B: Chemical* **2017**, *240*, 511–518. https://doi.org/10.1016/j.snb.2016.09.004.
(38) Yakacki, C. M.; Saed, M.; Nair, D. P.; Gong, T.; Reed, S. M.; Bowman, C. N. Tailorable and Programmable Liquid-Crystalline Elastomers Using a Two-Stage Thiol–Acrylate Reaction. *RSC Adv.* **2015**, *5* (25), 18997–19001. https://doi.org/10.1039/C5RA01039J.
(39) Kotikian, A.; Truby, R. L.; Boley, J. W.; White, T. J.; Lewis, J. A. 3D Printing of Liquid Crystal Elastomeric Actuators with Spatially Programed Nematic Order. *Advanced Materials* **2018**, *30* (10), 1706164. https://doi.org/10.1002/adma.201706164.
(40) Wang, Z.; Wang, Z.; Zheng, Y.; He, Q.; Wang, Y.; Cai, S. Three-Dimensional Printing of Functionally Graded Liquid Crystal Elastomer. *Sci. Adv.* **2020**, *6* (39), eabc0034. https://doi.org/10.1126/sciadv.abc0034.
(41) He, Q.; Wang, Z.; Wang, Y.; Song, Z.; Cai, S. Recyclable and Self-Repairable Fluid-Driven Liquid Crystal Elastomer Actuator. *ACS Appl. Mater. Interfaces* **2020**, *12* (31), 35464–35474. https://doi.org/10.1021/acsami.0c10021.
(42) He, Q.; Wang, Z.; Song, Z.; Cai, S. Bioinspired Design of Vascular Artificial Muscle. *Adv Materials Technologies* **2019**, *4* (1), 1800244. https://doi.org/10.1002/admt.201800244.
(43) He, Q.; Wang, Z.; Wang, Y.; Minori, A.; Tolley, M. T.; Cai, S. Electrically Controlled Liquid Crystal Elastomer–Based Soft Tubular Actuator with Multimodal Actuation. *Sci. Adv.* **2019**, *5* (10), eaax5746. https://doi.org/10.1126/sciadv.aax5746.

(44) Wang, C.; Sim, K.; Chen, J.; Kim, H.; Rao, Z.; Li, Y.; Chen, W.; Song, J.; Verduzco, R.; Yu, C. Soft Ultrathin Electronics Innervated Adaptive Fully Soft Robots. *Advanced Materials* **2018**, *30* (13), 1706695. https://doi.org/10.1002/adma.201706695.
(45) Bauman, G. E.; McCracken, J. M.; White, T. J. Actuation of Liquid Crystalline Elastomers at or Below Ambient Temperature. *Angew Chem Int Ed* **2022**, *61* (28), e202202577. https://doi.org/10.1002/anie.202202577.
(46) McCracken, J. M.; Donovan, B. R.; Lynch, K. M.; White, T. J. Molecular Engineering of Mesogenic Constituents Within Liquid Crystalline Elastomers to Sharpen Thermotropic Actuation. *Adv Funct Materials* **2021**, *31* (16), 2100564. https://doi.org/10.1002/adfm.202100564.
(47) Shaha, R. K.; Torbati, A. H.; Frick, C. P. BODY-TEMPERATURE S HAPE-SHIFTING Liquid Crystal Elastomers. *J of Applied Polymer Sci* **2021**, *138* (14), 50136. https://doi.org/10.1002/app.50136.
(48) Sui, C.; Pu, J.; Chen, T.-H.; Liang, J.; Lai, Y.-T.; Rao, Y.; Wu, R.; Han, Y.; Wang, K.; Li, X.; Viswanathan, V.; Hsu, P.-C. Dynamic Electrochromism for All-Season Radiative Thermoregulation. *Nat Sustain* **2023**, *6* (4), 428–437. https://doi.org/10.1038/s41893-022-01023-2.
(49) Tang, K.; Dong, K.; Li, J.; Gordon, M. P.; Reichertz, F. G.; Kim, H.; Rho, Y.; Wang, Q.; Lin, C.-Y.; Grigoropoulos, C. P.; Javey, A.; Urban, J. J.; Yao, J.; Levinson, R.; Wu, J. Temperature-Adaptive Radiative Coating for All-Season Household Thermal Regulation. *Science* **2021**, *374* (6574), 1504–1509. https://doi.org/10.1126/science.abf7136.
(50) *Radiative human body cooling by nanoporous polyethylene textile | Science*. https://www.science.org/doi/10.1126/science.aaf5471 (accessed 2024-02-15).
(51) Wei, H.; Gu, J.; Ren, F.; Zhang, L.; Xu, G.; Wang, B.; Song, S.; Zhao, J.; Dou, S.; Li, Y. Smart Materials for Dynamic Thermal Radiation Regulation. *Small* **2021**, *17* (35), 2100446. https://doi.org/10.1002/smll.202100446.
(52) Ulpiani, G.; Ranzi, G.; Shah, K. W.; Feng, J.; Santamouris, M. On the Energy Modulation of Daytime Radiative Coolers: A Review on Infrared Emissivity Dynamic Switch against Overcooling. *Solar energy* **2020**, *209*, 278–301.
(53) Kats, M. A.; Sharma, D.; Lin, J.; Genevet, P.; Blanchard, R.; Yang, Z.; Qazilbash, M. M.; Basov, D. N.; Ramanathan, S.; Capasso, F. Ultra-Thin Perfect Absorber Employing a Tunable Phase Change Material. *Applied Physics Letters* **2012**, *101* (22), 221101. https://doi.org/10.1063/1.4767646.
(54) Zeng, S.; Shen, K.; Liu, Y.; Chooi, A. P.; Smith, A. T.; Zhai, S.; Chen, Z.; Sun, L. Dynamic Thermal Radiation Modulators via Mechanically Tunable Surface Emissivity. *Materials Today* **2021**, *45*, 44–53. https://doi.org/10.1016/j.mattod.2020.12.001.
(55) Schultz, P. H.; Hermalyn, B.; Colaprete, A.; Ennico, K.; Shirley, M.; Marshall, W. S. The LCROSS Cratering Experiment. *Science* **2010**, *330* (6003), 468–472. https://doi.org/10.1126/science.1187454.
(56) Xu, C.; Stiubianu, G. T.; Gorodetsky, A. A. Adaptive Infrared-Reflecting Systems Inspired by Cephalopods. *Science* **2018**, *359* (6383), 1495–1500. https://doi.org/10.1126/science.aar5191.
(57) Song, J.; Lu, L.; Li, B.; Zhang, B.; Hu, R.; Zhou, X.; Cheng, Q. Thermal Routing via Near-Field Radiative Heat Transfer. *International Journal of Heat and Mass Transfer* **2020**, *150*, 119346.

(58) Xuan, Y. An Overview of Micro/Nanoscaled Thermal Radiation and Its Applications. *Photonics and Nanostructures - Fundamentals and Applications* **2014**, *12* (2), 93–113. https://doi.org/10.1016/j.photonics.2014.02.003.
(59) Goetzler, W.; Guernsey, M.; Young, J.; Fujrman, J.; Abdelaziz, A. *The Future of Air Conditioning for Buildings*; Navigant Consulting, Burlington, MA (United States), 2016. https://www.osti.gov/biblio/1420235 (accessed 2024-01-22).
(60) Li, Z.; Chen, W. Progress in Dynamic Emissivity Regulation: Control Methods, Material Systems, and Applications. *Mater. Chem. Front.* **2021**, *5* (17), 6315–6332. https://doi.org/10.1039/D1QM00624J.
(61) Zhao, H.; Sun, Q.; Zhou, J.; Deng, X.; Cui, J. Switchable Cavitation in Silicone Coatings for Energy-Saving Cooling and Heating. *Advanced Materials* **2020**, *32* (29), 2000870. https://doi.org/10.1002/adma.202000870.
(62) Mandal, J.; Du, S.; Dontigny, M.; Zaghib, K.; Yu, N.; Yang, Y. Li4Ti5O12: A Visible-to-Infrared Broadband Electrochromic Material for Optical and Thermal Management. *Advanced Functional Materials* **2018**, *28* (36), 1802180. https://doi.org/10.1002/adfm.201802180.
(63) Zhang, X. A.; Yu, S.; Xu, B.; Li, M.; Peng, Z.; Wang, Y.; Deng, S.; Wu, X.; Wu, Z.; Ouyang, M.; Wang, Y. Dynamic Gating of Infrared Radiation in a Textile. *Science* **2019**, *363* (6427), 619–623. https://doi.org/10.1126/science.aau1217.
(64) Lu, L.; Wu, Z.; Ji, C.; Song, M.; Feng, H.; Ma, X.; Jiang, Y. Effect of Fe Doping on Thermochromic Properties of VO2 Films. *J Mater Sci: Mater Electron* **2018**, *29* (7), 5501–5508. https://doi.org/10.1007/s10854-018-8518-1.
(65) Athanasopoulos, N.; Siakavellas, N. J. Programmable Thermal Emissivity Structures Based on Bioinspired Self-Shape Materials. *Sci Rep* **2015**, *5* (1), 17682. https://doi.org/10.1038/srep17682.
(66) Paik, T.; Hong, S.-H.; Gaulding, E. A.; Caglayan, H.; Gordon, T. R.; Engheta, N.; Kagan, C. R.; Murray, C. B. Solution-Processed Phase-Change VO_2 Metamaterials from Colloidal Vanadium Oxide (VO_x) Nanocrystals. *ACS Nano* **2014**, *8* (1), 797–806. https://doi.org/10.1021/nn4054446.
(67) Ohm, C.; Brehmer, M.; Zentel, R. Liquid Crystalline Elastomers as Actuators and Sensors. *Advanced Materials* **2010**, *22* (31), 3366–3387. https://doi.org/10.1002/adma.200904059.
(68) Wang, Y.; He, Q.; Wang, Z.; Zhang, S.; Li, C.; Wang, Z.; Park, Y.-L.; Cai, S. Liquid Crystal Elastomer Based Dexterous Artificial Motor Unit. *Advanced Materials* **2023**, *35* (17), 2211283. https://doi.org/10.1002/adma.202211283.
(69) Berszakiewicz, A.; Kasperczyk, J.; Sieroń, A.; Krasiński, Z.; Cholewka, A.; Stanek, A. The Effect of Compression Therapy on Quality of Life in Patients with Chronic Venous Disease: A Comparative 6-Month Study. *pdia* **2021**, *38* (3), 389–395. https://doi.org/10.5114/ada.2020.92277.
(70) Zarchi, K.; Jemec, G. B. E. Delivery of Compression Therapy for Venous Leg Ulcers. *JAMA Dermatol* **2014**, *150* (7), 730. https://doi.org/10.1001/jamadermatol.2013.7962.
(71) Todd, M. Compression Bandaging: Types and Skills Used in Practical Application. *Br J Nurs* **2011**, *20* (11), 681–687. https://doi.org/10.12968/bjon.2011.20.11.681.
(72) Webb, E.; Neeman, T.; Bowden, F. J.; Gaida, J.; Mumford, V.; Bissett, B. Compression Therapy to Prevent Recurrent Cellulitis of the Leg. *N Engl J Med* **2020**, *383* (7), 630–639. https://doi.org/10.1056/NEJMoa1917197.

(73) Keller, A.; Müller, M. L.; Calow, T.; Kern, I. K.; Schumann, H. Bandage Pressure Measurement and Training: Simple Interventions to Improve Efficacy in Compression Bandaging. *International Wound Journal* **2009**, *6* (5), 324–330. https://doi.org/10.1111/j.1742-481X.2009.00621.x.
(74) Mosti, G.; Cavezzi, A.; Partsch, H.; Urso, S.; Campana, F. Adjustable Velcro® Compression Devices Are More Effective than Inelastic Bandages in Reducing Venous Edema in the Initial Treatment Phase: A Randomized Controlled Trial. *European Journal of Vascular and Endovascular Surgery* **2015**, *50* (3), 368–374. https://doi.org/10.1016/j.ejvs.2015.05.014.
(75) Mosti, G.; Picerni, P.; Partsch, H. Compression Stockings with Moderate Pressure Are Able to Reduce Chronic Leg Oedema. *Phlebology* **2012**, *27* (6), 289–296. https://doi.org/10.1258/phleb.2011.011038.
(76) Kumar, B.; Das, A.; Alagirusamy, R. Study on Interface Pressure Generated by a Bandage Using *in Vitro* Pressure Measurement System. *Journal of the Textile Institute* **2013**, *104* (12), 1374–1383. https://doi.org/10.1080/00405000.2013.807020.
(77) Feldman, J. L.; Stout, N. L.; Wanchai, A.; Stewart, B. R.; Cormier, J. N.; Armer, J. M. Intermittent Pneumatic Compression Therapy: A Systematic Review. *Lymphology* **2012**, *45* (1), 13–25.
(78) Morris, R. J.; Woodcock, J. P. Intermittent Pneumatic Compression or Graduated Compression Stockings for Deep Vein Thrombosis Prophylaxis?: A Systematic Review of Direct Clinical Comparisons. *Annals of Surgery* **2010**, *251* (3), 393–396. https://doi.org/10.1097/SLA.0b013e3181b5d61c.
(79) Hakala, T.; Puolakka, A.; Nousiainen, P.; Vuorela, T.; Vanhala, J. Application of Air Bladders for Medical Compression Hosieries. *Textile Research Journal* **2018**, *88* (19), 2169–2181. https://doi.org/10.1177/0040517517716907.
(80) Rahimi, M.; Blaber, A. P.; Menon, C. Motorized Adaptive Compression System for Enhancing Venous Return: A Feasibility Study on Healthy Individuals. *Medical Engineering & Physics* **2017**, *50*, 65–74. https://doi.org/10.1016/j.medengphy.2017.10.005.
(81) Yang, S. T.; Ryu, J. W.; Park, S.-H.; Lee, Y. B.; Koo, S. H.; Park, Y.-L.; Lee, G. An Active Compression Sleeve with Variable Pressure Levels Using a Wire-Fabric Mechanism and a Soft Sensor. *Smart Mater. Struct.* **2019**, *28* (11), 114002. https://doi.org/10.1088/1361-665X/ab3f56.
(82) Pourazadi, S.; Ahmadi, S.; Menon, C. Towards the Development of Active Compression Bandages Using Dielectric Elastomer Actuators. *Smart Mater. Struct.* **2014**, *23* (6), 065007. https://doi.org/10.1088/0964-1726/23/6/065007.
(83) Ross, L. T. Intelligent Compression Wrap. US11154453B2, October 26, 2021. https://patents.google.com/patent/US11154453B2/en (accessed 2024-04-29).
(84) Kumar, B.; Hu, J.; Pan, N. Smart Medical Stocking Using Memory Polymer for Chronic Venous Disorders. *Biomaterials* **2016**, *75*, 174–181. https://doi.org/10.1016/j.biomaterials.2015.10.032.
(85) Ahmad, M.; Luo, J.; Miraftab, M. Feasibility Study of Polyurethane Shape-Memory Polymer Actuators for Pressure Bandage Application. *Science and Technology of Advanced Materials* **2012**, *13* (1), 015006. https://doi.org/10.1088/1468-6996/13/1/015006.
(86) Kumar, B.; Hu, J.; Pan, N.; Narayana, H. A Smart Orthopedic Compression Device Based on a Polymeric Stress Memory Actuator. *Materials & Design* **2016**, *97*, 222–229. https://doi.org/10.1016/j.matdes.2016.02.092.

(87) Narayana, H.; Hu, J.; Kumar, B.; Shang, S.; Han, J.; Liu, P.; Lin, T.; Ji, F.; Zhu, Y. Stress-Memory Polymeric Filaments for Advanced Compression Therapy. *J. Mater. Chem. B* **2017**, *5* (10), 1905–1916. https://doi.org/10.1039/C6TB03354G.
(88) Narayana, H.; Hu, J.; Kumar, B.; Shang, S.; Ying, M.; Young, R. J. Designing of Advanced Smart Medical Stocking Using Stress-Memory Polymeric Filaments for Pressure Control and Massaging. *Materials Science and Engineering: C* **2018**, *91*, 263–273. https://doi.org/10.1016/j.msec.2018.05.026.
(89) Alavi, A.; Sibbald, R. G.; Phillips, T. J.; Miller, O. F.; Margolis, D. J.; Marston, W.; Woo, K.; Romanelli, M.; Kirsner, R. S. What's New: Management of Venous Leg Ulcers. *Journal of the American Academy of Dermatology* **2016**, *74* (4), 643–664. https://doi.org/10.1016/j.jaad.2015.03.059.
(90) Jovanović, T.; Penava, Ž.; Vrljičak, Z. Impact of the Elastane Percentage on the Elastic Properties of Knitted Fabrics under Cyclic Loading. *Materials* **2022**, *15* (19), 6512. https://doi.org/10.3390/ma15196512.
(91) Murphree, R. W. Impairments in Skin Integrity. *Nursing Clinics of North America* **2017**, *52* (3), 405–417. https://doi.org/10.1016/j.cnur.2017.04.008.
(92) *Nutrition and Functional Foods for Healthy Aging*; Watson, R. R., Ed.; Academic Press: London San Diego Cambridge Oxford, 2017.
(93) Berliner, E.; Ozbilgin, B.; Zarin, D. A. A Systematic Review of Pneumatic Compression for Treatment of Chronic Venous Insufficiency and Venous Ulcers. *Journal of Vascular Surgery* **2003**, *37* (3), 539–544. https://doi.org/10.1067/mva.2003.103.
(94) Wienert, V.; Sick, H.; zur Mühlen, J. [Local thermal stress tolerance of human skin]. *Anasth Intensivther Notfallmed* **1983**, *18* (2), 88–90.
(95) Coelho Rezende, G.; O'Flynn, B.; O'Mahony, C. Smart Compression Therapy Devices for Treatment of Venous Leg Ulcers: A Review. *Adv Healthcare Materials* **2022**, *11* (17), 2200710. https://doi.org/10.1002/adhm.202200710.

Chapter 2 Magnetic vitrimer-based soft robotics

2.1 Introduction

Shape-morphing materials that can alter their configurations under various external stimuli, such as temperature, light, pH, humidity, electrical and magnetic fields, have been explored for diverse applications such as actuators, wearable devices, soft robotics and flexible electronics[1]. In this context, various stimuli-responsive materials have been developed, including liquid crystal elastomers[2], stimuli-responsive hydrogels[3] and shape memory polymers[4]. In particular, magnetically responsive soft materials composed of magnetic particles and polymer matrix have shown many unique and desirable features including fast response[5], reversible actuation[6], self-healing[7] and facile controllability[8], which has great potential in various applications with minimally invasive interactions[9,10].

Commonly adopted actuation mechanisms of magnetically responsive soft composite materials rely on the magnetic gradient-induced external force and magnetic field-induced torque exerting on the materials[11]. When the magnetic particles are embedded into a matrix, an external magnetic field can be used to remotely and rapidly actuate the soft composite. Recent studies have demonstrated several creative applications utilizing these composites. For example, a magnetically actuated soft continuum robot has been controlled to actively navigate and steer in confined environments[8]. Hu et al.[6] developed a small-scale magneto-elastic soft robot with silicone elastomer matrix (Ecoflex 00-10) embedded with hard magnetic neodymium-iron-boron (NdFeB) microparticles, which exhibited enhanced mobility and multimodal locomotion with controlled external magnetic field and carefully designed magnetic domain in the composite. Moreover, Kim et al.[5] fabricated magnetic responsive elastomers through the 3D printing

technique, enabling fast transformations between complex 3D shapes by programming ferromagnetic domains. For the examples above, elastic actuation of the polymer matrix is employed, where the material returns to its original configuration upon the removal of the magnetic field.

Limited actuation modes and deformability of elastomer-based soft actuators can be improved by substituting the elastomer matrix with viscous fluid. Viscous fluid greatly enhances the deformability of the soft actuators. Recent studies have reported the use of fluid-based magnetic responsive actuators such as ferrofluid[12] and magnetic slime[13] to build non-invasive and reconfigurable miniature robots, which show nearly infinite deformability[14]. Thanks to the flowability of the viscous fluid, these soft actuators are capable of passing through confined spaces that are much smaller than their sizes without any damage. Moreover, fluid-based magnetic robots can generate drastic shape changes under magnetic control, enabling novel functionalities including object manipulation and transportation[15–19]. For instance, Fan et al.[16] have developed collective magnetically actuated ferrofluid with multiple deformation modes such as splitting and forming various liquid-robot aggregates, which can be utilized for navigation in multi-terrain surfaces and confined spaces. Researchers have also investigated a single ferrofluid droplet controlled by spatiotemporally changing the external magnetic field to deliver and manipulate delicate objects[20]. However, magnetically actuated tiny droplets often experience additional resistance from their surface tension. One recent work[13] has proposed magnetic slime as a magnetic actuated soft robot with great adaptability and deformability compared with conventional magnetic droplet robots, being able to work across multiple interfaces and underwater. However, those soft actuators usually do not show reversible and elastic responses, which are often needed for many tasks such as cyclic gripping and releasing

items, reversible expansion/collapsing and impulsive motion based on the spring-latch mechanism.

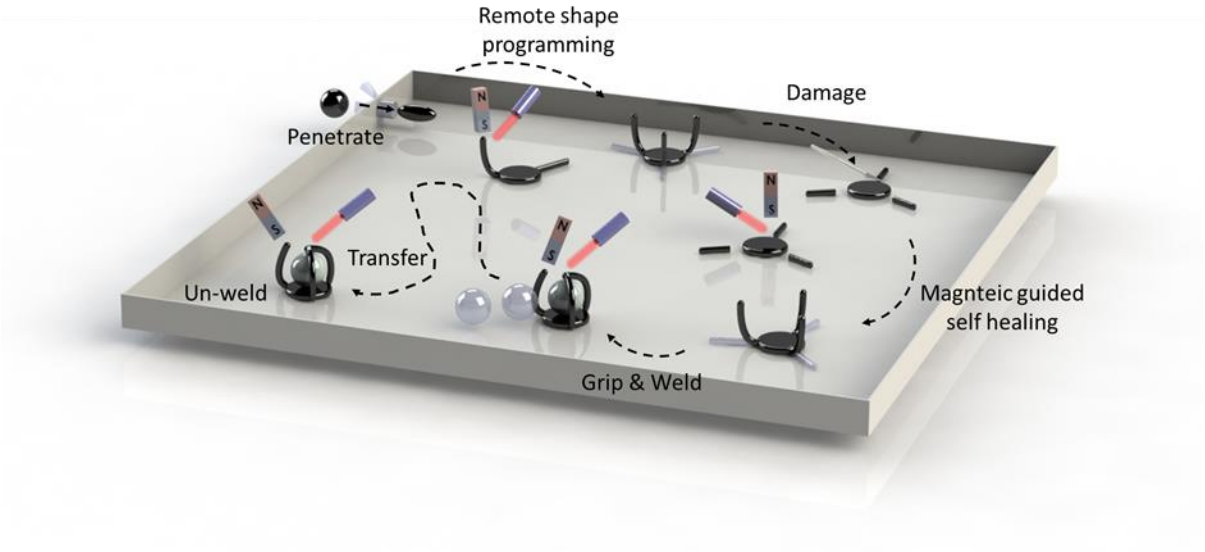

Figure 2.1 A magnetic vitrimer-based soft robot can squeeze itself to pass through an extremely confined space, reshape, self-heal, grip, transport and release an object.

The elastomer-based and fluid-based magnetic soft actuators both have been studied extensively, but each type has certain limitations: the actuation strain of an elastomer-based magnetic actuator is typically small, while the actuation of most fluid-based magnetic actuators is irreversible. To combine the characteristics of both elastomer-based actuators and fluid-based actuators, researchers have employed the polymer matrix with dynamic covalent bonds, which can rearrange their network under certain stimuli such as heat and ultraviolet (UV) irradiation[9,21,22]. Kuang et al.[23] have recently developed polymers with dynamic covalent bonds embedded with hard-magnetic particles for modular assembling and reconfigurable architectures with reprogrammable actuation modes. However, versatile and drastic permanent shape morphing has yet been demonstrated.

In this work, we have developed a magnetically responsive soft composite with a polymer matrix containing disulfide bonds embedded with magnetic particles. The exchange reaction of disulfide bonds occurs under heat or infrared (IR) irradiation. Consequently, disulfide bonds dynamically rearrange and the mobility of the polymer chains significantly increase[24,25]. The deformation mechanism of the magnetic vitrimer (MV) lies in its temperature-sensitive rheological behavior, which allows reversible actuation at room temperature and also drastic shape change with mild temperature increase. Besides, we used a laser to remotely control the local temperature field of the MV to enable local and more precise shape morphing. Furthermore, unlike most self-healing materials that need to be manually brought together[7] and subjected to mechanical pressure[25] during the healing process, a broken MV can self-heal without being touched under the guidance of an external magnetic field. As shown in **Figure 1**, we demonstrated an MV-based soft robot that can: 1) pass through a gap that is smaller than its original size, 2) dramatically transform its shape to a soft robotic gripper, 3) contactless self-heal from permanent damage, 4) catch and secure a fast-moving object, 5) transport and release the object.

2.2 Results and discussion

2.2.1 Fabrication and characterization of the magnetic vitrimer

The schematics of the material preparation are shown in **Figure 2.2A and 2.2B**: we prepared the MV using epoxy monomers (EPS25, epoxy equivalent = 462 $g \cdot equiv^{-1}$) with stoichiometric mixtures of two sulfhydryls: 2,2′ - (ethylenedioxy)diethanethiol (EDDET) and

pentaerythritol tetrakis (3-mercaptopropionate) (PETMP). The polymer network is formed through a thiol-epoxy reaction, where the EDDET with two thiol groups forms the polymer chains together with EPS25 and the PETMP with four thiol groups crosslinks the polymer chains into a network. We chose (dimethylamino)pyridine (DMAP) as the catalyst. In addition, we tuned molar ratio (γ) of thiol groups from EDDET and PETMP to tailor the crosslinking density of the MV and thus its thermomechanical properties, while maintaining the thiol group concentration the same. As shown in **Figure 2.2C**, as the temperature rises, the disulfide bonds can readily be cleaved and re-formed from a reduction reaction and an oxidation reaction, respectively[24,26], endowing the fluid-like behavior to the vitrimer.

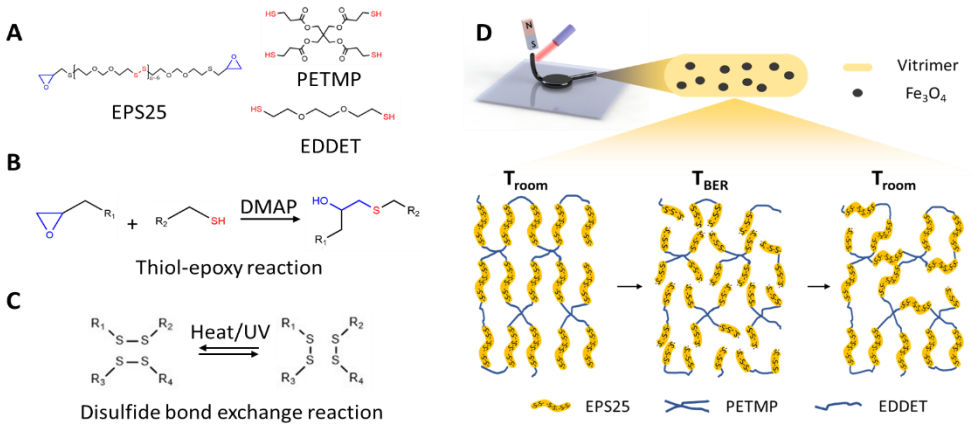

Figure 2.2 Preparation and molecular structure of the magnetic vitrimer used in the current study.
(A) Molecular structure of the monomer EPS25, crosslinker PETMP and chain extender EDDET. (B) Crosslinking mechanism of thiol-epoxy reaction with DMAP (4-Dimethylaaminopyridine) as the catalyst. (C) Mechanism of disulfide bond exchange reaction. (D) Reconfiguration mechanism of magnetic vitrimer.

To prepare a magnetically responsive vitrimer, we embedded magnetic microparticles (Fe_3O_4) into the polymer matrix, where the schematic of the MV and its reconfiguration mechanism is illustrated in **Figure 2.2D**. The monomers consist of abundant disulfide bonds and the bond exchange reaction (BER) becomes more active at an elevated temperature (T_{BER}),

leading to increased flowability of the composite. As a result, a magnetic gradient can induce dramatic and irreversible shape changes of magnetic vitrimer in a controlled manner. When the environmental temperature is dropped to room temperature, the disulfide bond exchange reaction becomes much less active and the MV behaves like a normal elastomer. The temperature-dependent behavior of the MV allows its shape reprogramability and also reversible actuation.

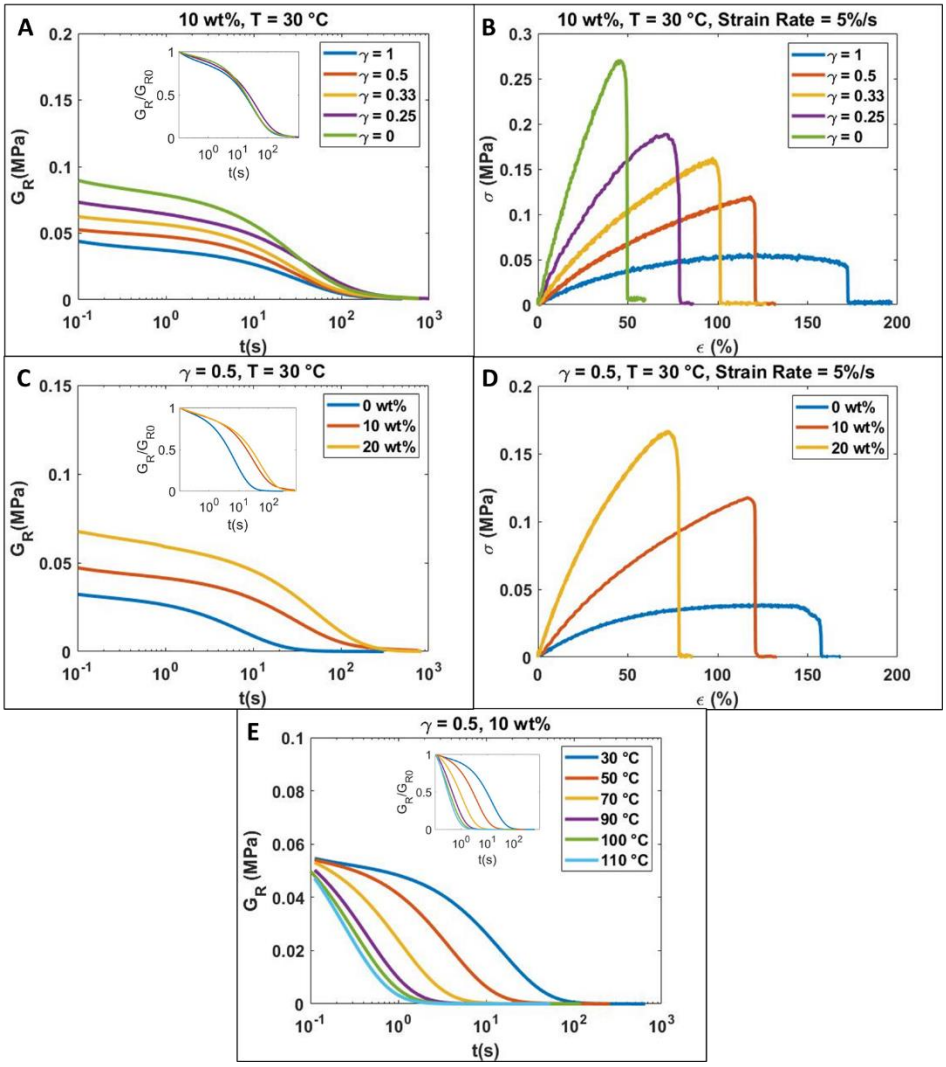

Figure 2.3 Thermomechanical characterizations of the MVs.
(A) Stress relaxation of MVs with different chain extender-crosslinker ratios (γ) at T= 30 °C. The inset shows the normalized experimental results. (B) Uniaxial tensile testing results of MVs with different chain extender-crosslinker ratios (γ) at T= 30 °C. (C) Stress relaxation of MVs with different weight percent of magnetic particles at T= 30 °C and the inset shows the normalized results. (D) Uniaxial tensile testing results of MV with different weight percent of a magnetic particle at T= 30 °C. (E) Stress relaxation of MVs at different temperatures.

To evaluate the potential of using MV for soft robotics, we systematically studied the effects of the two major parameters on the thermomechanical properties of the material: the stoichiometric ratio γ of chain extender to crosslinker and the weight percentage of the magnetic particles in the composite. We varied the γ value from 0 to 1 to investigate the effect of crosslinking density on the properties of MV composite at ambient temperature (30 °C) with a fixed magnetic particle loading (10 wt%). Among all the samples, we fixed the ratio between thiol groups (from EDDET and PETMP) and epoxy groups (from EPS25) to keep the concentration of the dynamic covalent bond as constant. As illustrated in **Figure 2.3A** (G_R in the relaxation shear modulus), the normalized stress relaxation for the samples with different γ values shows similar relaxation times, suggesting that the kinetics of the disulfide bond exchange reaction is not affected by the crosslinking density. However, the magnitude of the relaxation modulus is negatively correlated to γ. The stress vs. strain curves in **Figure 2.3B** show that both the stiffness and strength of the MV increase as the γ value decreases. The γ value is the molar ratio of the thiol group from EDDET and PETMP, where PETMP has four thiol groups and forms a crosslinking junction. Therefore, the material modulus and strength increase by increasing the crosslinking density.

In addition to the γ value, the magnetic particle loading also affects the mechanical behavior of MV. In **Figure 2.3C and 2.3D**, as the loading of magnetic particles increases from 0 wt% to 20 wt% for a given γ value (0.5), the relaxation time of the material increases by one order of magnitude and the material strength doubles. Both the mechanical property and magnetic response of the MV vary with the concentration of magnetic particles. Although higher

magnetic particle concentration can enhance magnetic response, introducing too many magnetic particles to the vitrimer matrix can affect the viscoelastic properties of MV. **Figure 2.4** shows that the viscosity of MV increases with increasing the concentration of magnetic particles. Therefore, at ambient temperature, higher magnetic particle loading increases the stiffness of the MV, requiring a larger force to actuate the body, which limits the magnetic actuation capabilities of the material. Moreover, at high temperatures, the viscosity will also increase with higher magnetic particle loading, which limits the flowability of the MV.

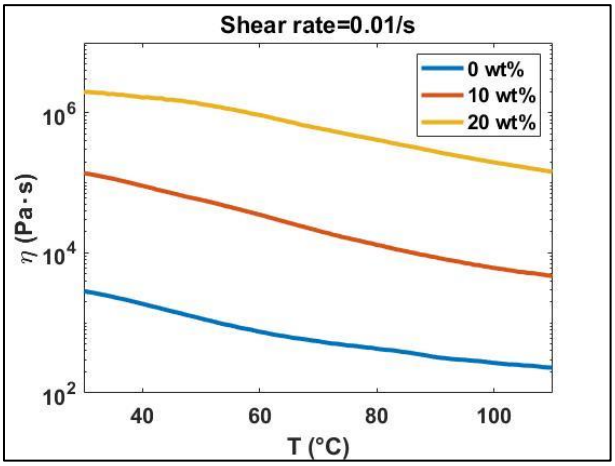

Figure 2.4 Viscosity (η) of MV with different magnetic particle loading as a function of temperature (T).

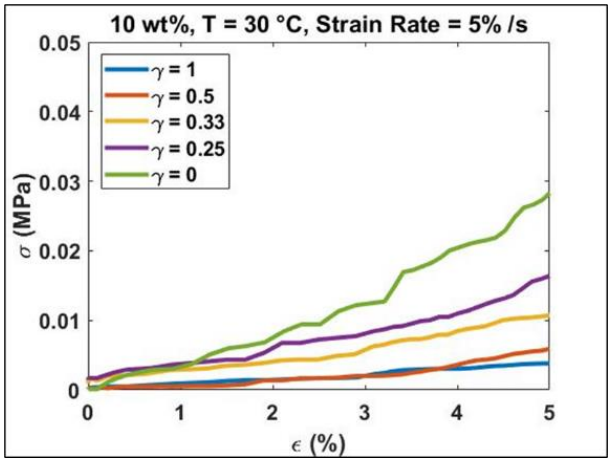

Figure 2.5 Zoom-in of Figure 2.3B, from which we calculated the secant modulus at 5% strain.

In the context of soft robotic grippers, their primary functionality is the ability to grasp or catch an object and hold against the external disturbance, and high compliance of the material can reduce control complexity. In most applications, the time scale of grasping or catching an object is typically less than a few seconds[27–29], requiring that the relaxation time of the composite at room temperature is longer than tens of seconds. On the other hand, low viscosity of MV at high temperature is desired during the shape morphing. Therefore, we chose the molar ratio (γ = 0.5) and magnetic particle loading (=10 wt%) to prepare the MV for the rest of this study, with a relaxation time of around 100 seconds and secant modulus of 0.11 MPa at ambient temperature (**Figure 2.5**). As shown in **Figure 2.3E**, using the selected MV, we conducted the stress relaxation tests at different temperatures. The decrease of the relaxation time with increasing temperature is due to the accelerated disulfide bond exchange reaction at higher temperature[30].

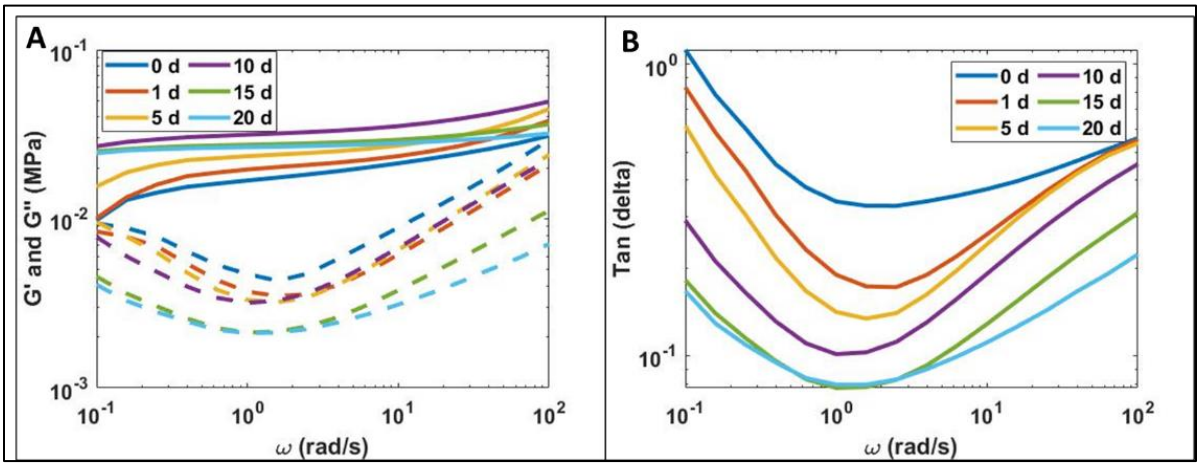

Figure 2.6 Viscoelastic properties of magnetic vitrimer stored for different period of times. A) Storage modulus (G', solid line), loss modulus (G'', dash line) and B) Tan(δ) of vitrimer varied as a function of angular frequency (ω) from 0.1 to 100 rad/s at a strain level of 1%, T = 30°C.

Finally, we have also examined the possible degradation of the property of the MV during its storage. **Figure 2.6** shows that as the stored time increases, the storage modulus (G') increases and tan(δ) decreases. Such property degradation is mainly due to the decrease of the

efficiency of the catalyst (DMAP) over time in the system[31,32]. It is noted that there have been various types of vitrimers, the dynamic bond exchanging reaction of which does not need any catalyst[33]. The properties of those vitrimers are often more stable after a long period of storage.

2.2.2 Demonstration of magnetic vitrimer-based soft robotics

In this study, we demonstrated four distinct working modes of an MV-based soft robot: 1) passing through confined environments, 2) permanent shape morphing with remote control, 3) touchless self-healing and 4) manipulating objects as a soft gripper.

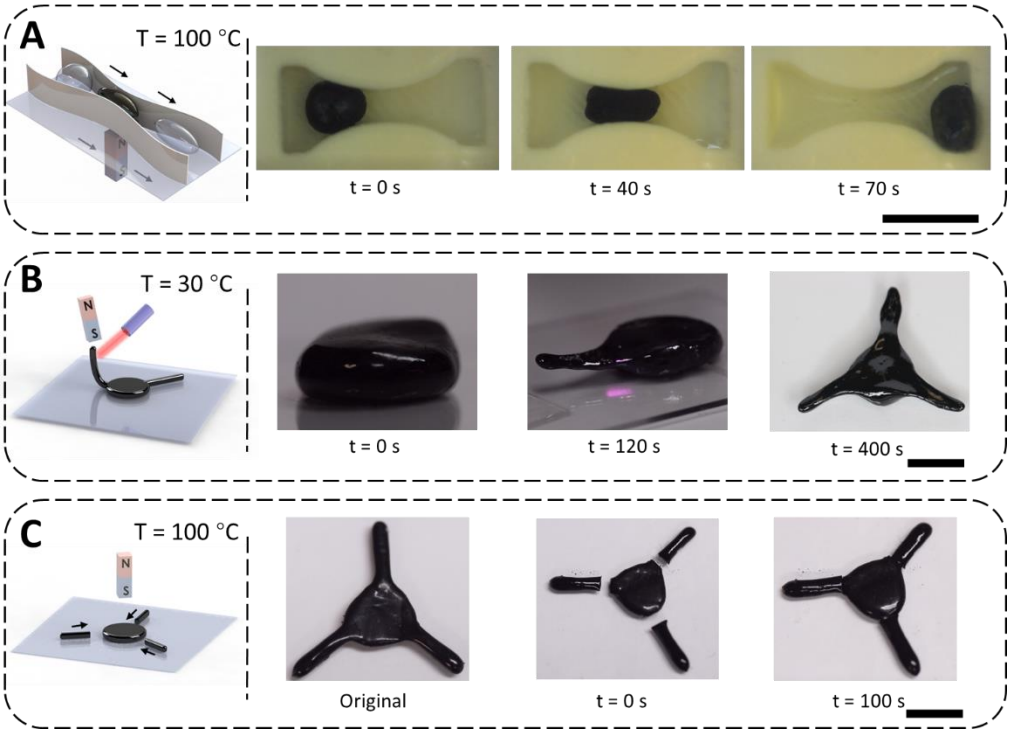

Figure 2.7 Heat enabled flowability, remote shape morphing and self-healing of MV. (A) At an elevated temperature (100 °C), an MV sphere can pass through a narrow opening with an applied magnetic field. Scale bar, 1 cm. (B) An MV disk can transform into a soft gripper by applying local heating with a laser beam and a magnetic field by a permanent magnet. Scale bar, 1 cm. (C) Self-healing capability of the soft gripper after severe damage. Scale bar, 1 cm.

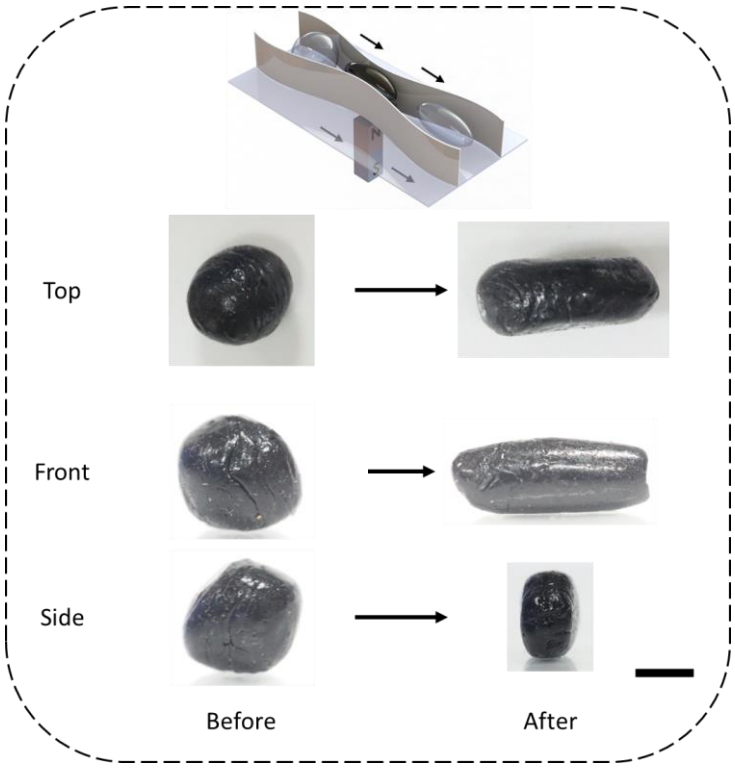

Figure 2.8 Dimensions of a spherical MV before and after passing through a narrow opening. Scale bar, 2 mm.

We first demonstrated the heat-enhanced flowability of the MV as shown in **Figure 2.7A**. A spherical MV was blocked by a narrow opening. The external magnetic field could not drive the MV to move through the opening at the room temperature because of its relatively high stiffness. When we heated the local environment to 100 °C, the disulfide bond exchange reaction became more active, leading to a significant increase of the flowability of the MV. With an applied magnetic field, the magnetic gradient-induced pulling force exerted on the MV drove it to flow through the narrow opening within around 1 min. The dimensions of the MV before and after penetrating through the small opening are shown in **Figure 2.8**.

The magnetic field gradient for actuation was generated by a cubic permanent magnet (25 x 25 x 25 mm, N52 Neodymium Magnet from KJ Magnetics), which has a magnetic field density

of 4000 gauss at the surface, measured by a hand-held gauss meter (TD8620, Tunkia). The MV was able to flow through the opening at a distance around 10 - 20 mm away from the surface of the magnet, where the magnetic field density ranges from 1500 to 500 gauss. After the MV robot completely went through the opening, both the thermal and magnetic fields were removed, and the material regained its elasticity.

We further extended the working mechanism of the MV to broaden its functionality by introducing localized heating, which can enhance the flowability of specific regions in the material. With the application of magnetic gradient, remote control of shape morphing could be realized in a designed fashion. As shown in **Figure 2.7B**, with the assistance of the local thermal field generated by an infrared laser pointer (Sky laser, PL-808-1000B) and the magnetic gradient in-line with the direction of robotic gripper 'arms', the MV could change its configuration from a disk shape to a soft robotic gripper.

We next demonstrated the magnetically guided self-healing of the MV gripper. As shown in **Figure 2.7C**, the three 'arms' of the MV gripper were separated from the 'body' by a sharp blade. To initiate the self-healing process, we placed a permanent magnet on the top of the gripper and heated up the environment to 100 °C for 100 seconds. The magnetic gradient-induced pulling force allowed the broken 'arms' to move toward the main 'body' without direct applied contact. The elevated temperature accelerates the disulfide bond exchange reaction, permitting the self-healing of the MV gripper at the broken regions. Upon the removal of the magnetic and thermal field, the gripper regained its integrity and elasticity.

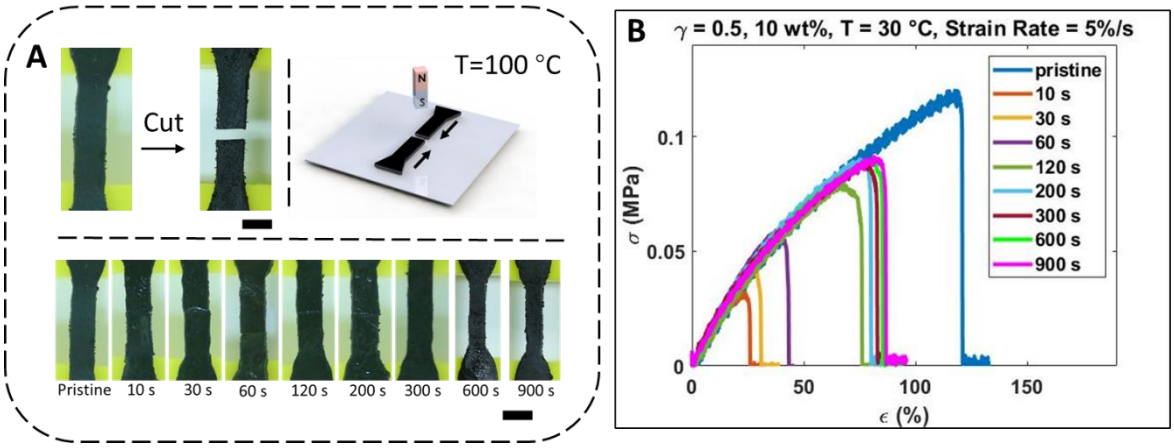

Figure 2.9 Magnetically assisted self-healing of MV.
(A) MV strips were first cut into two parts at 30 °C. Then, assisted by the external magnetic field, the two broken parts were brought into contact and heated up at a temperature of 100 °C to trigger the dynamic bond exchange reaction. Specimens were healed for different period of time. Scale bar, 2 mm. (B) Tensile stress-strain relationship of self-healed MV strips with different healing times.

To further investigate the self-healing efficiency of the MV, we studied the self-healing time of MV by conducting the tensile tests. As illustrated in **Figure 2.9A**, the specimens were cut into two halves at ambient temperature (30 °C) by using a sharp blade. The two segments were then brought into contact with the help of an external magnetic field and put at 100 °C for various period of time. The self-healing times for the MV sample were set to 0, 10, 30, 60, 120, 200, 300, 600 and 900 seconds. We conducted tensile test at 5% s^{-1} strain rate and the results are shown in **Figure 2.9B**. Self-healed MVs exhibited similar strength at 120, 200,300, 600 and 900 seconds at around 0.8 MPa, which was around 80% of the pristine sample. The results also agreed with our previous measurements of the relaxation time, which was around 100 seconds, indicating that the dynamic bonds need around 100 seconds to form between separated pieces.

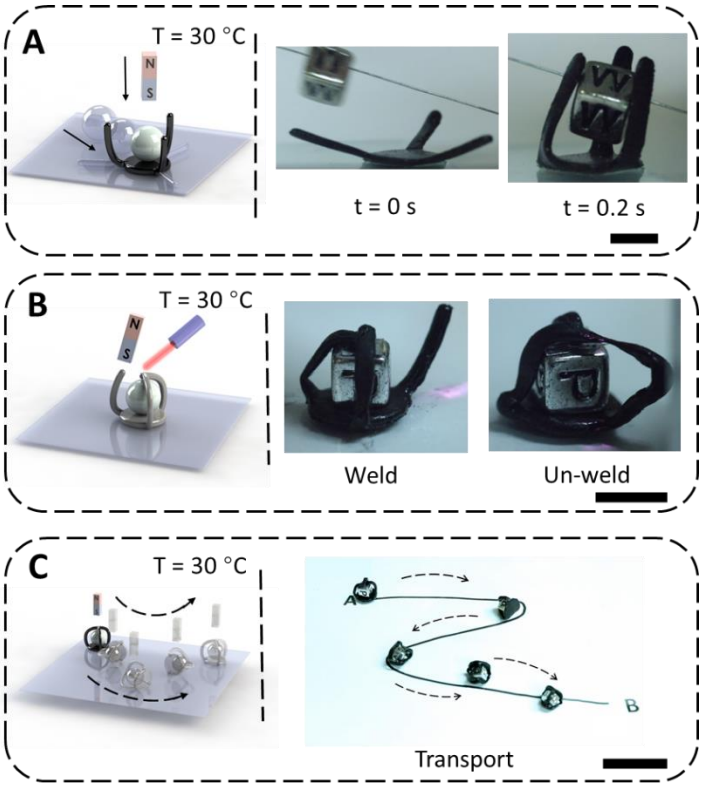

Figure 2.10 MV based soft gripper catches, welds, un-welds and transports an object. (A) The soft robotic gripper can catch a moving object through fast actuation. Scale bar, 1 cm. (B) Welding/un-welding of the gripper to secure/release the object. Scale bar, 1 cm. (C) With an externally applied magnetic field, the soft robotic gripper can carry the object and move along a planned path. Scale bar, 5 cm.

At last, we demonstrated the capability of the soft robotic gripper interacting with a moving object through magnetic control. As shown in **Figure 2.10A,** a magnetic field with a strong gradient exerted a pulling force onto the iron oxide microparticles, which could attract each ‘arm’ align with the magnetic field. On the other hand, the ‘arm’ also tended to align with the magnetic field direction, due to the body-force torque from anisotropic gripper geometry and paramagnetic torque from iron oxide anisotropic distribution. Therefore, the deformation resulted from a balance between the elastic restoring force of the gripper and magnetic force exerted onto the gripper. At the ambient temperature (T=30 °C), fast response of the gripper controlled by a permanent magnet allowed the soft robotic gripper to catch a fast-moving object. The gripper

was also able to release the object on demand. By further harnessing the remote local shape morphing capability of MV, the soft robotic gripper could secure and release the object by 'welding' and 'un-welding' of the 'arms', as shown in **Figure 2.10B**. With careful manipulation of a magnet and a local thermal field, the tip of the 'arms' could be connected or disconnected with an object held inside. In **Figure 2.10C**, the welded soft robotic gripper was able to carry the object and travel along a planned route under the guidance of a magnetic field. Moreover, the soft robotic gripper could protect the object from possible mechanical damage, due to the viscoelastic nature of MV.

2.3 Experimental methods

2.3.1 Magnetic vitrimer preparation

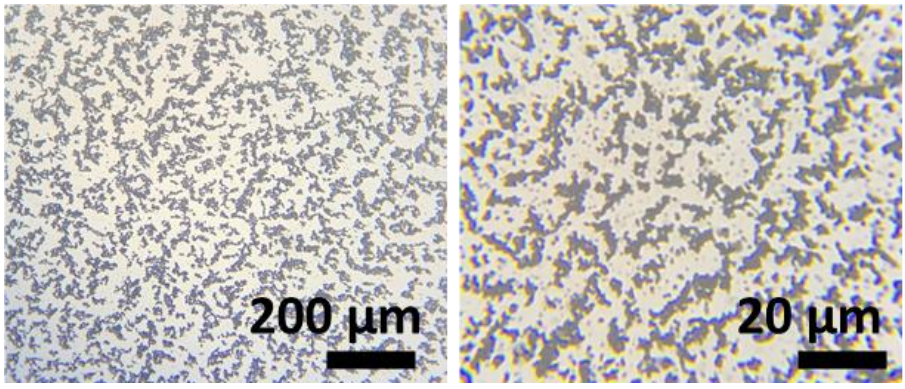

Figure 2.11 Microscopic images of MV mixed 10 wt% iron oxide particles.
The images were taken from OMAX 40X-2000X optical microscope. The images show homogenous distribution of the iron oxide particles within the vitrimer polymer matrix.

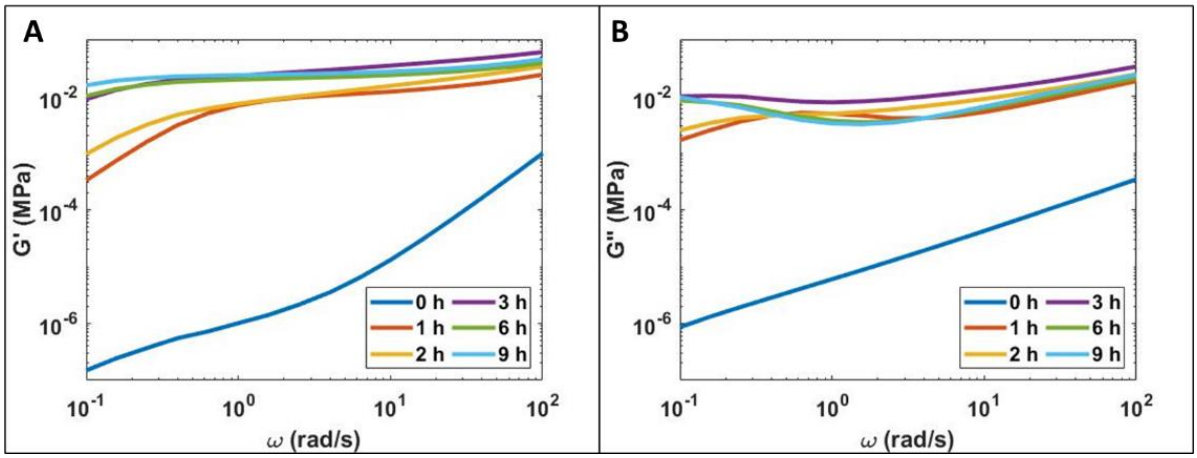

Figure 2.12 Rheological properties of magnetic vitrimer for different period of times of crosslinking.
A) Storage modulus (G') and B) loss modulus (G'') of vitrimer varied as a function of angular frequency (ω) from 0.1 to 100 rad/s at a strain level of 1%, T = 30°C.

MV was prepared by cross-linking epoxy monomer with 2 different sulfhydryls. Briefly, the monomer EPS25 (ThioPlast, epoxy equivalent = 462 g · equiv^{-1}, kindly provided by Norton Functional Chemicals GmbH) and a stoichiometric mixture (γ=0.5) of two crosslinkers: 2,2′-(ethylenedioxy)diethanethiol (EDDET, >95%, Sigma Aldrich) and pentaerythritol tetrakis (3-mercaptopropionate) (PETMP, >95%, Sigma Aldrich) were manually mixed at room temperature. Then, 1 wt% of 4-DMAP (>99.0%, Sigma Aldrich) and 10 wt% of iron oxide microparticles (Fe_3O_4, >98%, d~1μm, Alpha Chemicals) were manually added and mixed into the composition to obtain a homogeneous blend, which was confirmed by the optical microscopic images in **Figure 2.11**. Finally, the mixture was poured into a glass petri dish and cured under 60 °C for 3 hours. As shown in **Figure 2.12**, the storage modulus (G') and loss modulus (G'') of MV change little after 3 hours of curing, indicating the MV is fully cured. To obtain MV sheet with desired thickness for characterization purpose, the samples and a spacer were hot-pressed by a heat press machine (Carver, Wabash) under 100 °C for 2 minutes between

parchment paper. All samples were cooled to room temperature and stored at 30 °C for 24 hours before characterization.

2.3.2 Characterization

The uniaxial test was performed on a dynamic mechanical analysis equipment RSA-G2 (TA instruments, New Castle) using dog bone samples (effective dimension: 2 × 20 × 0.8 mm). The strain rate was 5% s^{-1}. For each sample, three specimens were tested and the average results were reported. The stress relaxation test was conducted on a rheometer DHR3 (TA instruments, New Castle) using disc samples (diameter: 20 mm, thickness: 0.8 mm). The samples were equilibrated at specified temperature for 5 minutes, and then a constant shear strain of 30% (0.015 rad) was applied to monitor the evolution of stress as a function of time. The homogeneous thermal field was created within an in-house built heating chamber including 4 polyimide heating pads (5 V, 1 W, 30 × 40 mm) with a uniform thermal field up to 130 °C. The local thermal field was generated by an infra-red laser pointer PL-808-2000 (Sky Laser, 2 W). The videos and pictures were captured using a digital camera (Cannon EOS 80D).

2.4 Conclusion

In this article, we have designed and fabricated magnetic vitrimer based soft robots. The exchange reaction activity of the dynamic bonds within the MV increases at an elevated temperature, allowing the MV soft robot to have dramatic and irreversible shape change with applied magnetic field. Such dramatic shape change enables the MV based soft robot to pass through a significantly confined space. With the laser-induced local heating and external

magnetic field, the MV-based soft robot can also change its shape with control. Moreover, the combination of embedded magnetic particles and exchange reaction of the dynamic bond in the MV makes it self-healable without requiring any direct touch. At room temperature, MV behaves like a regular elastomer, and the MV based soft robotic gripper can achieve fast catching, releasing and locomotion.

2.5 Reference

(1) Wang, L.; Iida, F. Deformation in Soft-Matter Robotics: A Categorization and Quantitative Characterization. *IEEE Robot. Automat. Mag.* **2015**, *22* (3), 125–139. https://doi.org/10.1109/MRA.2015.2448277.

(2) Laschi, C.; Mazzolai, B.; Cianchetti, M. Soft Robotics: Technologies and Systems Pushing the Boundaries of Robot Abilities. *Sci. Robot.* **2016**, *1* (1), eaah3690. https://doi.org/10.1126/scirobotics.aah3690.

(3) Hao, Y.; Zhang, S.; Fang, B.; Sun, F.; Liu, H.; Li, H. A Review of Smart Materials for the Boost of Soft Actuators, Soft Sensors, and Robotics Applications. *Chin. J. Mech. Eng.* **2022**, *35* (1), 37. https://doi.org/10.1186/s10033-022-00707-2.

(4) Chen, Z.-J.; Gao, F.; Pan, Y. Novel Door-Opening Method for Six-Legged Robots Based on Only Force Sensing. *Chin. J. Mech. Eng.* **2017**, *30* (5), 1227–1238. https://doi.org/10.1007/s10033-017-0172-7.

(5) Carpentier, J.; Mansard, N. Multicontact Locomotion of Legged Robots. *IEEE Trans. Robot.* **2018**, *34* (6), 1441–1460. https://doi.org/10.1109/TRO.2018.2862902.

(6) Shian, S.; Bertoldi, K.; Clarke, D. R. Dielectric Elastomer Based "Grippers" for Soft Robotics. *Advanced Materials* **2015**, *27* (43), 6814–6819. https://doi.org/10.1002/adma.201503078.

(7) Mazzolai, B.; Margheri, L.; Cianchetti, M.; Dario, P.; Laschi, C. Soft-Robotic Arm Inspired by the Octopus: II. From Artificial Requirements to Innovative Technological Solutions. *Bioinspir. Biomim.* **2012**, *7* (2), 025005. https://doi.org/10.1088/1748-3182/7/2/025005.

(8) Shen, Q.; Wang, T.; Liang, J.; Wen, L. Hydrodynamic Performance of a Biomimetic Robotic Swimmer Actuated by Ionic Polymer–Metal Composite. *Smart Mater. Struct.* **2013**, *22* (7), 075035. https://doi.org/10.1088/0964-1726/22/7/075035.

(9) Keplinger, C.; Sun, J.-Y.; Foo, C. C.; Rothemund, P.; Whitesides, G. M.; Suo, Z. Stretchable, Transparent, Ionic Conductors. *Science* **2013**, *341* (6149), 984–987. https://doi.org/10.1126/science.1240228.

(10) Lee, E.; Kim, D.; Kim, H.; Yoon, J. Photothermally Driven Fast Responding Photo-Actuators Fabricated with Comb-Type Hydrogels and Magnetite Nanoparticles. *Sci Rep* **2015**, *5* (1), 15124. https://doi.org/10.1038/srep15124.

(11) Bassik, N.; Abebe, B. T.; Laflin, K. E.; Gracias, D. H. Photolithographically Patterned Smart Hydrogel Based Bilayer Actuators. *Polymer* **2010**, *51* (26), 6093–6098. https://doi.org/10.1016/j.polymer.2010.10.035.
(12) Shin, B.; Ha, J.; Lee, M.; Park, K.; Park, G. H.; Choi, T. H.; Cho, K.-J.; Kim, H.-Y. Hygrobot: A Self-Locomotive Ratcheted Actuator Powered by Environmental Humidity. *Sci. Robot.* **2018**, *3* (14), eaar2629. https://doi.org/10.1126/scirobotics.aar2629.
(13) Poojary, U. R.; Gangadharan, K. V. Material Modeling of Frequency, Magnetic Field and Strain Dependent Response of Magnetorheological Elastomer. *J Mater Sci* **2021**, *56* (28), 15752–15766. https://doi.org/10.1007/s10853-021-06307-0.
(14) Dong, G.; He, Q.; Cai, S. Magnetic Vitrimer-Based Soft Robotics. *Soft Matter* **2022**, *18* (39), 7604–7611. https://doi.org/10.1039/D2SM00893A.
(15) De Gennes, P.; Hébert, M.; Kant, R. Artificial Muscles Based on Nematic Gels. *Macromolecular Symposia* **1997**, *113* (1), 39–49. https://doi.org/10.1002/masy.19971130107.
(16) Brazel, C. S. Magnetothermally-Responsive Nanomaterials: Combining Magnetic Nanostructures and Thermally-Sensitive Polymers for Triggered Drug Release. *Pharm Res* **2009**, *26* (3), 644–656. https://doi.org/10.1007/s11095-008-9773-2.
(17) Thévenot, J.; Oliveira, H.; Sandre, O.; Lecommandoux, S. Magnetic Responsive Polymer Composite Materials. *Chem. Soc. Rev.* **2013**, *42* (17), 7099. https://doi.org/10.1039/c3cs60058k.
(18) Kuang, X.; Wu, S.; Ze, Q.; Yue, L.; Jin, Y.; Montgomery, S. M.; Yang, F.; Qi, H. J.; Zhao, R. Magnetic Dynamic Polymers for Modular Assembling and Reconfigurable Morphing Architectures. *Advanced Materials* **2021**, *33* (30), 2102113. https://doi.org/10.1002/adma.202102113.
(19) Kim, Y.; Yuk, H.; Zhao, R.; Chester, S. A.; Zhao, X. Printing Ferromagnetic Domains for Untethered Fast-Transforming Soft Materials. *Nature* **2018**, *558* (7709), 274–279. https://doi.org/10.1038/s41586-018-0185-0.
(20) Cheng, Y.; Chan, K. H.; Wang, X.-Q.; Ding, T.; Li, T.; Zhang, C.; Lu, W.; Zhou, Y.; Ho, G. W. A Fast Autonomous Healing Magnetic Elastomer for Instantly Recoverable, Modularly Programmable, and Thermorecyclable Soft Robots. *Advanced Functional Materials* **2021**, *31* (32), 2101825. https://doi.org/10.1002/adfm.202101825.
(21) Matxain, J. M.; Asua, J. M.; Ruipérez, F. Design of New Disulfide-Based Organic Compounds for the Improvement of Self-Healing Materials. *Phys. Chem. Chem. Phys.* **2016**, *18* (3), 1758–1770. https://doi.org/10.1039/C5CP06660C.
(22) Maeda, T.; Otsuka, H.; Takahara, A. Dynamic Covalent Polymers: Reorganizable Polymers with Dynamic Covalent Bonds. *Progress in Polymer Science* **2009**, *34* (7), 581–604. https://doi.org/10.1016/j.progpolymsci.2009.03.001.
(23) Ruff, Y.; Lehn, J. Glycodynamers: Dynamic Analogs of Arabinofuranoside Oligosaccharides. *Biopolymers* **2008**, *89* (5), 486–496. https://doi.org/10.1002/bip.20885.
(24) Otsuka, H.; Muta, T.; Sakada, M.; Maeda, T.; Takahara, A. Scrambling Reaction between Polymers Prepared by Step-Growth and Chain-Growth Polymerizations: Macromolecular Cross-Metathesis between 1,4-Polybutadiene and Olefin-Containing Polyester. *Chem. Commun.* **2009**, No. 9, 1073. https://doi.org/10.1039/b818014h.
(25) Guimard, N. K.; Oehlenschlaeger, K. K.; Zhou, J.; Hilf, S.; Schmidt, F. G.; Barner-Kowollik, C. Current Trends in the Field of Self-Healing Materials. *Macro Chemistry & Physics* **2012**, *213* (2), 131–143. https://doi.org/10.1002/macp.201100442.

(26) Bergman, S. D.; Wudl, F. Mendable Polymers. *J. Mater. Chem.* **2008**, *18* (1), 41–62. https://doi.org/10.1039/B713953P.
(27) Cordier, P.; Tournilhac, F.; Soulié-Ziakovic, C.; Leibler, L. Self-Healing and Thermoreversible Rubber from Supramolecular Assembly. *Nature* **2008**, *451* (7181), 977–980. https://doi.org/10.1038/nature06669.
(28) Burattini, S.; Colquhoun, H. M.; Fox, J. D.; Friedmann, D.; Greenland, B. W.; Harris, P. J. F.; Hayes, W.; Mackay, M. E.; Rowan, S. J. A Self-Repairing, Supramolecular Polymer System: Healability as a Consequence of Donor–Acceptor π–π Stacking Interactions. *Chem. Commun.* **2009**, No. 44, 6717. https://doi.org/10.1039/b910648k.
(29) Burnworth, M.; Tang, L.; Kumpfer, J. R.; Duncan, A. J.; Beyer, F. L.; Fiore, G. L.; Rowan, S. J.; Weder, C. Optically Healable Supramolecular Polymers. *Nature* **2011**, *472* (7343), 334–337. https://doi.org/10.1038/nature09963.
(30) Ritz, D.; Beckwith, J. Roles of Thiol-Redox Pathways in Bacteria. *Annu. Rev. Microbiol.* **2001**, *55* (1), 21–48. https://doi.org/10.1146/annurev.micro.55.1.21.
(31) Wedemeyer, W. J.; Welker, E.; Narayan, M.; Scheraga, H. A. Disulfide Bonds and Protein Folding. *Biochemistry* **2000**, *39* (15), 4207–4216. https://doi.org/10.1021/bi992922o.
(32) Spillmann, C. M.; Naciri, J.; Martin, B. D.; Farahat, W.; Herr, H.; Ratna, B. R. Stacking Nematic Elastomers for Artificial Muscle Applications. *Sensors and Actuators A: Physical* **2007**, *133* (2), 500–505. https://doi.org/10.1016/j.sna.2006.04.045.
(33) Zeng, H.; Wani, O. M.; Wasylczyk, P.; Kaczmarek, R.; Priimagi, A. Self-Regulating Iris Based on Light-Actuated Liquid Crystal Elastomer. *Advanced Materials* **2017**, *29* (30), 1701814. https://doi.org/10.1002/adma.201701814.
(34) Rogóż, M.; Zeng, H.; Xuan, C.; Wiersma, D. S.; Wasylczyk, P. Light-Driven Soft Robot Mimics Caterpillar Locomotion in Natural Scale. *Advanced Optical Materials* **2016**, *4* (11), 1689–1694. https://doi.org/10.1002/adom.201600503.
(35) Ahn, C.; Liang, X.; Cai, S. Inhomogeneous Stretch Induced Patterning of Molecular Orientation in Liquid Crystal Elastomers. *Extreme Mechanics Letters* **2015**, *5*, 30–36. https://doi.org/10.1016/j.eml.2015.09.007.
(36) Bisoyi, H. K.; Li, Q. Light-Driven Liquid Crystalline Materials: From Photo-Induced Phase Transitions and Property Modulations to Applications. *Chem. Rev.* **2016**, *116* (24), 15089–15166. https://doi.org/10.1021/acs.chemrev.6b00415.
(37) Boothby, J. M.; Kim, H.; Ware, T. H. Shape Changes in Chemoresponsive Liquid Crystal Elastomers. *Sensors and Actuators B: Chemical* **2017**, *240*, 511–518. https://doi.org/10.1016/j.snb.2016.09.004.
(38) Yakacki, C. M.; Saed, M.; Nair, D. P.; Gong, T.; Reed, S. M.; Bowman, C. N. Tailorable and Programmable Liquid-Crystalline Elastomers Using a Two-Stage Thiol–Acrylate Reaction. *RSC Adv.* **2015**, *5* (25), 18997–19001. https://doi.org/10.1039/C5RA01039J.
(39) Kotikian, A.; Truby, R. L.; Boley, J. W.; White, T. J.; Lewis, J. A. 3D Printing of Liquid Crystal Elastomeric Actuators with Spatially Programed Nematic Order. *Advanced Materials* **2018**, *30* (10), 1706164. https://doi.org/10.1002/adma.201706164.
(40) Wang, Z.; Wang, Z.; Zheng, Y.; He, Q.; Wang, Y.; Cai, S. Three-Dimensional Printing of Functionally Graded Liquid Crystal Elastomer. *Sci. Adv.* **2020**, *6* (39), eabc0034. https://doi.org/10.1126/sciadv.abc0034.
(41) He, Q.; Wang, Z.; Wang, Y.; Song, Z.; Cai, S. Recyclable and Self-Repairable Fluid-Driven Liquid Crystal Elastomer Actuator. *ACS Appl. Mater. Interfaces* **2020**, *12* (31), 35464–35474. https://doi.org/10.1021/acsami.0c10021.

(42) He, Q.; Wang, Z.; Song, Z.; Cai, S. Bioinspired Design of Vascular Artificial Muscle. *Adv Materials Technologies* **2019**, *4* (1), 1800244. https://doi.org/10.1002/admt.201800244.
(43) He, Q.; Wang, Z.; Wang, Y.; Minori, A.; Tolley, M. T.; Cai, S. Electrically Controlled Liquid Crystal Elastomer–Based Soft Tubular Actuator with Multimodal Actuation. *Sci. Adv.* **2019**, *5* (10), eaax5746. https://doi.org/10.1126/sciadv.aax5746.
(44) Wang, C.; Sim, K.; Chen, J.; Kim, H.; Rao, Z.; Li, Y.; Chen, W.; Song, J.; Verduzco, R.; Yu, C. Soft Ultrathin Electronics Innervated Adaptive Fully Soft Robots. *Advanced Materials* **2018**, *30* (13), 1706695. https://doi.org/10.1002/adma.201706695.
(45) Bauman, G. E.; McCracken, J. M.; White, T. J. Actuation of Liquid Crystalline Elastomers at or Below Ambient Temperature. *Angew Chem Int Ed* **2022**, *61* (28), e202202577. https://doi.org/10.1002/anie.202202577.
(46) McCracken, J. M.; Donovan, B. R.; Lynch, K. M.; White, T. J. Molecular Engineering of Mesogenic Constituents Within Liquid Crystalline Elastomers to Sharpen Thermotropic Actuation. *Adv Funct Materials* **2021**, *31* (16), 2100564. https://doi.org/10.1002/adfm.202100564.
(47) Shaha, R. K.; Torbati, A. H.; Frick, C. P. BODY-TEMPERATURE S HAPE-SHIFTING Liquid Crystal Elastomers. *J of Applied Polymer Sci* **2021**, *138* (14), 50136. https://doi.org/10.1002/app.50136.
(48) Sui, C.; Pu, J.; Chen, T.-H.; Liang, J.; Lai, Y.-T.; Rao, Y.; Wu, R.; Han, Y.; Wang, K.; Li, X.; Viswanathan, V.; Hsu, P.-C. Dynamic Electrochromism for All-Season Radiative Thermoregulation. *Nat Sustain* **2023**, *6* (4), 428–437. https://doi.org/10.1038/s41893-022-01023-2.
(49) Tang, K.; Dong, K.; Li, J.; Gordon, M. P.; Reichertz, F. G.; Kim, H.; Rho, Y.; Wang, Q.; Lin, C.-Y.; Grigoropoulos, C. P.; Javey, A.; Urban, J. J.; Yao, J.; Levinson, R.; Wu, J. Temperature-Adaptive Radiative Coating for All-Season Household Thermal Regulation. *Science* **2021**, *374* (6574), 1504–1509. https://doi.org/10.1126/science.abf7136.
(50) *Radiative human body cooling by nanoporous polyethylene textile | Science*. https://www.science.org/doi/10.1126/science.aaf5471 (accessed 2024-02-15).
(51) Wei, H.; Gu, J.; Ren, F.; Zhang, L.; Xu, G.; Wang, B.; Song, S.; Zhao, J.; Dou, S.; Li, Y. Smart Materials for Dynamic Thermal Radiation Regulation. *Small* **2021**, *17* (35), 2100446. https://doi.org/10.1002/smll.202100446.
(52) Ulpiani, G.; Ranzi, G.; Shah, K. W.; Feng, J.; Santamouris, M. On the Energy Modulation of Daytime Radiative Coolers: A Review on Infrared Emissivity Dynamic Switch against Overcooling. *Solar energy* **2020**, *209*, 278–301.
(53) Kats, M. A.; Sharma, D.; Lin, J.; Genevet, P.; Blanchard, R.; Yang, Z.; Qazilbash, M. M.; Basov, D. N.; Ramanathan, S.; Capasso, F. Ultra-Thin Perfect Absorber Employing a Tunable Phase Change Material. *Applied Physics Letters* **2012**, *101* (22), 221101. https://doi.org/10.1063/1.4767646.
(54) Zeng, S.; Shen, K.; Liu, Y.; Chooi, A. P.; Smith, A. T.; Zhai, S.; Chen, Z.; Sun, L. Dynamic Thermal Radiation Modulators via Mechanically Tunable Surface Emissivity. *Materials Today* **2021**, *45*, 44–53. https://doi.org/10.1016/j.mattod.2020.12.001.
(55) Schultz, P. H.; Hermalyn, B.; Colaprete, A.; Ennico, K.; Shirley, M.; Marshall, W. S. The LCROSS Cratering Experiment. *Science* **2010**, *330* (6003), 468–472. https://doi.org/10.1126/science.1187454.

(56) Xu, C.; Stiubianu, G. T.; Gorodetsky, A. A. Adaptive Infrared-Reflecting Systems Inspired by Cephalopods. *Science* **2018**, *359* (6383), 1495–1500. https://doi.org/10.1126/science.aar5191.
(57) Song, J.; Lu, L.; Li, B.; Zhang, B.; Hu, R.; Zhou, X.; Cheng, Q. Thermal Routing via Near-Field Radiative Heat Transfer. *International Journal of Heat and Mass Transfer* **2020**, *150*, 119346.
(58) Xuan, Y. An Overview of Micro/Nanoscaled Thermal Radiation and Its Applications. *Photonics and Nanostructures - Fundamentals and Applications* **2014**, *12* (2), 93–113. https://doi.org/10.1016/j.photonics.2014.02.003.
(59) Goetzler, W.; Guernsey, M.; Young, J.; Fujrman, J.; Abdelaziz, A. *The Future of Air Conditioning for Buildings*; Navigant Consulting, Burlington, MA (United States), 2016. https://www.osti.gov/biblio/1420235 (accessed 2024-01-22).
(60) Li, Z.; Chen, W. Progress in Dynamic Emissivity Regulation: Control Methods, Material Systems, and Applications. *Mater. Chem. Front.* **2021**, *5* (17), 6315–6332. https://doi.org/10.1039/D1QM00624J.
(61) Zhao, H.; Sun, Q.; Zhou, J.; Deng, X.; Cui, J. Switchable Cavitation in Silicone Coatings for Energy-Saving Cooling and Heating. *Advanced Materials* **2020**, *32* (29), 2000870. https://doi.org/10.1002/adma.202000870.
(62) Mandal, J.; Du, S.; Dontigny, M.; Zaghib, K.; Yu, N.; Yang, Y. Li4Ti5O12: A Visible-to-Infrared Broadband Electrochromic Material for Optical and Thermal Management. *Advanced Functional Materials* **2018**, *28* (36), 1802180. https://doi.org/10.1002/adfm.201802180.
(63) Zhang, X. A.; Yu, S.; Xu, B.; Li, M.; Peng, Z.; Wang, Y.; Deng, S.; Wu, X.; Wu, Z.; Ouyang, M.; Wang, Y. Dynamic Gating of Infrared Radiation in a Textile. *Science* **2019**, *363* (6427), 619–623. https://doi.org/10.1126/science.aau1217.
(64) Lu, L.; Wu, Z.; Ji, C.; Song, M.; Feng, H.; Ma, X.; Jiang, Y. Effect of Fe Doping on Thermochromic Properties of VO2 Films. *J Mater Sci: Mater Electron* **2018**, *29* (7), 5501–5508. https://doi.org/10.1007/s10854-018-8518-1.
(65) Athanasopoulos, N.; Siakavellas, N. J. Programmable Thermal Emissivity Structures Based on Bioinspired Self-Shape Materials. *Sci Rep* **2015**, *5* (1), 17682. https://doi.org/10.1038/srep17682.
(66) Paik, T.; Hong, S.-H.; Gaulding, E. A.; Caglayan, H.; Gordon, T. R.; Engheta, N.; Kagan, C. R.; Murray, C. B. Solution-Processed Phase-Change VO_2 Metamaterials from Colloidal Vanadium Oxide (VO_x) Nanocrystals. *ACS Nano* **2014**, *8* (1), 797–806. https://doi.org/10.1021/nn4054446.
(67) Ohm, C.; Brehmer, M.; Zentel, R. Liquid Crystalline Elastomers as Actuators and Sensors. *Advanced Materials* **2010**, *22* (31), 3366–3387. https://doi.org/10.1002/adma.200904059.
(68) Wang, Y.; He, Q.; Wang, Z.; Zhang, S.; Li, C.; Wang, Z.; Park, Y.-L.; Cai, S. Liquid Crystal Elastomer Based Dexterous Artificial Motor Unit. *Advanced Materials* **2023**, *35* (17), 2211283. https://doi.org/10.1002/adma.202211283.
(69) Berszakiewicz, A.; Kasperczyk, J.; Sieroń, A.; Krasiński, Z.; Cholewka, A.; Stanek, A. The Effect of Compression Therapy on Quality of Life in Patients with Chronic Venous Disease: A Comparative 6-Month Study. *pdia* **2021**, *38* (3), 389–395. https://doi.org/10.5114/ada.2020.92277.
(70) Zarchi, K.; Jemec, G. B. E. Delivery of Compression Therapy for Venous Leg Ulcers. *JAMA Dermatol* **2014**, *150* (7), 730. https://doi.org/10.1001/jamadermatol.2013.7962.

(71) Todd, M. Compression Bandaging: Types and Skills Used in Practical Application. *Br J Nurs* **2011**, *20* (11), 681–687. https://doi.org/10.12968/bjon.2011.20.11.681.
(72) Webb, E.; Neeman, T.; Bowden, F. J.; Gaida, J.; Mumford, V.; Bissett, B. Compression Therapy to Prevent Recurrent Cellulitis of the Leg. *N Engl J Med* **2020**, *383* (7), 630–639. https://doi.org/10.1056/NEJMoa1917197.
(73) Keller, A.; Müller, M. L.; Calow, T.; Kern, I. K.; Schumann, H. Bandage Pressure Measurement and Training: Simple Interventions to Improve Efficacy in Compression Bandaging. *International Wound Journal* **2009**, *6* (5), 324–330. https://doi.org/10.1111/j.1742-481X.2009.00621.x.
(74) Mosti, G.; Cavezzi, A.; Partsch, H.; Urso, S.; Campana, F. Adjustable Velcro® Compression Devices Are More Effective than Inelastic Bandages in Reducing Venous Edema in the Initial Treatment Phase: A Randomized Controlled Trial. *European Journal of Vascular and Endovascular Surgery* **2015**, *50* (3), 368–374. https://doi.org/10.1016/j.ejvs.2015.05.014.
(75) Mosti, G.; Picerni, P.; Partsch, H. Compression Stockings with Moderate Pressure Are Able to Reduce Chronic Leg Oedema. *Phlebology* **2012**, *27* (6), 289–296. https://doi.org/10.1258/phleb.2011.011038.
(76) Kumar, B.; Das, A.; Alagirusamy, R. Study on Interface Pressure Generated by a Bandage Using *in Vitro* Pressure Measurement System. *Journal of the Textile Institute* **2013**, *104* (12), 1374–1383. https://doi.org/10.1080/00405000.2013.807020.
(77) Feldman, J. L.; Stout, N. L.; Wanchai, A.; Stewart, B. R.; Cormier, J. N.; Armer, J. M. Intermittent Pneumatic Compression Therapy: A Systematic Review. *Lymphology* **2012**, *45* (1), 13–25.
(78) Morris, R. J.; Woodcock, J. P. Intermittent Pneumatic Compression or Graduated Compression Stockings for Deep Vein Thrombosis Prophylaxis?: A Systematic Review of Direct Clinical Comparisons. *Annals of Surgery* **2010**, *251* (3), 393–396. https://doi.org/10.1097/SLA.0b013e3181b5d61c.
(79) Hakala, T.; Puolakka, A.; Nousiainen, P.; Vuorela, T.; Vanhala, J. Application of Air Bladders for Medical Compression Hosieries. *Textile Research Journal* **2018**, *88* (19), 2169–2181. https://doi.org/10.1177/0040517517716907.
(80) Rahimi, M.; Blaber, A. P.; Menon, C. Motorized Adaptive Compression System for Enhancing Venous Return: A Feasibility Study on Healthy Individuals. *Medical Engineering & Physics* **2017**, *50*, 65–74. https://doi.org/10.1016/j.medengphy.2017.10.005.
(81) Yang, S. T.; Ryu, J. W.; Park, S.-H.; Lee, Y. B.; Koo, S. H.; Park, Y.-L.; Lee, G. An Active Compression Sleeve with Variable Pressure Levels Using a Wire-Fabric Mechanism and a Soft Sensor. *Smart Mater. Struct.* **2019**, *28* (11), 114002. https://doi.org/10.1088/1361-665X/ab3f56.
(82) Pourazadi, S.; Ahmadi, S.; Menon, C. Towards the Development of Active Compression Bandages Using Dielectric Elastomer Actuators. *Smart Mater. Struct.* **2014**, *23* (6), 065007. https://doi.org/10.1088/0964-1726/23/6/065007.
(83) Ross, L. T. Intelligent Compression Wrap. US11154453B2, October 26, 2021. https://patents.google.com/patent/US11154453B2/en (accessed 2024-04-29).
(84) Kumar, B.; Hu, J.; Pan, N. Smart Medical Stocking Using Memory Polymer for Chronic Venous Disorders. *Biomaterials* **2016**, *75*, 174–181. https://doi.org/10.1016/j.biomaterials.2015.10.032.

(85) Ahmad, M.; Luo, J.; Miraftab, M. Feasibility Study of Polyurethane Shape-Memory Polymer Actuators for Pressure Bandage Application. *Science and Technology of Advanced Materials* **2012**, *13* (1), 015006. https://doi.org/10.1088/1468-6996/13/1/015006.
(86) Kumar, B.; Hu, J.; Pan, N.; Narayana, H. A Smart Orthopedic Compression Device Based on a Polymeric Stress Memory Actuator. *Materials & Design* **2016**, *97*, 222–229. https://doi.org/10.1016/j.matdes.2016.02.092.
(87) Narayana, H.; Hu, J.; Kumar, B.; Shang, S.; Han, J.; Liu, P.; Lin, T.; Ji, F.; Zhu, Y. Stress-Memory Polymeric Filaments for Advanced Compression Therapy. *J. Mater. Chem. B* **2017**, *5* (10), 1905–1916. https://doi.org/10.1039/C6TB03354G.
(88) Narayana, H.; Hu, J.; Kumar, B.; Shang, S.; Ying, M.; Young, R. J. Designing of Advanced Smart Medical Stocking Using Stress-Memory Polymeric Filaments for Pressure Control and Massaging. *Materials Science and Engineering: C* **2018**, *91*, 263–273. https://doi.org/10.1016/j.msec.2018.05.026.
(89) Alavi, A.; Sibbald, R. G.; Phillips, T. J.; Miller, O. F.; Margolis, D. J.; Marston, W.; Woo, K.; Romanelli, M.; Kirsner, R. S. What's New: Management of Venous Leg Ulcers. *Journal of the American Academy of Dermatology* **2016**, *74* (4), 643–664. https://doi.org/10.1016/j.jaad.2015.03.059.
(90) Jovanović, T.; Penava, Ž.; Vrljičak, Z. Impact of the Elastane Percentage on the Elastic Properties of Knitted Fabrics under Cyclic Loading. *Materials* **2022**, *15* (19), 6512. https://doi.org/10.3390/ma15196512.
(91) Murphree, R. W. Impairments in Skin Integrity. *Nursing Clinics of North America* **2017**, *52* (3), 405–417. https://doi.org/10.1016/j.cnur.2017.04.008.
(92) *Nutrition and Functional Foods for Healthy Aging*; Watson, R. R., Ed.; Academic Press: London San Diego Cambridge Oxford, 2017.
(93) Berliner, E.; Ozbilgin, B.; Zarin, D. A. A Systematic Review of Pneumatic Compression for Treatment of Chronic Venous Insufficiency and Venous Ulcers. *Journal of Vascular Surgery* **2003**, *37* (3), 539–544. https://doi.org/10.1067/mva.2003.103.
(94) Wienert, V.; Sick, H.; zur Mühlen, J. [Local thermal stress tolerance of human skin]. *Anasth Intensivther Notfallmed* **1983**, *18* (2), 88–90.
(95) Coelho Rezende, G.; O'Flynn, B.; O'Mahony, C. Smart Compression Therapy Devices for Treatment of Venous Leg Ulcers: A Review. *Adv Healthcare Materials* **2022**, *11* (17), 2200710. https://doi.org/10.1002/adhm.202200710.

Acknowledgements

Chapter 2, in full, is a reprint of the material as it appears in “Magnetic vitrimer-based soft robotics”, *Soft Matter*, 18.39, 2022, by Gaoweiang Dong, Qiguang He, Shengqiang Cai. The dissertation author was the primary investigator and first author of this paper.

Chapter 3 Autonomous thermal modulator based on gold film-coated liquid crystal elastomer

3.1 Introduction

Radiative cooling, a fundamental way to emit thermal radiation of an object to provide a cooling effect, has been recently intensively explored in the thermal management of households[48,49] and human body[50]. However, conventional materials, with their fixed emissivity, offer singular thermal functions[51]. This limitation highlights the need for materials that can dynamically adjust emissivity in response to environmental or applied stimuli[52,53] for applications such as thermal management[54], infrared imaging[55], and camouflage[56]. In response to this need, radiative modulation was introduced by controlling the thermal radiation emission from surfaces, which has considerable potential in temperature regulation[57] and reducing energy consumption for heating and cooling[58]. Numerous active and passive radiative modulation solutions are in development, often resulting from breakthroughs in material sciences[59].

Active radiative modulation strategies, characterized by their use of external stimuli to adjust emissivity dynamically, are by far the most common approaches for applications requiring dynamic thermal modulation. Their thermal responses can be controlled in real time according to the operational demands, offering a high degree of adaptability[60]. Some examples of active solutions include mechanically responsive surfaces, electrochromic materials, and humidity-responsive materials. For example, Zhao et al.[61] developed a switchable cavitation in silicone coating under mechanical stretch so that it has high infrared emissivity in the porous state and high solar transmittance in the transparent solid state. Mandal et al.[62] demonstrated a $Li_4Ti_5O_{12}$ electrochromic material with lithiated and delithiated states showing significant emittance

tunability in mid-infrared and long-infrared regimes, offering a versatile approach for thermal camouflage and temperature control. Moreover, Zhang et al.[63] introduced a textile capable of dynamically gating infrared radiation in response to changes in the relative humidity of the skin, leveraging carbon nanotube-coated fibers to modulate heat exchange under hot and wet conditions. Despite the advantages of active modulation, the approach also has its own limitations. The need for external stimuli for operation can lead to limited application and increased energy use, potentially negating the efficiency benefits[51]. Additionally, the complexity of these systems may result in higher costs[52] and maintenance requirements.

To complement the capabilities of active modulation, passive modulation strategies have been explored to offer an energy-efficient alternative. These strategies utilize the inherent properties of materials and their interaction with the environment to modulate emissivity without additional energy inputs. For example, Ono et al.[64] introduced a self-adaptive radiative cooling approach using the thermochromic material Vanadium dioxide (VO_2), which transitions between metallic and insulating states at its phase transition temperature, resulting in its emissivity change. Similarly, Cai et al.[65] utilized $Ge_2Sb_2Te_5$ (GST), another thermochromic material, to create a nonvolatile silicon carbide-based thermal emitter capable of adjusting its thermal emissivity in the mid-infrared range in response to environmental temperatures. Athanasopoulos et al.[65] developed a bilayer structure leveraging the mismatch in coefficients of thermal expansion to reveal high emissivity surfaces at higher temperatures, while serving as a reflective barrier at lower temperatures, introducing an innovative method for dynamic thermal regulation. Such passive systems can automatically adapt to temperature variations, providing a self-regulating mechanism for thermal management that simplifies system design and potentially

reduces operational costs[66]. However, the production of thermochromic-based modulators involves expensive equipment and complex processes, such as precisely controlling the VO_2 or GST composition, making them costly to manufacture. Additionally, the creation of reconfigurable structures demands precise engineering and control, posing challenges for scaling up and applying these solutions over large areas.

Herein, we introduce a passive and self-regulating radiative modulation solution to overcome existing limitations: a self-regulated thermal modulator utilizing gold film-coated liquid crystal elastomer (Au-LCE). LCE exhibits significant and reversible actuation strain through the phase transition between its nematic and isotropic states[67,68]. We used LCE as the temperature-responsive material and constructed a thermal modulator that can switch between "high thermal resistance" and "low thermal resistance" states in response to the environment temperature. Firstly, the LCE modulator contains an air pocket at lower temperatures to preserve heat and forms microcracks at higher temperatures to increase effective emissivity, enabling seamless transitions based on environmental temperature changes. Secondly, the design of the device emphasizes the ease of application and flexibility, allowing it to conform to various surface shapes. Despite up to 50% contraction of the LCE, the modulator's fixed outer dimensions allow for easy attachment to objects, expanding its range of applications. Thirdly, our manufacturing process, involving LCE sheet preparation and thin film metal deposition, followed by periodic attachment to a substrate, simplifies production and enhances scalability. Finally, by altering the liquid crystal mesogen, we achieved tunable nematic-isotropic transition temperature (T_{NI}), allowing the device to be customized for specific application requirements. This tunability provides more potential in passive thermal modulation design.

3.2 Results and discussion

3.2.1 Design concept of Au-LCE thermal modulator

The Au-LCE thermal modulator presents a solution by reversibly switching between "low thermal resistance" and "high thermal resistance" states in response to environmental temperature changes. This modulator enables a cooling state through actuation-induced microcracks that expose a high-emissivity polymer substrate, and a "high thermal resistance" state by closing these microcracks and forming a high thermal resistance air gap between the modulator and the target object.

An LCE film undergoes a reversible phase transition between nematic and isotropic states, influenced by temperature changes around T_{NI}. In its nematic state at lower temperatures, the LC mesogen orientation is aligned, while at higher temperature isotropic state, the mesogen orientation is random. This large and fully reversible actuation strain identifies LCE as a good candidate for temperature-sensitive applications. Additionally, the thin gold film coating does not hinder LCE actuation, which can be seen in the experimental images in **Figure 3.1**. We first measure the length of LCE and Au-LCE at 25 °C. Then, we heated up the sample to 90 °C and recorded the fully actuated length. The pictures show that the gold coating does not hinder LCE's actuation performance.

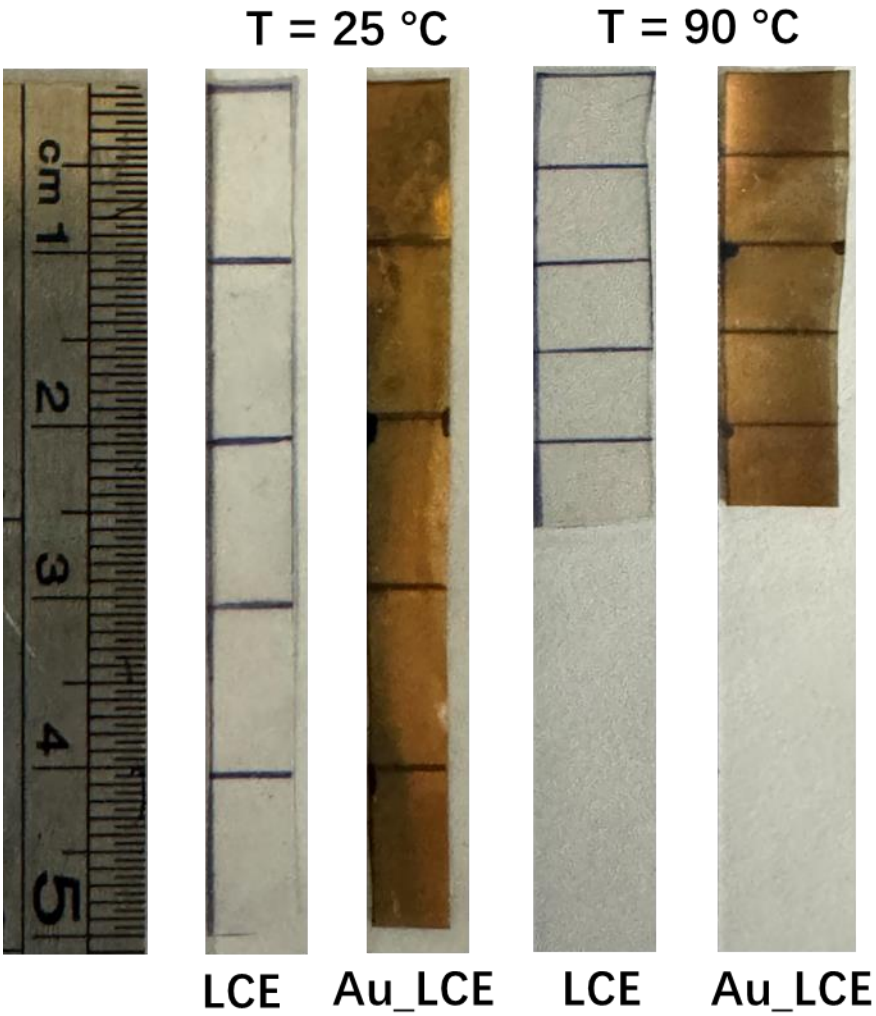

Figure 3.1 LCE and Au_LCE have same actuation behavior from 25 °C to 90 °C

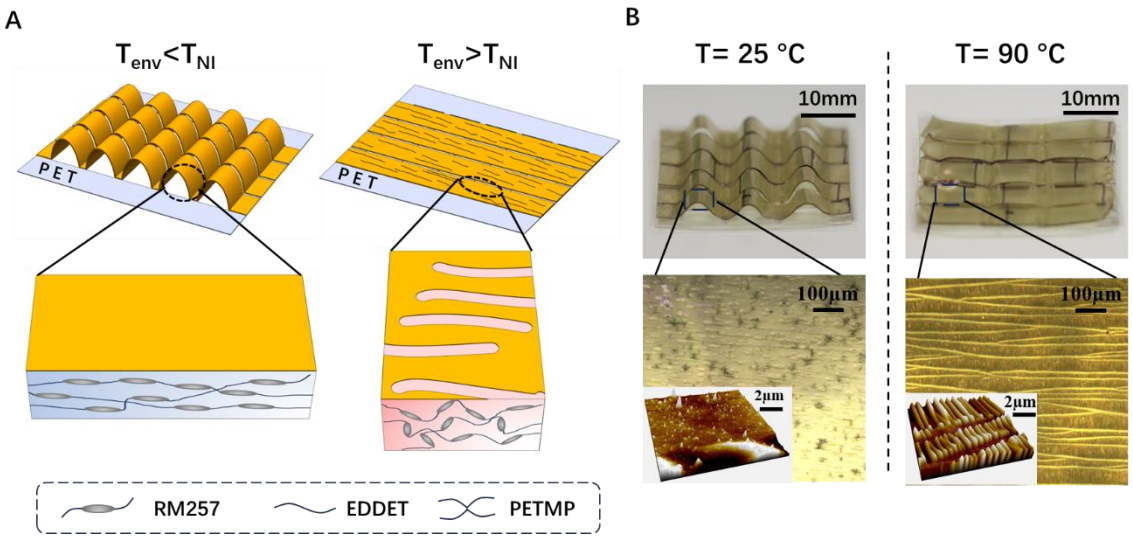

Figure 3.2 Design of an Au-LCE thermal modulator.
A) Structural reconfigurability, phase transition, and chemical composition of Au-LCE flexible autonomous thermal modulator. When the environmental temperature (T_{env}) is lower than the T_{NI}, the modulator turns into a high thermal resistance state by forming air pockets and being covered with low-emissivity continuous gold thin film. When the T_{env} is higher than the T_{NI}, the modulator turns into a low thermal resistance state by removing the air pockets and forming microcracks on the Au film to expose a high-emissivity polymer substrate. B) Experimental, optical microscope and AFM images of the Au-LCE thermal modulator, confirming the opening and closure of the microcracks.

LCE, similar to most polymers, has a high emissivity of around 0.95. In contrast, the coated smooth gold film has a low emissivity of around 0.05. As shown in **Figure 3.2A**, a gold-film-coated LCE thermal modulator is designed to actively respond to environmental temperature changes. When the temperature is low, the emissivity of the modulator is determined by the continuous gold film, which is small. The complete coverage of the LCE by the gold film can be confirmed by the optical microscopic images in Figure 1B. When the temperature is higher than T_{NI}, the monodomain LCE film contracts along the mesogen alignment direction and expands along the perpendicular direction. Such expansion is large enough to break the gold film coating and numerous microcracks appear, exposing the covered LCE to the air shown in **Figure 3.2A**. Along with atomic force microscope (AFM) images in **Figure 3.2B**, we can see the cracks

and wrinkles in Au film at high temperatures to accommodate the LCE actuation, demonstrating the modulator's dynamic response to temperature variations. As a result, the effective emissivity of the modulator increases. When the temperature is cooled again below the T_{NI}, LCE recovers back to its original shape and the cracks return to a continuous film, due to the reversible actuation of LCE.

Arch-shaped gold-film-coated LCE strips were mounted on a polyethylene terephthalate (PET) substrate, forming numerous small arches. For each individual arch, the LCE length (L) and the arch span (W) are tailored based on the LCE's actuation strain:

$$\frac{L-W}{L} = \varepsilon_a \quad (1)$$

, where the actuation strain ε_a is defined as the ratio of the change in length upon heating to the original length of the LCE. The design of the arch interspacing ensures that minimal shear force is applied to the adhesive points and substrate, maintaining the structural integrity and flatness of the substrate at elevated temperatures.

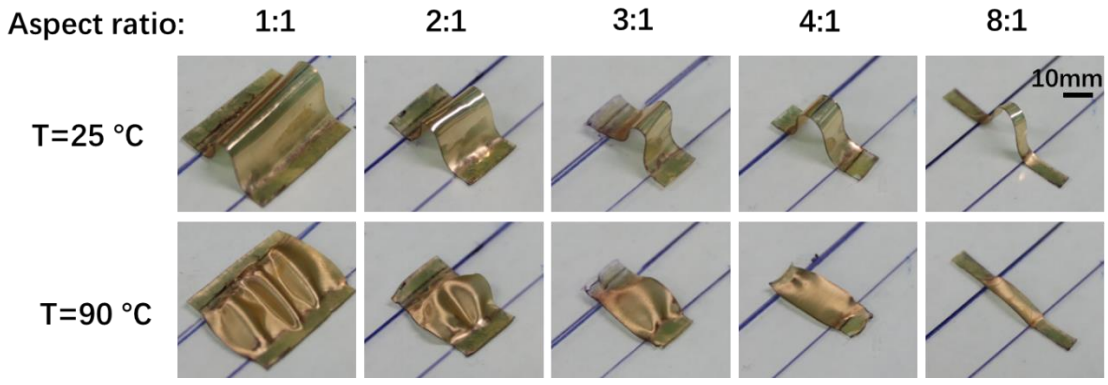

Figure 3.3 Au_LCE with aspect ratios from 1 to 8

As shown in **Figure 3.2B**, as the environmental temperature surpasses T_{NI}, the arch-shaped Au-LCE contracts into a flat configuration for good contact with the targeted cooling

object. To avoid the lateral buckling of the Au-LCE strip, we optimized the aspect ratio of the Au-LCE strip, defined by the strip width divided by the arch width, to be larger than 4. Detailed images of Au-LCE deformation across various aspect ratios can be found in **Figure 3.3**. To study the effect of aspect ratio on bonded Au-LCE strips, we fabricated Au-LCE samples with different aspect ratios, maintaining a constant thickness of 0.3mm for the film. The samples were bonded along the two indicator lines, mimicking the structure in the Au-LCE thermal modulator. The samples were then heated to 90 °C and cooled to 25 °C for multiple cycles. Representative photos were taken. **Figure 3.3** shows that when the aspect ratio exceeds 4, the Au-LCE strips do not exhibit buckling at elevated temperatures of 90 °C. We chose the aspect ratio equal to 4 for the study. When the environmental temperature is below T_{NI}, arch-shaped Au-LCE films introduce air pockets, which can effectively reduce the conduction heat transfer from the substrate to the Au-LCE. Therefore, the heat loss from the substrate to the environment is reduced, and the thermal resistance of the device is increased.

3.2.2 Thermal-mechanical characterization of Au-LCE thermal modulator

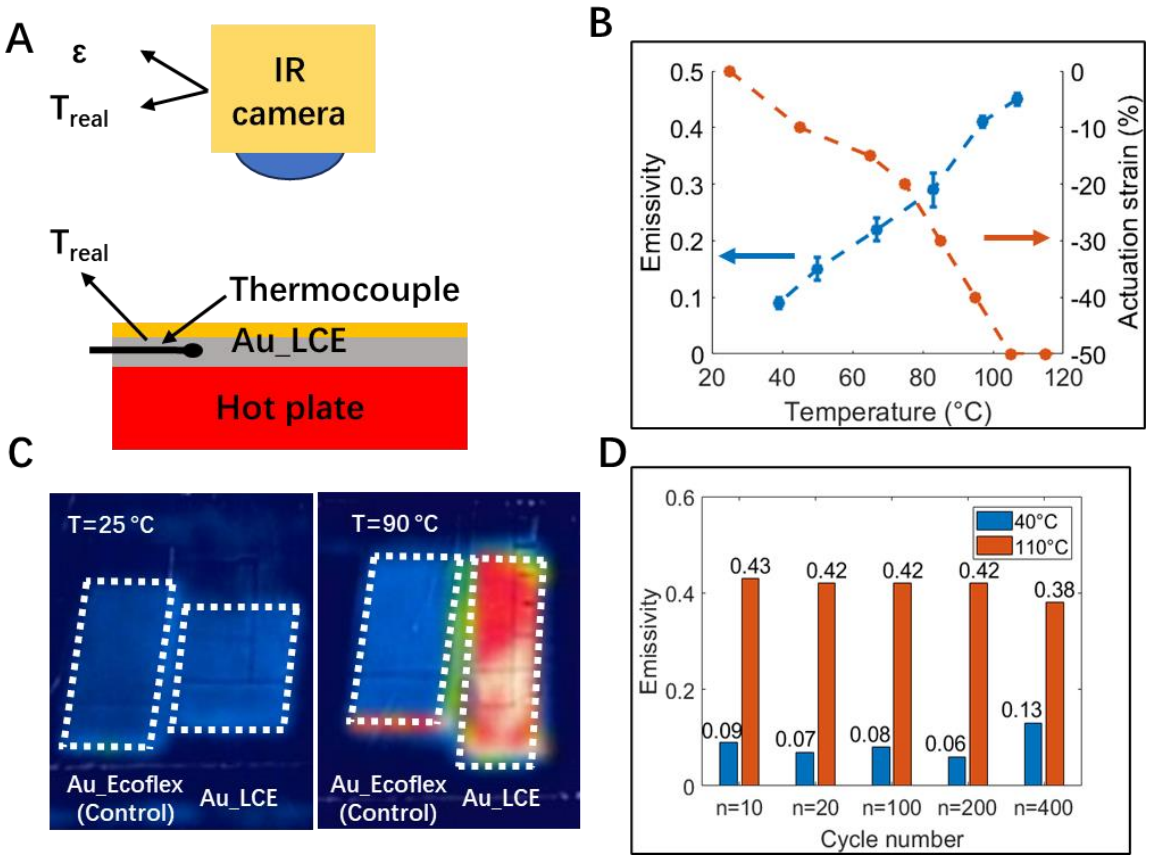

Figure 3.4 Thermal characterization of Au-LCE samples.
A) Experimental setup of emissivity measurement. B) Emissivity and actuation strain change of Au-LCE as a function of temperature. C) IR images showing emissivity change at different temperatures, blue and red indicate low and high emissivity, respectively, from the IR camera, with a copper background. D) Reversibility of the emissivity at 40 °C and 110 °C upon heating/cooling for 400 cycles.

Figure 3.4 shows the thermal characterizations of the Au-LCE thermal modulator, illustrating its ability to switch between cooling and non-cooling states based on environmental temperature changes. The emissivity measurement setup, constructed by following ASTM (E1933-14R22) standard and described in **Figure 3.4A**, involves tuning the emissivity setting in the IR camera to match the real temperature measured by a thermocouple (T_{real}), ensuring the

emissivity (ε) value displayed corresponds to the Au-LCE's emissivity. Figure 2B shows that as the temperature increases from 40 °C to 110 °C, the emissivity rises from 0.09 to 0.46, and the actuation strain increases from 0% to 50%. To further confirm that the change in the emissivity in response to temperature is a strain-dependent phenomenon, we conducted additional experiments by mechanically stretching the Au-LCE in both its nematic phase at 40 °C and isotropic phases at 110 °C to various strain values and then measuring the corresponding emissivity. The results of these experiments, shown in **Figure 3.5**, demonstrate that the emissivity of the Au-LCE remains consistent across different strains. We measured the emissivity value at various strains for nematic and isotropic phase LCE under 40 °C and 90 °C, respectively. The results show no obvious difference between the two samples, indicating this strain-induced emissivity change is independent of the LCE phase. This finding underscores the intrinsic relationship between the physical deformation of the Au-LCE strips and the thermal emissivity properties, confirming that the observed variations in emissivity with temperature are indeed due to the strain changes of the material rather than its phase transition. To achieve a large actuation strain of the LCE, we varied its chemical composition and measured actuation strains, as shown in **Figure 3.6**. In synthesizing the LCE, we measured several parameters: the length after initial crosslinking (l_0), the length when stretched before the second crosslinking (l_{hold}), the length after recovery from the second crosslinking (l_e), and the fully actuated length (l_c). We defined the curing strain, fixity, and actuation strain, as shown in **Figure 3.6A**. The PETMP percent is calculated based on the ratio of thiol groups from the crosslinker PETMP to those from the chain-extender EDDET. For instance, "11% PETMP" means the ratio $n_{SH\text{-}PETMP}/n_{SH\text{-}EDDET}$ is 11%. All other chemical compositions were kept constant.

Based on the results in **Figure 3.6B** and **Figure 3.6C**, we selected the 60% PETMP formulation for its high fixity and actuation strain. This decision was made to optimize the performance of the LCE for our thermal modulator application.

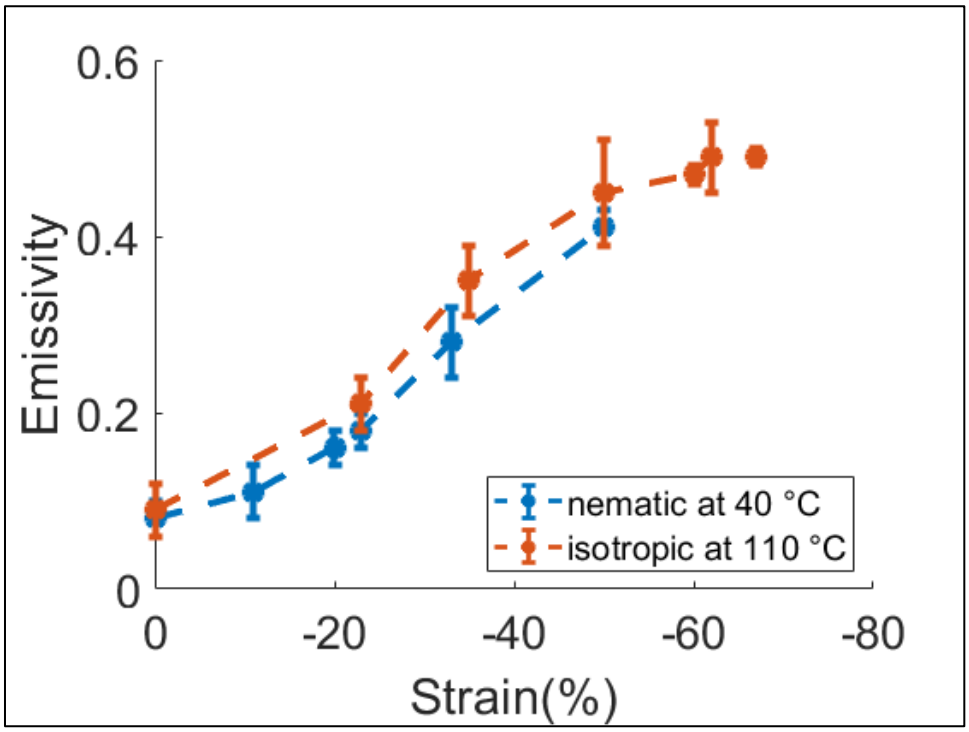

Figure 3.5 Emissivity change of Au_LCE with nematic and isotropic phase under constant temperature, respectively

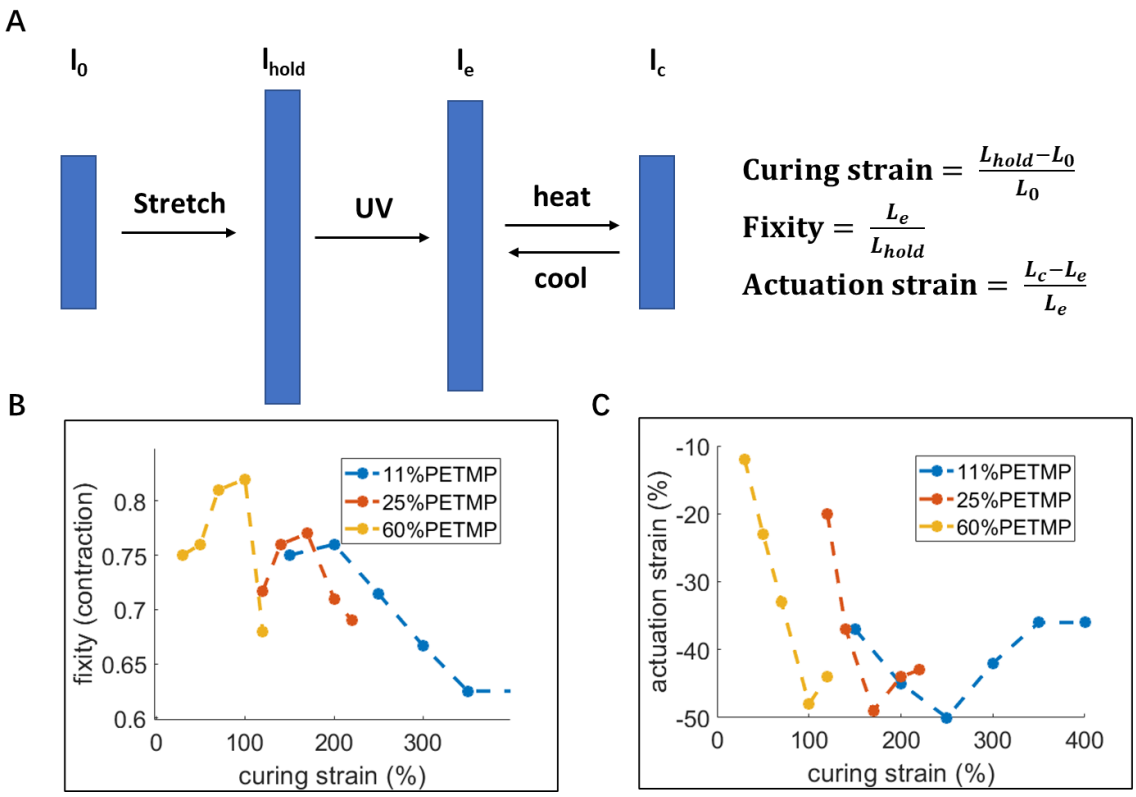

Figure 3.6 Fixity and actuation strain of LCE with different composition and curing strain. A) Definitions of cure strain, fixity, and actuation strain. B) contraction fixity of LCE as a function of curing strain. C) actuation strain of LCE as a function of curing strain

IR images in **Figure 3.4C** visually capture the change in emissivity at different temperatures. An Au-LCE sample and a gold-coated silicone rubber (Au-SR) as a control sample were placed next to each other on a uniformly heated hot copper (Cu) plate. SR does not undergo phase transition; thus the control sample maintained its low emissivity of Au from 25 to 90 °C, as shown by the constant blue color (low temperature) in the IR image. The color is similar to the Cu background for the entire temperature range due to the similar emissivity between Au and Cu. On the other hand, the Au-LCE sample underwent a transition from the same radiative temperature as the Cu background (blue color) at 25 °C to a much higher radiative temperature than the background (red color) at 90 °C, demonstrating the transition from low to high emissivity. **Figure 3.4D** illustrates the cyclability of the Au-LCE thermal modulator. The

modulator shows consistent performance for up to 200 cycles, with only a slight decrease in efficacy after 400 cycles. This durability is essential for practical applications, suggesting that the modulator can function reliably over extended periods and withstand multiple usage cycles without significant performance degradation.

The temperature-dependent thermal regulation of the Au-LCE thermal modulator can be tailored by modifying its T_{NI} and the sharpness of its thermotropic actuation. One way to tune the thermal response of the LCE is to change the LC mesogen in the LCE network.

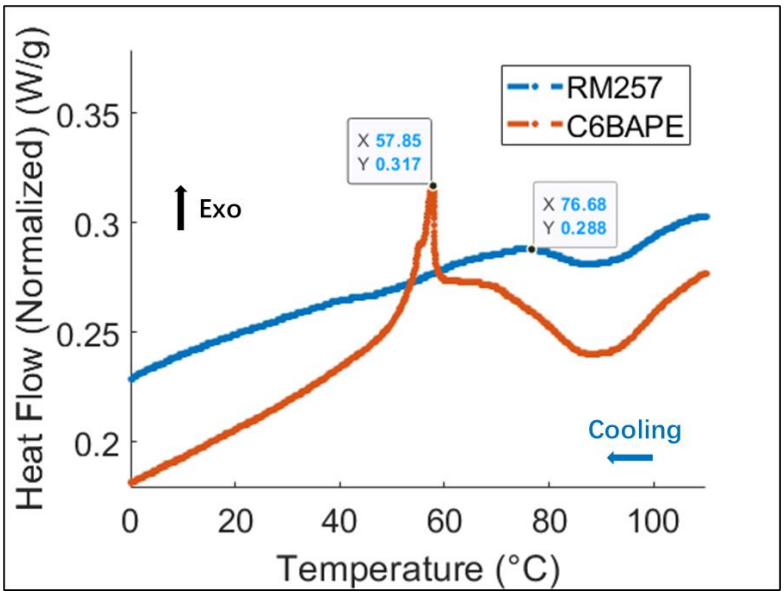

Figure 3.7 Differential Scanning Calorimetry (DSC) of LCEs consisting of RM257 and C6BAPE.

To demonstrate this, we synthesized LCEs using two different reactive LC mesogens: RM257 and C6BAPE, without changing the compositions of the other chemicals. The differential scanning calorimetry showed that LCEs with RM257 have T_{NI} around 76 °C and with C6BAPE have T_{NI} around 57 °C (**Figure 3.7**). The two mesogens have similar structures,

but mesogen-mesogen interaction for C6BAPE is weaker than RM257[46]. Therefore, C6BAPE-based LCE shows sharper phase transition and lower phase transition temperature.

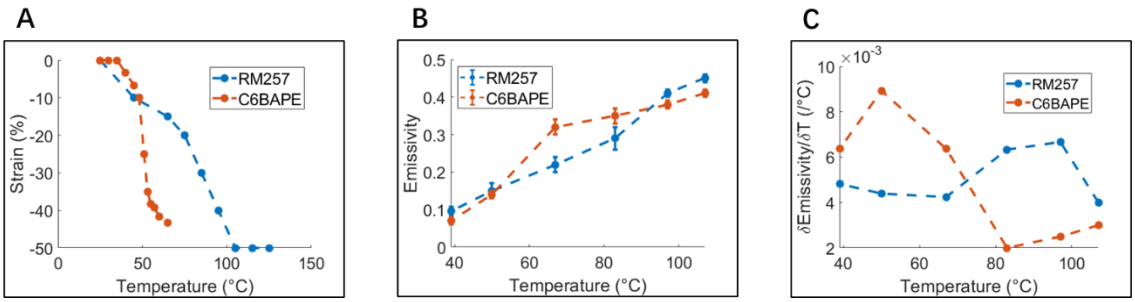

Figure 3.8 Mechanical and thermal characterization of Au-LCE with various T_{NI}.
A) Actuation strain vs temperature. B) Emissivity vs temperature. C) Emissivity change rate vs temperature

Figure 3.8A presents a comparative analysis of the actuation strain changing with temperature for the two LCEs. Both LCEs exhibit comparable magnitude of actuation strains, but C6BAPE-based LCE contracts at a lower temperature of around 55 °C, in contrast to RM257-based LCE showing significant actuation at the temperature of approximately 85 °C. **Figure 3.8B** illustrates that two different LCEs exhibit comparable changes in emissivity, even with varying T_{NI}. This suggests that adjusting the chemical composition of the LCE enhances the adaptability of the modulators while maintaining their cooling efficiency. **Figure 3.8C** analyzes the changing rate of the emissivity with temperature for the modulator based on the two LCEs. For the RM257-based LCE modulator, we observe that peak emissivity change occurs around 90 °C, while the C6BAPE-based modulator's peak is at about 55 °C.

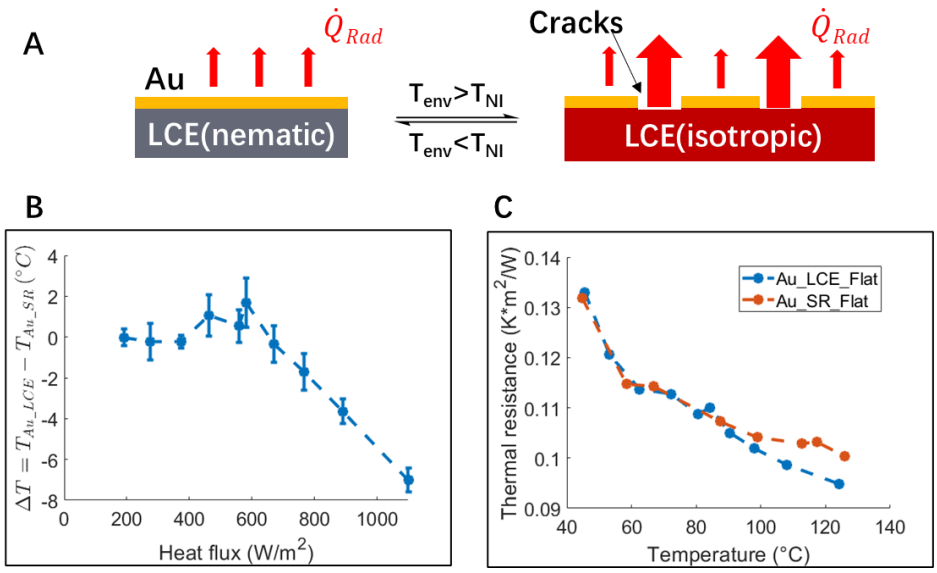

Figure 3.9 Thermal resistance of the thermal modulator with actuation-induced microcracks. A) Actuation-induced microcracks in the thermal modulator with temperature change. B) Temperature difference between the Au-coated LCE film and Au-coated silicone rubber film as a function of heat flux. With high heat flux, the temperature of the Au-coated LCE film is significantly lower than that of the Au-coated silicone rubber film. C) Thermal resistance as a function of temperature for Au-coated LCE film and Au-coated silicone rubber film. At high temperatures, the resistance of Au-coated LCE film is lower than that of the Au-coated silicone rubber film.

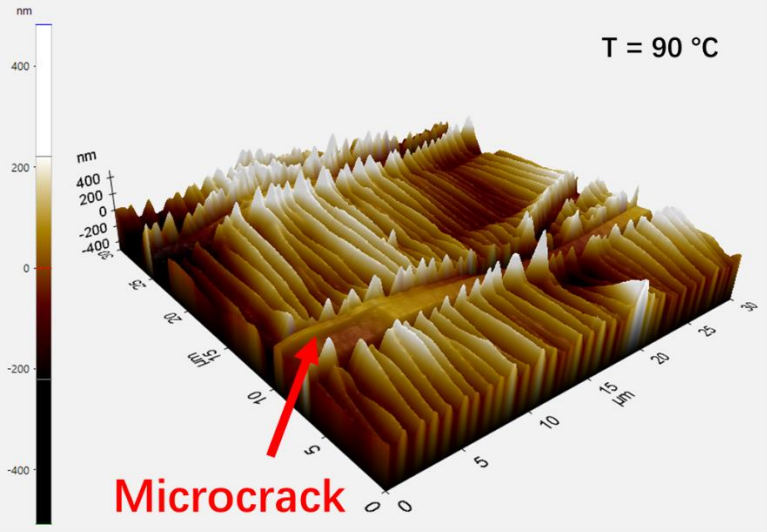

Figure 3.10 AFM images of quantitative measurement of actuation-induced microcrack in Au-LCE.

We next studied the thermal resistance changes of the gold-coated thermal modulator caused by microcracking and buckling mechanisms separately. When the temperature is higher than T_{NI}, the large expansion of the LCE breaks the coated gold film as shown in **Figure 3.9A**, exposing the high-emissivity polymer to the air and thus significantly increases the overall effective emissivity of the modulator. As the temperature decreases, the LCE returns to its original shape, causing the microcracks to close and the gold layer to fully cover the LCE once more.

The morphology of microcracks was further observed with AFM, which can be found in **Figure 3.10**. When the environmental temperature is above the T_{NI} of LCE, the LCE contracts along the mesogen alignment direction and expands in the perpendicular direction. The expansion of LCE breaks the gold film, and the 3D view of the AFM image shows the microcrack of a width of around 3 microns. From the AFM image, we can also see periodic wrinkles of a width of around 1 micron along the contraction direction of the LCE film.

To quantify the radiative cooling effect of the Au-LCE thermal modulator and separate it from the air-pocket effect, we compared the temperatures of a flat Au-LCE and a flat Au-SR placed on a copper block under varying input heat fluxes. The Au-SR serves as a control sample as it has negligible deformation with temperature changes. We define the temperature difference and thermal resistance as:

$$\Delta T = T_{Au-LCE} - T_{Au-SR} \quad , \tag{2}$$

$$R_{th} = \frac{T - T_{amb}}{\dot{Q}} \ . \tag{3}$$

where $\dot{Q}$ is the heat flux and T_{amb} = 20 °C is the ambient temperature.

As depicted in **Figure 3.9B**, the temperature of the Au-LCE samples begins to fall below that of Au-SR when the input heat flux is around 600 W/m^2, with the disparity enlarging with the heat flux. Temperature measurements as a function of heat flux for each sample can be found in **Figure 3.11**. When the heat flux is under 700W/m^2, the temperatures of Au-coated LCE film and Au-coated silicone rubber film are similar. When the heat flux is above 700W/m^2, the temperature of the Au-coated LCE film is significantly lower than that of the Au-coated silicone rubber film. **Figure 3.9C** further demonstrates a decreasing trend in the thermal resistance of the Au-LCE sample as the temperature increases past the T_{NI}, indicating enhanced radiative heat transfer to the environment due to emissivity increase. The comparative analysis with Au-SR underscores the Au-LCE cooling performance.

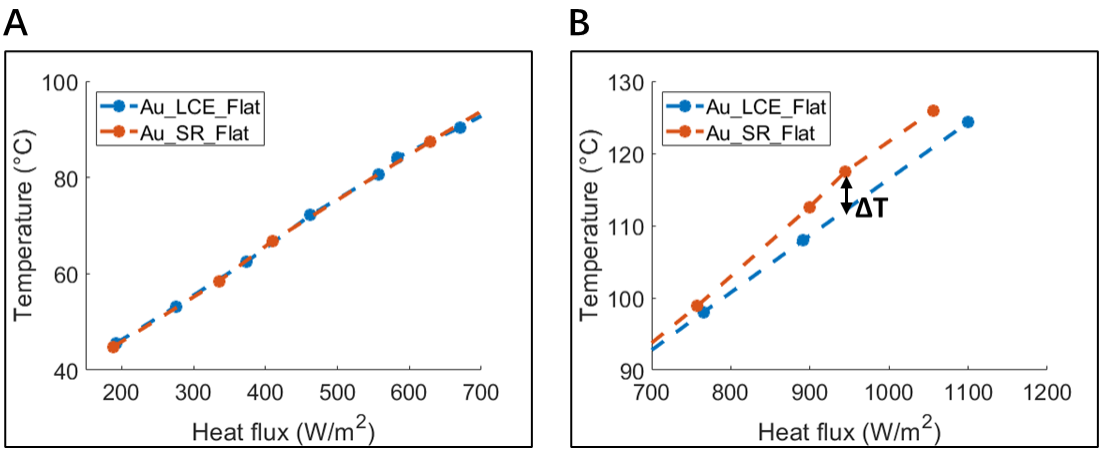

Figure 3.11 Temperatures of the Au-coated LCE film and Au-coated silicone rubber film as a function of heat flux.

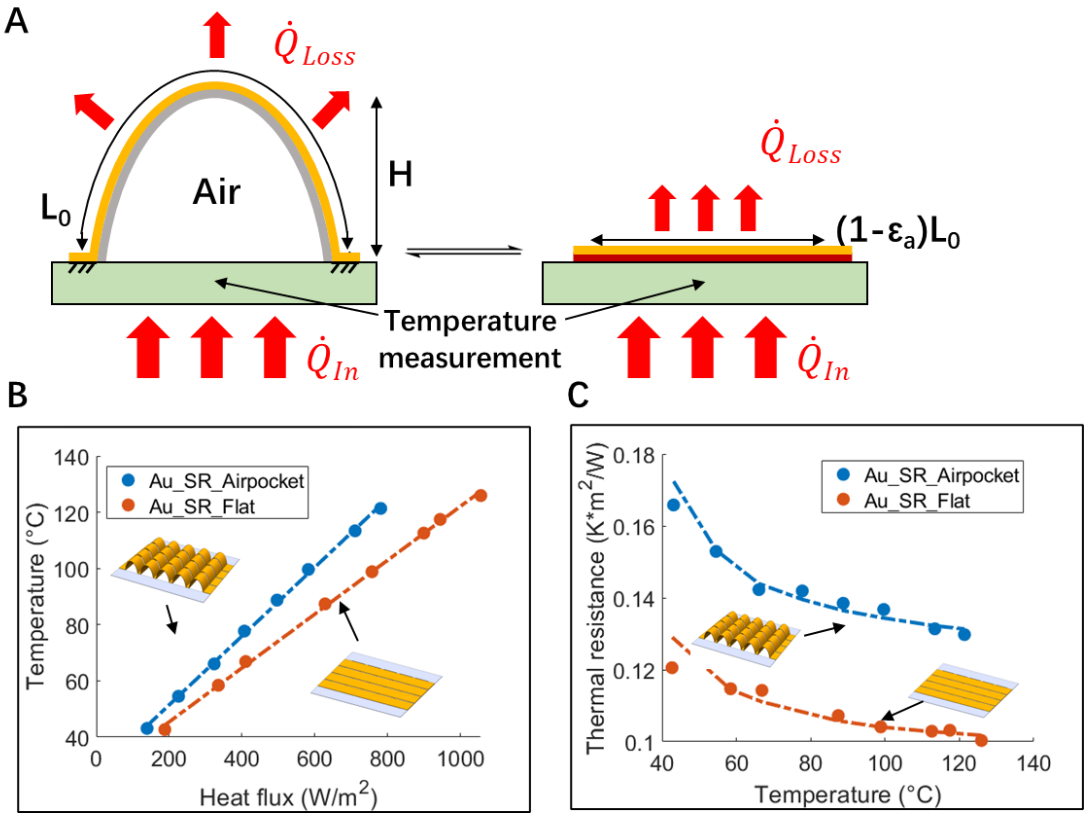

Figure 3.12 Thermal resistance of the thermal modulator with air pocket underneath the Au-LCE arch.
A) Actuation-induced air pocket formation in the thermal modulator with temperature change. B) Temperature of Au-coated SR film with air pockets and flat Au-coated SR film as a function of heat flux. The temperature of the Au-coated SR film with air pockets is significantly higher than that of the flat Au-coated SR film. C) Thermal resistance as a function of temperature for Au-coated SR film with air pockets and flat Au-coated SR film. At high temperatures, the resistance of Au-coated SR film with air pockets is higher than that of the flat Au-coated SR film.

Next, we study the effect of the air pockets. When the temperature decreases below the T_{NI}, the Au-LCE thermal modulator recovers back from the flat shape to the arch shape with an air pocket trapped between the film and the substrate. Meanwhile, the microcracks of the gold film close. As a consequence, at low temperature, the thermal resistance of the modulator increases due to the reduction of the emissivity of the film and also the formation of the trapped air. The air pockets under the arch-shaped Au-LCE act as an insulating barrier, significantly reducing heat transfer from the device to the environment. This insulation mechanism enables

the device to retain heat at lower temperatures, effectively nullifying the cooling effect. To further explore and quantify the thermal resistance change associated with the formation of air pockets, we conducted experiments comparing the temperature responses of an arch-shaped Au-SR with the same geometry as the arch-shaped Au-LCE sample, and a flat Au-SR sample under various input heat fluxes as shown in **Figure 3.12A**. As the SR does not undergo phase transition to introduce cracks in Au, these samples only differ in the presence of the air pockets. In **Figure 3.13**, we illustrate our experimental setup using a brass block (360 Brass) with a thermal conductivity of approximately 150 W/m-K as a substrate to simulate the target object. A heater, serving as the heat source, warms the entire assembly, mimicking an internal heat source. We placed a calibrated heat flux sensor (PHFS-01, FluxTeq) between the heater and the brass block, with our test samples (Au_LCE and Au_SR) covering the brass block's top surface. A K-type thermocouple is positioned between the heat flux sensor and the brass block to monitor the interfacial temperature. At the same time, another is embedded in the brass block to record the device temperature, which we use to assess the samples' performance. Lower device temperatures at a given heat flux indicate reduced thermal resistance from the brass block to the environment. To minimize heat loss, we placed a large Styrofoam block beneath the setup and surrounded the device with thick glass fiber insulation to prevent heat dissipation through forced convection from laboratory air conditioning. With the ambient temperature maintained at 21-22°C, we assume heat transfer through the brass block and the top layer polymer occurs solely via natural convection and radiative cooling. The resulting data, showing device temperature versus heat flux for different samples, is presented in **Figure 3.9**, **Figure 3.12**, and **Figure 3.14**.

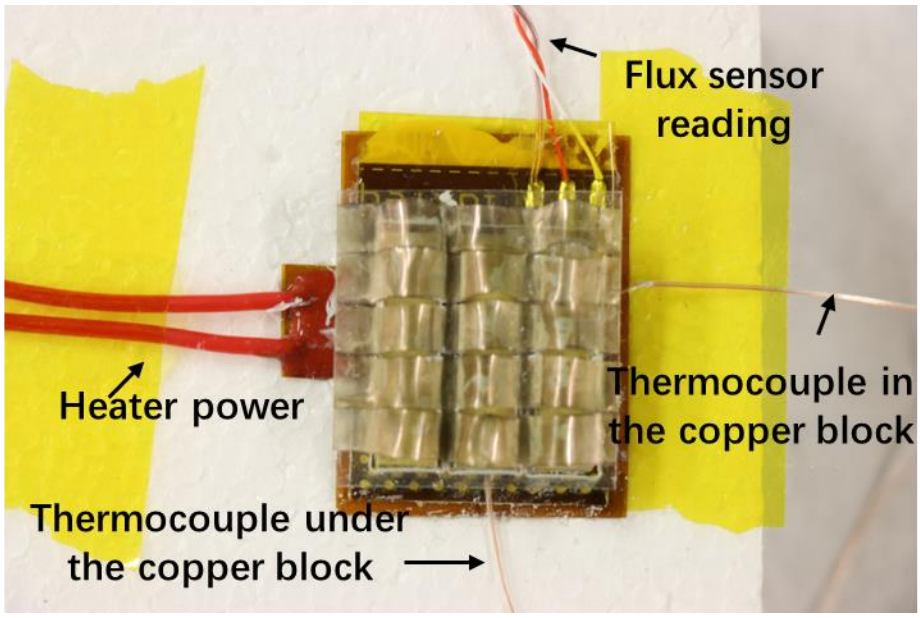

Figure 3.13 Experimental setup for the thermal measurement of which Figure 4, Figure 5, and Figure 6

As demonstrated in **Figure 3.12B**, the arch-shaped Au-SR sample consistently exhibited higher temperatures than its flat counterpart under identical heating conditions, confirming the effectiveness of the air pocket in reducing heat loss. Additionally, **Figure 3.12C** reveals an increase in thermal resistance in the presence of air pockets, further substantiating the role of these structural features in altering the thermal behavior of the Au-LCE thermal modulator.

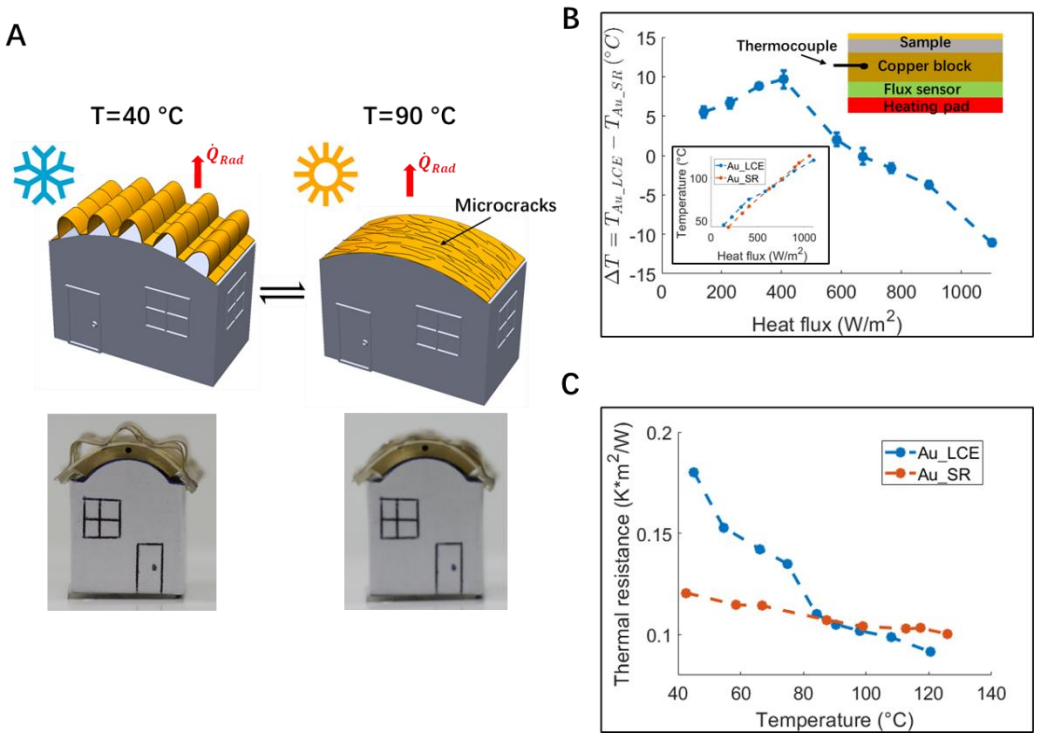

Figure 3.14
A) Schematics of the working concept of Au-coated LCE thermal modulator. B) Temperature of the object covered by Au-coated LCE modulator and the one covered by Au-coated silicon rubber. With low heat flux, the temperature of the object covered by an Au-coated LCE modulator is higher. With high heat flux, the temperature of the object covered by the Au-coated LCE modulator is lower. C) Effective thermal resistance of Au-coated LCE modulator and Au-coated silicon rubber as a function of temperature.

Finally, we demonstrated the performance of the Au-LCE thermal modulator under varying environmental temperatures. **Figure 3.14A** illustrates the modulator's behavior in response to changes in environmental temperature relative to T_{NI}. Below T_{NI}, the Au-LCE modulator retains its air pocket and remains fully enveloped by the film, showing high thermal resistance. Conversely, when the environmental temperature exceeds T_{NI}, the air pocket disappears, and microcracks develop in the gold layer, revealing the high emissivity LCE beneath and thus activating the cooling effect by enhancing radiative heat transfer to the environment.

To evaluate the comprehensive performance of the Au-LCE modulator, we conducted comparative tests against a flat Au-SR sample. The key distinction between the Au-LCE and Au-SR samples lies in the presence of an air pocket below T_{NI} and the formation of microcracks above T_{NI} in the Au-LCE sample. **Figure 3.14B** demonstrates that the Au-LCE thermal modulator is capable of efficiently conserving heat when the environmental temperature is below T_{NI} and effectively dissipating heat when the temperature rises above T_{NI}. As shown in **Figure 3.14C** this dual functionality is further validated by observing the thermal resistance differences between the two samples at varying temperatures, indicating the Au-LCE's superior thermal management capabilities.

This comparative analysis highlights the unique ability of the Au-LCE thermal modulator to adapt its thermal resistance based on environmental conditions via emissivity and structural changes, offering a versatile solution for thermal management that can toggle between heat preservation and heat dissipation as required.

3.3 Conclusion

This study has systematically explored the design, functionality, and thermal regulation capabilities of the Au-LCE thermal modulator, demonstrating an innovative approach to adaptive thermal management. We have shown that the Au-LCE modulator can effectively switch between “low thermal resistance” and “high thermal resistance” states in response to environmental temperature changes, a feature enabled by its unique material composition and structural design. The reversible transition of the Au-LCE, facilitated by the formation of microcracks in the gold layer at temperatures above the T_{NI} and the formation of insulating air

pockets below T_{NI}, underscores the modulator's ability to adapt its thermal properties dynamically. The modulator's flexibility, together with its fixed device's outer dimensions, broadens its applicability across various surface geometries. Our findings highlight the potential of the Au-LCE thermal modulator in diverse applications, from energy-efficient building materials to wearable technology that requires active temperature control. Future work will focus on optimizing the chemical composition and structural design of the Au-LCE to further enhance its thermal modulation capabilities.

3.4 Experimental secion

3.4.1 Materials

(1,4-bis-[4-(3-acryloyloxypropyloxy) benzoyloxy]-2-methylbenzene) (RM257, Chemfish, 97%), 4-(6-(acryloyloxy)hexyloxy)phenyl-4-(6- (acryloyloxy)hexyloxy)benzoate (C6BAPE, Chemfish, 97%), 2,2'-(ethylenedioxy) diethanethiol (EDDET; Sigma-Aldrich; 95%), pentaerythritol tetrakis (3-mercaptopropionate) (PETMP, Sigma-Aldrich, 95%), dipropylamine (DPA, Sigma-Aldrich, 98%), (2-hydroxyethoxy)-2-methylpropiophenone (HHMP; Sigma-Aldrich; 98%), silicon rubber (Dragon skin 30, Smooth-On), and all the solvents were used as received without further purification. All the chemical structures can be found in **Figure 3.15**.

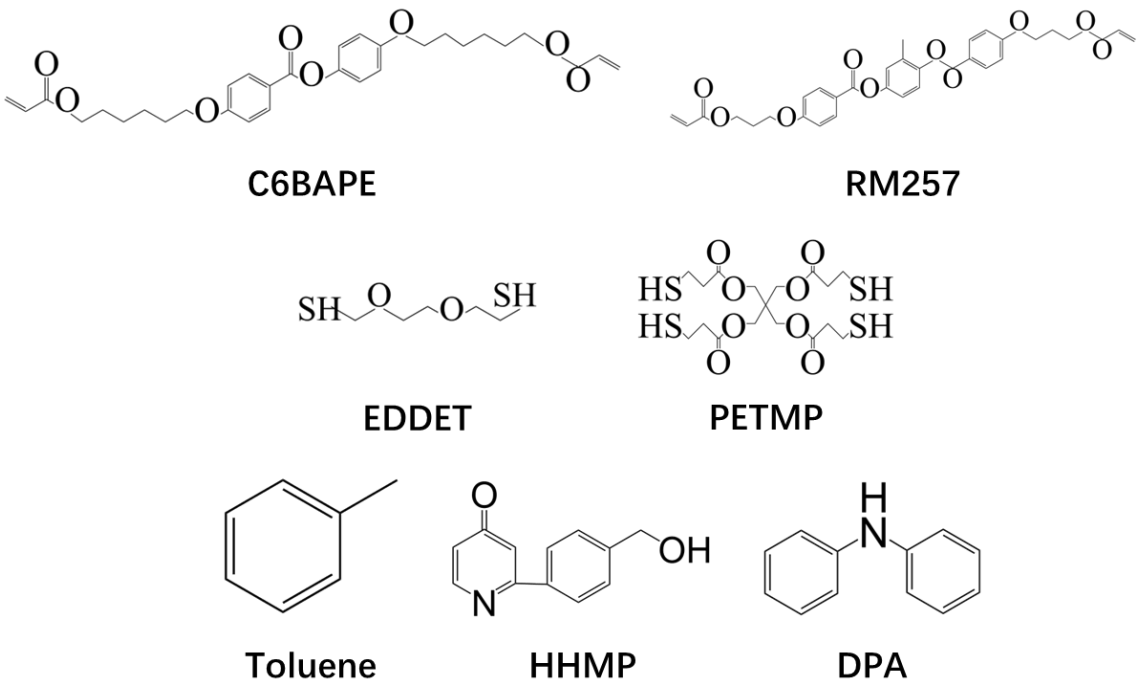

Figure 3.15 Chemical structures of all used chemicals

3.4.2 Fabrication of Au-LCE thermal modulator:

To prepare the LCE film, firstly, the monomer RM257 (10.0000 g) was dissolved in toluene (3.100 g) at 80 °C for 30 minutes. Secondly, sequentially add photo-initiator HHMP (0.0772 g), a mixture of chain extender EDDET (1.9018 g), crosslinker PETMP (1.5293 g) and catalyst DPA solution (1 wt%, 3.24 g). Thirdly, stir and degas the solution. Then, pour the solution into a compression-assisted mold for 24 hours in a dark environment. Finally, take out the loosely crosslinked LCE, apply the pre-stretch, and leave the LCE under UV (365nm) for 60 minutes to get monodomain LCE.

To prepare the Au-LCE thermal modulator, LCE films were placed inside a DC magnetron sputter deposition system (Denton Discovery 18) for gold sputtering. We then used a

CO_2 (H2, YH Laser) laser cutter to cut the PET (poly(ethylene terephthalate))as substrate. Finally, we used superglue (Loctite 495) to fix the Au-LCE on the PET substrate with a house-made spacer.

3.4.3 Characterization:

The atomic force microscopy was performed on NX20 (Park Systems) using NSC15 tips. Under tapping mode, the Z height information was used for reporting. The differential scanning calorimetry tests were performed on DSC250 (TA Instrument) with Tzero pans (901683.901, TA Instrument) and lids (901671.901, TA Instrument) under a ramp rate of 10 °C/min. The emissivity and IR pictures were measured and captured by adjusting the IR camera (C3-X, FLIR) emissivity setting till the temperature reading was the same as the actual temperature measured by a separate thermocouple. The measurements followed the ASTM (E1933-14R22) standard. The actuation strains were measured on a hot plate (Fristaden Lab). The videos and pictures were captured using a digital camera (Cannon EOS 80D). Thermal characterizations were performed using a DC power source (Dr. Meter PS-305DM), a flexible heating pad (5V, 1W) as the heating source, a calibrated heat flux sensor (PHFS-01, FluxTeq) between the heater and the brass block, and a multimeter (3478A, Hewlett Packard) to measure the heat flux, a brass block (360 Brass) with a thermal conductivity of approximately 150 W/m-K as the cooling target, a K-type thermocouple between the heat flux sensor and the brass block to monitor the interfacial temperature, another K-type thermocouple embedded in the brass block to record the device temperature, a large Styrofoam block beneath the setup, and thick glass fiber surrounding the

device to prevent heat dissipation through forced convection due to airflow from air condition in the environment.

3.5 Reference

(1) Wang, L.; Iida, F. Deformation in Soft-Matter Robotics: A Categorization and Quantitative Characterization. *IEEE Robot. Automat. Mag.* **2015**, *22* (3), 125–139. https://doi.org/10.1109/MRA.2015.2448277.

(2) Laschi, C.; Mazzolai, B.; Cianchetti, M. Soft Robotics: Technologies and Systems Pushing the Boundaries of Robot Abilities. *Sci. Robot.* **2016**, *1* (1), eaah3690. https://doi.org/10.1126/scirobotics.aah3690.

(3) Hao, Y.; Zhang, S.; Fang, B.; Sun, F.; Liu, H.; Li, H. A Review of Smart Materials for the Boost of Soft Actuators, Soft Sensors, and Robotics Applications. *Chin. J. Mech. Eng.* **2022**, *35* (1), 37. https://doi.org/10.1186/s10033-022-00707-2.

(4) Chen, Z.-J.; Gao, F.; Pan, Y. Novel Door-Opening Method for Six-Legged Robots Based on Only Force Sensing. *Chin. J. Mech. Eng.* **2017**, *30* (5), 1227–1238. https://doi.org/10.1007/s10033-017-0172-7.

(5) Carpentier, J.; Mansard, N. Multicontact Locomotion of Legged Robots. *IEEE Trans. Robot.* **2018**, *34* (6), 1441–1460. https://doi.org/10.1109/TRO.2018.2862902.

(6) Shian, S.; Bertoldi, K.; Clarke, D. R. Dielectric Elastomer Based "Grippers" for Soft Robotics. *Advanced Materials* **2015**, *27* (43), 6814–6819. https://doi.org/10.1002/adma.201503078.

(7) Mazzolai, B.; Margheri, L.; Cianchetti, M.; Dario, P.; Laschi, C. Soft-Robotic Arm Inspired by the Octopus: II. From Artificial Requirements to Innovative Technological Solutions. *Bioinspir. Biomim.* **2012**, *7* (2), 025005. https://doi.org/10.1088/1748-3182/7/2/025005.

(8) Shen, Q.; Wang, T.; Liang, J.; Wen, L. Hydrodynamic Performance of a Biomimetic Robotic Swimmer Actuated by Ionic Polymer–Metal Composite. *Smart Mater. Struct.* **2013**, *22* (7), 075035. https://doi.org/10.1088/0964-1726/22/7/075035.

(9) Keplinger, C.; Sun, J.-Y.; Foo, C. C.; Rothemund, P.; Whitesides, G. M.; Suo, Z. Stretchable, Transparent, Ionic Conductors. *Science* **2013**, *341* (6149), 984–987. https://doi.org/10.1126/science.1240228.

(10) Lee, E.; Kim, D.; Kim, H.; Yoon, J. Photothermally Driven Fast Responding Photo-Actuators Fabricated with Comb-Type Hydrogels and Magnetite Nanoparticles. *Sci Rep* **2015**, *5* (1), 15124. https://doi.org/10.1038/srep15124.

(11) Bassik, N.; Abebe, B. T.; Laflin, K. E.; Gracias, D. H. Photolithographically Patterned Smart Hydrogel Based Bilayer Actuators. *Polymer* **2010**, *51* (26), 6093–6098. https://doi.org/10.1016/j.polymer.2010.10.035.

(12) Shin, B.; Ha, J.; Lee, M.; Park, K.; Park, G. H.; Choi, T. H.; Cho, K.-J.; Kim, H.-Y. Hygrobot: A Self-Locomotive Ratcheted Actuator Powered by Environmental Humidity. *Sci. Robot.* **2018**, *3* (14), eaar2629. https://doi.org/10.1126/scirobotics.aar2629.

(13) Poojary, U. R.; Gangadharan, K. V. Material Modeling of Frequency, Magnetic Field and Strain Dependent Response of Magnetorheological Elastomer. *J Mater Sci* **2021**, *56* (28), 15752–15766. https://doi.org/10.1007/s10853-021-06307-0.
(14) Dong, G.; He, Q.; Cai, S. Magnetic Vitrimer-Based Soft Robotics. *Soft Matter* **2022**, *18* (39), 7604–7611. https://doi.org/10.1039/D2SM00893A.
(15) De Gennes, P.; Hébert, M.; Kant, R. Artificial Muscles Based on Nematic Gels. *Macromolecular Symposia* **1997**, *113* (1), 39–49. https://doi.org/10.1002/masy.19971130107.
(16) Brazel, C. S. Magnetothermally-Responsive Nanomaterials: Combining Magnetic Nanostructures and Thermally-Sensitive Polymers for Triggered Drug Release. *Pharm Res* **2009**, *26* (3), 644–656. https://doi.org/10.1007/s11095-008-9773-2.
(17) Thévenot, J.; Oliveira, H.; Sandre, O.; Lecommandoux, S. Magnetic Responsive Polymer Composite Materials. *Chem. Soc. Rev.* **2013**, *42* (17), 7099. https://doi.org/10.1039/c3cs60058k.
(18) Kuang, X.; Wu, S.; Ze, Q.; Yue, L.; Jin, Y.; Montgomery, S. M.; Yang, F.; Qi, H. J.; Zhao, R. Magnetic Dynamic Polymers for Modular Assembling and Reconfigurable Morphing Architectures. *Advanced Materials* **2021**, *33* (30), 2102113. https://doi.org/10.1002/adma.202102113.
(19) Kim, Y.; Yuk, H.; Zhao, R.; Chester, S. A.; Zhao, X. Printing Ferromagnetic Domains for Untethered Fast-Transforming Soft Materials. *Nature* **2018**, *558* (7709), 274–279. https://doi.org/10.1038/s41586-018-0185-0.
(20) Cheng, Y.; Chan, K. H.; Wang, X.-Q.; Ding, T.; Li, T.; Zhang, C.; Lu, W.; Zhou, Y.; Ho, G. W. A Fast Autonomous Healing Magnetic Elastomer for Instantly Recoverable, Modularly Programmable, and Thermorecyclable Soft Robots. *Advanced Functional Materials* **2021**, *31* (32), 2101825. https://doi.org/10.1002/adfm.202101825.
(21) Matxain, J. M.; Asua, J. M.; Ruipérez, F. Design of New Disulfide-Based Organic Compounds for the Improvement of Self-Healing Materials. *Phys. Chem. Chem. Phys.* **2016**, *18* (3), 1758–1770. https://doi.org/10.1039/C5CP06660C.
(22) Maeda, T.; Otsuka, H.; Takahara, A. Dynamic Covalent Polymers: Reorganizable Polymers with Dynamic Covalent Bonds. *Progress in Polymer Science* **2009**, *34* (7), 581–604. https://doi.org/10.1016/j.progpolymsci.2009.03.001.
(23) Ruff, Y.; Lehn, J. Glycodynamers: Dynamic Analogs of Arabinofuranoside Oligosaccharides. *Biopolymers* **2008**, *89* (5), 486–496. https://doi.org/10.1002/bip.20885.
(24) Otsuka, H.; Muta, T.; Sakada, M.; Maeda, T.; Takahara, A. Scrambling Reaction between Polymers Prepared by Step-Growth and Chain-Growth Polymerizations: Macromolecular Cross-Metathesis between 1,4-Polybutadiene and Olefin-Containing Polyester. *Chem. Commun.* **2009**, No. 9, 1073. https://doi.org/10.1039/b818014h.
(25) Guimard, N. K.; Oehlenschlaeger, K. K.; Zhou, J.; Hilf, S.; Schmidt, F. G.; Barner-Kowollik, C. Current Trends in the Field of Self-Healing Materials. *Macro Chemistry & Physics* **2012**, *213* (2), 131–143. https://doi.org/10.1002/macp.201100442.
(26) Bergman, S. D.; Wudl, F. Mendable Polymers. *J. Mater. Chem.* **2008**, *18* (1), 41–62. https://doi.org/10.1039/B713953P.
(27) Cordier, P.; Tournilhac, F.; Soulié-Ziakovic, C.; Leibler, L. Self-Healing and Thermoreversible Rubber from Supramolecular Assembly. *Nature* **2008**, *451* (7181), 977–980. https://doi.org/10.1038/nature06669.

(28) Burattini, S.; Colquhoun, H. M.; Fox, J. D.; Friedmann, D.; Greenland, B. W.; Harris, P. J. F.; Hayes, W.; Mackay, M. E.; Rowan, S. J. A Self-Repairing, Supramolecular Polymer System: Healability as a Consequence of Donor–Acceptor π–π Stacking Interactions. *Chem. Commun.* **2009**, No. 44, 6717. https://doi.org/10.1039/b910648k.
(29) Burnworth, M.; Tang, L.; Kumpfer, J. R.; Duncan, A. J.; Beyer, F. L.; Fiore, G. L.; Rowan, S. J.; Weder, C. Optically Healable Supramolecular Polymers. *Nature* **2011**, *472* (7343), 334–337. https://doi.org/10.1038/nature09963.
(30) Ritz, D.; Beckwith, J. Roles of Thiol-Redox Pathways in Bacteria. *Annu. Rev. Microbiol.* **2001**, *55* (1), 21–48. https://doi.org/10.1146/annurev.micro.55.1.21.
(31) Wedemeyer, W. J.; Welker, E.; Narayan, M.; Scheraga, H. A. Disulfide Bonds and Protein Folding. *Biochemistry* **2000**, *39* (15), 4207–4216. https://doi.org/10.1021/bi992922o.
(32) Spillmann, C. M.; Naciri, J.; Martin, B. D.; Farahat, W.; Herr, H.; Ratna, B. R. Stacking Nematic Elastomers for Artificial Muscle Applications. *Sensors and Actuators A: Physical* **2007**, *133* (2), 500–505. https://doi.org/10.1016/j.sna.2006.04.045.
(33) Zeng, H.; Wani, O. M.; Wasylczyk, P.; Kaczmarek, R.; Priimagi, A. Self-Regulating Iris Based on Light-Actuated Liquid Crystal Elastomer. *Advanced Materials* **2017**, *29* (30), 1701814. https://doi.org/10.1002/adma.201701814.
(34) Rogóż, M.; Zeng, H.; Xuan, C.; Wiersma, D. S.; Wasylczyk, P. Light-Driven Soft Robot Mimics Caterpillar Locomotion in Natural Scale. *Advanced Optical Materials* **2016**, *4* (11), 1689–1694. https://doi.org/10.1002/adom.201600503.
(35) Ahn, C.; Liang, X.; Cai, S. Inhomogeneous Stretch Induced Patterning of Molecular Orientation in Liquid Crystal Elastomers. *Extreme Mechanics Letters* **2015**, *5*, 30–36. https://doi.org/10.1016/j.eml.2015.09.007.
(36) Bisoyi, H. K.; Li, Q. Light-Driven Liquid Crystalline Materials: From Photo-Induced Phase Transitions and Property Modulations to Applications. *Chem. Rev.* **2016**, *116* (24), 15089–15166. https://doi.org/10.1021/acs.chemrev.6b00415.
(37) Boothby, J. M.; Kim, H.; Ware, T. H. Shape Changes in Chemoresponsive Liquid Crystal Elastomers. *Sensors and Actuators B: Chemical* **2017**, *240*, 511–518. https://doi.org/10.1016/j.snb.2016.09.004.
(38) Yakacki, C. M.; Saed, M.; Nair, D. P.; Gong, T.; Reed, S. M.; Bowman, C. N. Tailorable and Programmable Liquid-Crystalline Elastomers Using a Two-Stage Thiol–Acrylate Reaction. *RSC Adv.* **2015**, *5* (25), 18997–19001. https://doi.org/10.1039/C5RA01039J.
(39) Kotikian, A.; Truby, R. L.; Boley, J. W.; White, T. J.; Lewis, J. A. 3D Printing of Liquid Crystal Elastomeric Actuators with Spatially Programed Nematic Order. *Advanced Materials* **2018**, *30* (10), 1706164. https://doi.org/10.1002/adma.201706164.
(40) Wang, Z.; Wang, Z.; Zheng, Y.; He, Q.; Wang, Y.; Cai, S. Three-Dimensional Printing of Functionally Graded Liquid Crystal Elastomer. *Sci. Adv.* **2020**, *6* (39), eabc0034. https://doi.org/10.1126/sciadv.abc0034.
(41) He, Q.; Wang, Z.; Wang, Y.; Song, Z.; Cai, S. Recyclable and Self-Repairable Fluid-Driven Liquid Crystal Elastomer Actuator. *ACS Appl. Mater. Interfaces* **2020**, *12* (31), 35464–35474. https://doi.org/10.1021/acsami.0c10021.
(42) He, Q.; Wang, Z.; Song, Z.; Cai, S. Bioinspired Design of Vascular Artificial Muscle. *Adv Materials Technologies* **2019**, *4* (1), 1800244. https://doi.org/10.1002/admt.201800244.
(43) He, Q.; Wang, Z.; Wang, Y.; Minori, A.; Tolley, M. T.; Cai, S. Electrically Controlled Liquid Crystal Elastomer–Based Soft Tubular Actuator with Multimodal Actuation. *Sci. Adv.* **2019**, *5* (10), eaax5746. https://doi.org/10.1126/sciadv.aax5746.

(44) Wang, C.; Sim, K.; Chen, J.; Kim, H.; Rao, Z.; Li, Y.; Chen, W.; Song, J.; Verduzco, R.; Yu, C. Soft Ultrathin Electronics Innervated Adaptive Fully Soft Robots. *Advanced Materials* **2018**, *30* (13), 1706695. https://doi.org/10.1002/adma.201706695.
(45) Bauman, G. E.; McCracken, J. M.; White, T. J. Actuation of Liquid Crystalline Elastomers at or Below Ambient Temperature. *Angew Chem Int Ed* **2022**, *61* (28), e202202577. https://doi.org/10.1002/anie.202202577.
(46) McCracken, J. M.; Donovan, B. R.; Lynch, K. M.; White, T. J. Molecular Engineering of Mesogenic Constituents Within Liquid Crystalline Elastomers to Sharpen Thermotropic Actuation. *Adv Funct Materials* **2021**, *31* (16), 2100564. https://doi.org/10.1002/adfm.202100564.
(47) Shaha, R. K.; Torbati, A. H.; Frick, C. P. BODY-TEMPERATURE S HAPE-SHIFTING Liquid Crystal Elastomers. *J of Applied Polymer Sci* **2021**, *138* (14), 50136. https://doi.org/10.1002/app.50136.
(48) Sui, C.; Pu, J.; Chen, T.-H.; Liang, J.; Lai, Y.-T.; Rao, Y.; Wu, R.; Han, Y.; Wang, K.; Li, X.; Viswanathan, V.; Hsu, P.-C. Dynamic Electrochromism for All-Season Radiative Thermoregulation. *Nat Sustain* **2023**, *6* (4), 428–437. https://doi.org/10.1038/s41893-022-01023-2.
(49) Tang, K.; Dong, K.; Li, J.; Gordon, M. P.; Reichertz, F. G.; Kim, H.; Rho, Y.; Wang, Q.; Lin, C.-Y.; Grigoropoulos, C. P.; Javey, A.; Urban, J. J.; Yao, J.; Levinson, R.; Wu, J. Temperature-Adaptive Radiative Coating for All-Season Household Thermal Regulation. *Science* **2021**, *374* (6574), 1504–1509. https://doi.org/10.1126/science.abf7136.
(50) *Radiative human body cooling by nanoporous polyethylene textile | Science*. https://www.science.org/doi/10.1126/science.aaf5471 (accessed 2024-02-15).
(51) Wei, H.; Gu, J.; Ren, F.; Zhang, L.; Xu, G.; Wang, B.; Song, S.; Zhao, J.; Dou, S.; Li, Y. Smart Materials for Dynamic Thermal Radiation Regulation. *Small* **2021**, *17* (35), 2100446. https://doi.org/10.1002/smll.202100446.
(52) Ulpiani, G.; Ranzi, G.; Shah, K. W.; Feng, J.; Santamouris, M. On the Energy Modulation of Daytime Radiative Coolers: A Review on Infrared Emissivity Dynamic Switch against Overcooling. *Solar energy* **2020**, *209*, 278–301.
(53) Kats, M. A.; Sharma, D.; Lin, J.; Genevet, P.; Blanchard, R.; Yang, Z.; Qazilbash, M. M.; Basov, D. N.; Ramanathan, S.; Capasso, F. Ultra-Thin Perfect Absorber Employing a Tunable Phase Change Material. *Applied Physics Letters* **2012**, *101* (22), 221101. https://doi.org/10.1063/1.4767646.
(54) Zeng, S.; Shen, K.; Liu, Y.; Chooi, A. P.; Smith, A. T.; Zhai, S.; Chen, Z.; Sun, L. Dynamic Thermal Radiation Modulators via Mechanically Tunable Surface Emissivity. *Materials Today* **2021**, *45*, 44–53. https://doi.org/10.1016/j.mattod.2020.12.001.
(55) Schultz, P. H.; Hermalyn, B.; Colaprete, A.; Ennico, K.; Shirley, M.; Marshall, W. S. The LCROSS Cratering Experiment. *Science* **2010**, *330* (6003), 468–472. https://doi.org/10.1126/science.1187454.
(56) Xu, C.; Stiubianu, G. T.; Gorodetsky, A. A. Adaptive Infrared-Reflecting Systems Inspired by Cephalopods. *Science* **2018**, *359* (6383), 1495–1500. https://doi.org/10.1126/science.aar5191.
(57) Song, J.; Lu, L.; Li, B.; Zhang, B.; Hu, R.; Zhou, X.; Cheng, Q. Thermal Routing via Near-Field Radiative Heat Transfer. *International Journal of Heat and Mass Transfer* **2020**, *150*, 119346.

(58) Xuan, Y. An Overview of Micro/Nanoscaled Thermal Radiation and Its Applications. *Photonics and Nanostructures - Fundamentals and Applications* **2014**, *12* (2), 93–113. https://doi.org/10.1016/j.photonics.2014.02.003.
(59) Goetzler, W.; Guernsey, M.; Young, J.; Fujrman, J.; Abdelaziz, A. *The Future of Air Conditioning for Buildings*; Navigant Consulting, Burlington, MA (United States), 2016. https://www.osti.gov/biblio/1420235 (accessed 2024-01-22).
(60) Li, Z.; Chen, W. Progress in Dynamic Emissivity Regulation: Control Methods, Material Systems, and Applications. *Mater. Chem. Front.* **2021**, *5* (17), 6315–6332. https://doi.org/10.1039/D1QM00624J.
(61) Zhao, H.; Sun, Q.; Zhou, J.; Deng, X.; Cui, J. Switchable Cavitation in Silicone Coatings for Energy-Saving Cooling and Heating. *Advanced Materials* **2020**, *32* (29), 2000870. https://doi.org/10.1002/adma.202000870.
(62) Mandal, J.; Du, S.; Dontigny, M.; Zaghib, K.; Yu, N.; Yang, Y. Li4Ti5O12: A Visible-to-Infrared Broadband Electrochromic Material for Optical and Thermal Management. *Advanced Functional Materials* **2018**, *28* (36), 1802180. https://doi.org/10.1002/adfm.201802180.
(63) Zhang, X. A.; Yu, S.; Xu, B.; Li, M.; Peng, Z.; Wang, Y.; Deng, S.; Wu, X.; Wu, Z.; Ouyang, M.; Wang, Y. Dynamic Gating of Infrared Radiation in a Textile. *Science* **2019**, *363* (6427), 619–623. https://doi.org/10.1126/science.aau1217.
(64) Lu, L.; Wu, Z.; Ji, C.; Song, M.; Feng, H.; Ma, X.; Jiang, Y. Effect of Fe Doping on Thermochromic Properties of VO2 Films. *J Mater Sci: Mater Electron* **2018**, *29* (7), 5501–5508. https://doi.org/10.1007/s10854-018-8518-1.
(65) Athanasopoulos, N.; Siakavellas, N. J. Programmable Thermal Emissivity Structures Based on Bioinspired Self-Shape Materials. *Sci Rep* **2015**, *5* (1), 17682. https://doi.org/10.1038/srep17682.
(66) Paik, T.; Hong, S.-H.; Gaulding, E. A.; Caglayan, H.; Gordon, T. R.; Engheta, N.; Kagan, C. R.; Murray, C. B. Solution-Processed Phase-Change VO_2 Metamaterials from Colloidal Vanadium Oxide (VO_x) Nanocrystals. *ACS Nano* **2014**, *8* (1), 797–806. https://doi.org/10.1021/nn4054446.
(67) Ohm, C.; Brehmer, M.; Zentel, R. Liquid Crystalline Elastomers as Actuators and Sensors. *Advanced Materials* **2010**, *22* (31), 3366–3387. https://doi.org/10.1002/adma.200904059.
(68) Wang, Y.; He, Q.; Wang, Z.; Zhang, S.; Li, C.; Wang, Z.; Park, Y.-L.; Cai, S. Liquid Crystal Elastomer Based Dexterous Artificial Motor Unit. *Advanced Materials* **2023**, *35* (17), 2211283. https://doi.org/10.1002/adma.202211283.
(69) Berszakiewicz, A.; Kasperczyk, J.; Sieroń, A.; Krasiński, Z.; Cholewka, A.; Stanek, A. The Effect of Compression Therapy on Quality of Life in Patients with Chronic Venous Disease: A Comparative 6-Month Study. *pdia* **2021**, *38* (3), 389–395. https://doi.org/10.5114/ada.2020.92277.
(70) Zarchi, K.; Jemec, G. B. E. Delivery of Compression Therapy for Venous Leg Ulcers. *JAMA Dermatol* **2014**, *150* (7), 730. https://doi.org/10.1001/jamadermatol.2013.7962.
(71) Todd, M. Compression Bandaging: Types and Skills Used in Practical Application. *Br J Nurs* **2011**, *20* (11), 681–687. https://doi.org/10.12968/bjon.2011.20.11.681.
(72) Webb, E.; Neeman, T.; Bowden, F. J.; Gaida, J.; Mumford, V.; Bissett, B. Compression Therapy to Prevent Recurrent Cellulitis of the Leg. *N Engl J Med* **2020**, *383* (7), 630–639. https://doi.org/10.1056/NEJMoa1917197.

(73) Keller, A.; Müller, M. L.; Calow, T.; Kern, I. K.; Schumann, H. Bandage Pressure Measurement and Training: Simple Interventions to Improve Efficacy in Compression Bandaging. *International Wound Journal* **2009**, *6* (5), 324–330. https://doi.org/10.1111/j.1742-481X.2009.00621.x.
(74) Mosti, G.; Cavezzi, A.; Partsch, H.; Urso, S.; Campana, F. Adjustable Velcro® Compression Devices Are More Effective than Inelastic Bandages in Reducing Venous Edema in the Initial Treatment Phase: A Randomized Controlled Trial. *European Journal of Vascular and Endovascular Surgery* **2015**, *50* (3), 368–374. https://doi.org/10.1016/j.ejvs.2015.05.014.
(75) Mosti, G.; Picerni, P.; Partsch, H. Compression Stockings with Moderate Pressure Are Able to Reduce Chronic Leg Oedema. *Phlebology* **2012**, *27* (6), 289–296. https://doi.org/10.1258/phleb.2011.011038.
(76) Kumar, B.; Das, A.; Alagirusamy, R. Study on Interface Pressure Generated by a Bandage Using *in Vitro* Pressure Measurement System. *Journal of the Textile Institute* **2013**, *104* (12), 1374–1383. https://doi.org/10.1080/00405000.2013.807020.
(77) Feldman, J. L.; Stout, N. L.; Wanchai, A.; Stewart, B. R.; Cormier, J. N.; Armer, J. M. Intermittent Pneumatic Compression Therapy: A Systematic Review. *Lymphology* **2012**, *45* (1), 13–25.
(78) Morris, R. J.; Woodcock, J. P. Intermittent Pneumatic Compression or Graduated Compression Stockings for Deep Vein Thrombosis Prophylaxis?: A Systematic Review of Direct Clinical Comparisons. *Annals of Surgery* **2010**, *251* (3), 393–396. https://doi.org/10.1097/SLA.0b013e3181b5d61c.
(79) Hakala, T.; Puolakka, A.; Nousiainen, P.; Vuorela, T.; Vanhala, J. Application of Air Bladders for Medical Compression Hosieries. *Textile Research Journal* **2018**, *88* (19), 2169–2181. https://doi.org/10.1177/0040517517716907.
(80) Rahimi, M.; Blaber, A. P.; Menon, C. Motorized Adaptive Compression System for Enhancing Venous Return: A Feasibility Study on Healthy Individuals. *Medical Engineering & Physics* **2017**, *50*, 65–74. https://doi.org/10.1016/j.medengphy.2017.10.005.
(81) Yang, S. T.; Ryu, J. W.; Park, S.-H.; Lee, Y. B.; Koo, S. H.; Park, Y.-L.; Lee, G. An Active Compression Sleeve with Variable Pressure Levels Using a Wire-Fabric Mechanism and a Soft Sensor. *Smart Mater. Struct.* **2019**, *28* (11), 114002. https://doi.org/10.1088/1361-665X/ab3f56.
(82) Pourazadi, S.; Ahmadi, S.; Menon, C. Towards the Development of Active Compression Bandages Using Dielectric Elastomer Actuators. *Smart Mater. Struct.* **2014**, *23* (6), 065007. https://doi.org/10.1088/0964-1726/23/6/065007.
(83) Ross, L. T. Intelligent Compression Wrap. US11154453B2, October 26, 2021. https://patents.google.com/patent/US11154453B2/en (accessed 2024-04-29).
(84) Kumar, B.; Hu, J.; Pan, N. Smart Medical Stocking Using Memory Polymer for Chronic Venous Disorders. *Biomaterials* **2016**, *75*, 174–181. https://doi.org/10.1016/j.biomaterials.2015.10.032.
(85) Ahmad, M.; Luo, J.; Miraftab, M. Feasibility Study of Polyurethane Shape-Memory Polymer Actuators for Pressure Bandage Application. *Science and Technology of Advanced Materials* **2012**, *13* (1), 015006. https://doi.org/10.1088/1468-6996/13/1/015006.
(86) Kumar, B.; Hu, J.; Pan, N.; Narayana, H. A Smart Orthopedic Compression Device Based on a Polymeric Stress Memory Actuator. *Materials & Design* **2016**, *97*, 222–229. https://doi.org/10.1016/j.matdes.2016.02.092.

(87) Narayana, H.; Hu, J.; Kumar, B.; Shang, S.; Han, J.; Liu, P.; Lin, T.; Ji, F.; Zhu, Y. Stress-Memory Polymeric Filaments for Advanced Compression Therapy. *J. Mater. Chem. B* **2017**, *5* (10), 1905–1916. https://doi.org/10.1039/C6TB03354G.
(88) Narayana, H.; Hu, J.; Kumar, B.; Shang, S.; Ying, M.; Young, R. J. Designing of Advanced Smart Medical Stocking Using Stress-Memory Polymeric Filaments for Pressure Control and Massaging. *Materials Science and Engineering: C* **2018**, *91*, 263–273. https://doi.org/10.1016/j.msec.2018.05.026.
(89) Alavi, A.; Sibbald, R. G.; Phillips, T. J.; Miller, O. F.; Margolis, D. J.; Marston, W.; Woo, K.; Romanelli, M.; Kirsner, R. S. What's New: Management of Venous Leg Ulcers. *Journal of the American Academy of Dermatology* **2016**, *74* (4), 643–664. https://doi.org/10.1016/j.jaad.2015.03.059.
(90) Jovanović, T.; Penava, Ž.; Vrljičak, Z. Impact of the Elastane Percentage on the Elastic Properties of Knitted Fabrics under Cyclic Loading. *Materials* **2022**, *15* (19), 6512. https://doi.org/10.3390/ma15196512.
(91) Murphree, R. W. Impairments in Skin Integrity. *Nursing Clinics of North America* **2017**, *52* (3), 405–417. https://doi.org/10.1016/j.cnur.2017.04.008.
(92) *Nutrition and Functional Foods for Healthy Aging*; Watson, R. R., Ed.; Academic Press: London San Diego Cambridge Oxford, 2017.
(93) Berliner, E.; Ozbilgin, B.; Zarin, D. A. A Systematic Review of Pneumatic Compression for Treatment of Chronic Venous Insufficiency and Venous Ulcers. *Journal of Vascular Surgery* **2003**, *37* (3), 539–544. https://doi.org/10.1067/mva.2003.103.
(94) Wienert, V.; Sick, H.; zur Mühlen, J. [Local thermal stress tolerance of human skin]. *Anasth Intensivther Notfallmed* **1983**, *18* (2), 88–90.
(95) Coelho Rezende, G.; O'Flynn, B.; O'Mahony, C. Smart Compression Therapy Devices for Treatment of Venous Leg Ulcers: A Review. *Adv Healthcare Materials* **2022**, *11* (17), 2200710. https://doi.org/10.1002/adhm.202200710.

Acknowledgements

Chapter 3, in full, is a reprint of the material as it appears in "Autonomous thermal modulator based on gold film-coated liquid crystal elastomer", submitted, by Gaoweiang Dong, Tianshi Feng, Renkun Chen, Shengqiang Cai. The dissertation author was the primary investigator and first author of this paper.

Chapter 4 Liquid crystal elastomer for compression therapy

4.1 Introduction

Compression therapy, a widely used treatment method, involves applying consistent pressure to the limbs or other body parts using specially designed garments, bandages, or devices. The applied pressure facilitates better blood flow and lymphatic drainage, supporting the natural healing processes in the body. The therapy is commonly used for managing a wide range of disorders, including chronic venous diseases, edema, and conditions associated with poor blood circulation. The key to effective compression therapy is applying the appropriate level of pressure for a specified duration[69]. Inadequate pressure can delay treatment, while excessive pressure may cause pain or tissue damage[70].

Traditional compression therapies primarily utilize either inelastic bandages or elastic stockings. While inelastic compression bandaging offers low cost and versatile application, it relies heavily on the skill of the nurse and may lose elasticity over time [71,72]. For instance, Keller et al.[73] carried out research involving 21 nurses to assess their precision in applying inelastic compression bandages. The findings indicated that 34.9% of the applications resulted in inadequate sub-bandage pressure levels when the application was only based on the experience of the nurses. Elastic stockings, easier to apply and more patient-friendly, depend significantly on limb size for effective pressure application. Moreover, as the swelling in the treated limb decreases, the limb's diameter reduces and consequently, both inelastic bandages and elastic stockings, experience a reduction in applied pressure as they conform to the smaller limb size[74]. For example, Mosti et al.[75] conducted a study on pressure reduction during deswelling in 30 patients with chronic leg edema. The findings revealed that the minimum pressure drop observed

was 21%, resulting from a 10% reduction in calf circumference. Such pressure drop is undesired since a proper level of compression over the wounded area ensures more effective compression treatment for venous leg ulcers and oedema reduction[76].

To enhance pressure control and compliance with the bandage/stocking, researchers have explored dynamic compression therapy devices incorporating an actuating component. Moreover, by adopting actuators, dynamic compression therapy can be realized with intermittent pressure cycles, which was shown to be more efficient than static compression[77,78]. Pneumatic compression has been extensively studied as a dynamic compression therapy device, capable of delivering precise and dynamic pressure to the limb. For instance, Hakala et al.[79] employed adjustable air bladders in their design of a compression stocking, enabling fast pressure change within a few seconds. However, these devices are bulky, noisy, and usually not portable. Dynamic compression therapy devices utilizing motor-driven mechanisms can produce substantial torque and demonstrate rapid actuation speeds. For instance, Rahimi et al.[80] created a motorized compression bandage that incorporates tensioning wires capable of exerting pressures up to 87.3 mmHg. Nonetheless, integrating the motor into a compression garment poses challenges, particularly when applying high torque[81]. Shape memory alloys (SMA) provide the advantage of seamless textile integration and a low-profile design. For example, Duvall et al. developed a dynamic compression vest that employs shape memory alloy and achieved compression pressure up to 52.5 mmHg. However, the operational temperature of SMA typically exceeds human body temperature by tens of degrees, potentially posing risks during extended use. Additionally, motor-driven-based and SMA-based compression therapy devices mentioned

are inherently rigid actuators, which reduce their compliance and comfort as wearable devices for humans.

Recently, soft actuating polymers have been explored in constructing dynamic compression therapy devices. Pourazadi et al.[82] utilized dielectric elastomeric actuators (DEA) to develop a dynamic compression bandage that allows for precise pressure control. However, the pressure variation of the device is limited to less than 10 mmHg, and it operates at a high voltage exceeding 2 kV, raising safety concerns. Ross et al.[83] developed a compression device based on liquid crystal elastomer, consisting of a microprocessor, an active layer, a stimuli layer, and an insulation layer. However, the working temperature of liquid crystal elastomer exceeds human body temperature by over 30°C, and the fabrication and performance of the device have not been carefully studied. Shape memory polymers (SMP) have recently emerged as promising materials for smart compression therapy due to their significant actuation stress and inherent softness. Kumar et al.[84] and Ahmad et al.[85] developed an SMP-based compression therapy device and demonstrated around 10 mmHg increase of interfacial pressure with increasing temperature. However, these devices exhibited notable stress relaxation, exceeding 40%, which could undermine their therapeutic efficacy. To address the issue of stress relaxation, Kumar et al.[86] and Narayana et al.[87,88] implemented a preconditioning step in their SMP-based devices, significantly reducing stress relaxation and ensuring minimal pressure decay during dynamic compression treatment. Despite this advancement, each intermittent pressure cycle is over half an hour and the required preconditioning time of at least one hour before application poses practical challenges, limiting the immediate usability and convenience of SMP-based compression therapies. More

importantly, most shape memory polymers turn to glassy states at room temperature, which is stiff and difficult to wear.

Herein, we introduce room-temperature responsive liquid crystal elastomer (LCE) as an innovative material for both static and dynamic compression therapy applications. The unique composition of LCE, comprising liquid crystal mesogen, chain extender, and crosslinker, endows it with distinct mechanical and thermomechanical properties that distinguish it from conventional elastomers. LCEs can be synthesized in two states: polydomain, with randomly oriented mesogen domains, and monodomain, with aligned mesogens.

For static compression therapy, we proposed polydomain LCE as the elastic material due to its unique soft elasticity. It demonstrates a stress-strain curve with a stress plateau and negligible hysteresis in loading and unloading cycles. Consequently, a static stocking made from polydomain LCE can maintain a constant pressure within a large range of stretch, offering a significant range for application error compared to inelastic bandages and accommodating a variety of limb sizes compared to elastic stockings. Moreover, the negligible hysteresis of polydomain LCE during loading and unloading allows the LCE-based static stocking to maintain a steady pressure as the limb circumference decreases due to the deswelling. Additionally, the negligible stress relaxation and good cyclability of polydomain LCE permit the maintenance of the pressure level without requiring external energy or additional tightening steps, which is a notable advantage over other compression devices.

For dynamic compression therapy, monodomain LCE presents promising characteristics due to its reversible thermal actuation properties. Upon heating slightly above human body temperature, a monodomain LCE undergoes a nematic-isotropic phase transition, enabling it to exert substantial actuation stress when the displacement is fixed. By incorporating a power supply, a sensing unit, a controller, and a stretchable heater into the monodomain LCE-based stocking, it can achieve intermittent compression cycles, enhancing therapeutic efficacy. More importantly, monodomain LCE maintains its actuation properties over 1000 cycles, exhibiting minimal stress relaxation and superior durability compared to traditional shape memory polymers.

4.2 Results and discussion

4.2.1 Design concept:

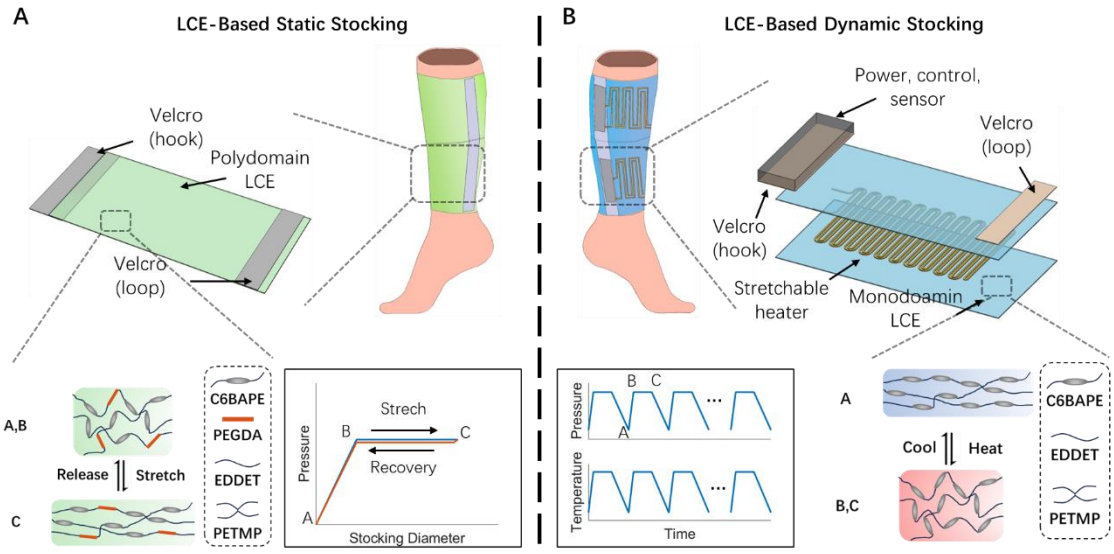

Figure 4.1 Design concept and working mechanisms of static and dynamic LCE-based compression stockings.
A) LCE-based static stocking consists of polydomain LCE and Velcro strips. As the deformation of the LCE is between state B and state C, the pressure remains nearly constant, corresponding to the liquid crystal mesogen rotation in the elastomer, as shown in the molecular schematics. B) Dynamic LCE-based compression stocking consists of monodomain LCE, stretchable heater, PCS module, and Velcro strips. With periodic voltage input, the LCE-based dynamic stocking can generate a cyclic, consistent, and controlled pressure profile within the human-comfort temperature range. The pressure increase from state A to state B is due to the nematic-isotropic phase transition of LCE, as shown in the molecular schematic.

As shown in **Figure 4.1A**, we employed polydomain LCE for static compression therapy, distinguishing itself from previously used materials, including inelastic bandages and elastic stockings. Firstly, when polydomain LCE is subjected to uniaxial stretch, its stress initially increases with strain, followed by a stress plateau over a wide range of strain. This property enables the LCE-based static stocking to maintain a constant pressure level (**Figure 4.1A**), demonstrating a high tolerance for application error compared to traditional inelastic bandages.

Moreover, LCE-based static stockings can easily accommodate various limb sizes while providing similar interfacial pressure. This is in contrast to the conventional solutions where the stress in the material increases with strain monotonically so that the desired pressure level is hard to maintain for various limb sizes.

Secondly, polydomain LCE with carefully tailored composition shows negligible stress reduction during unloading due to the extremely small mechanical hysteresis compared to conventional stocking materials (**Figure 4.1A**). Such feature of polydomain LCE can be important as the swollen leg starts to deswell after the application of the compression stocking. When traditional compression materials are used, a decrease in limb size often leads to a significant drop in applied pressure, which may diminish the treatment's effectiveness[75]. In contrast, polydomain LCE can maintain a stable pressure level despite the changes in limb size. The ability to maintain constant pressure during both application and size reduction allows the LCE-based static stocking to provide adequate compression across various limb sizes, providing a novel solution compared to conventional materials.

Finally, polydomain LCE demonstrates additional characteristics that make it suitable for static compression therapy. Notably, it maintains its stress level throughout the duration of its application, which typically spans a few hours. Furthermore, LCE exhibits a consistent stress profile across hundreds of usage cycles.

As illustrated in **Figure 4.1B**, monodomain LCE has merits in dynamic compression therapy due to its thermomechanical properties. We constructed a LCE-based dynamic stocking

using monodomain LCE and a heating element. We also developed a Power, Control, Sensor (PCS) module to control the LCE-based dynamic stocking and collect pressure, temperature, and voltage data. The monodomain LCE exhibits reversible actuation stress in response to temperature changes across the nematic-isotropic transition temperature (T_{NI}). By adjusting the chemical composition of the LCE, we tuned the T_{NI} to slightly above human body temperature, allowing the LCE-based dynamic stocking to generate sufficient interfacial pressure for therapeutic purposes[69] upon a mild increase in temperature. The application of periodic voltage enables the stocking to generate compression cycles consistently, maintaining adequate pressure without decay over time. Additionally, we 1employed pressure feedback mechanisms to regulate the interfacial pressure profile, permitting the controllability of the pressure profile throughout each compression cycle.

We fabricated the heating element from a thin copper film and precisely shaped it using a contour cutter to ensure its geometry provides a uniform temperature distribution. The heater can withstand moderate stretching and compression, maintaining consistent performance through thousands of operational cycles without noticeable changes in its electrical resistance. The entire device is portable and powered and controlled by a module that integrates battery, microcontroller, pressure sensor, and temperature sensor, providing real-time data to optimize therapy effectiveness.

4.2.2 LCE-based static stocking

4.2.2.1 Stress-strain relationship of polydomain LCE

We first examined the mechanical properties of polydomain LCE at 33 °C, a temperature close to that of human skin. The mechanical characterization of LCE under this temperature can provide necessary guidance to the design of static stockings. To identify the chemical composition of an LCE that exhibits a stress plateau and minimal hysteresis, we substituted a portion of rigid liquid crystal mesogen C6BAPE with a more flexible backbone, PEGDA.

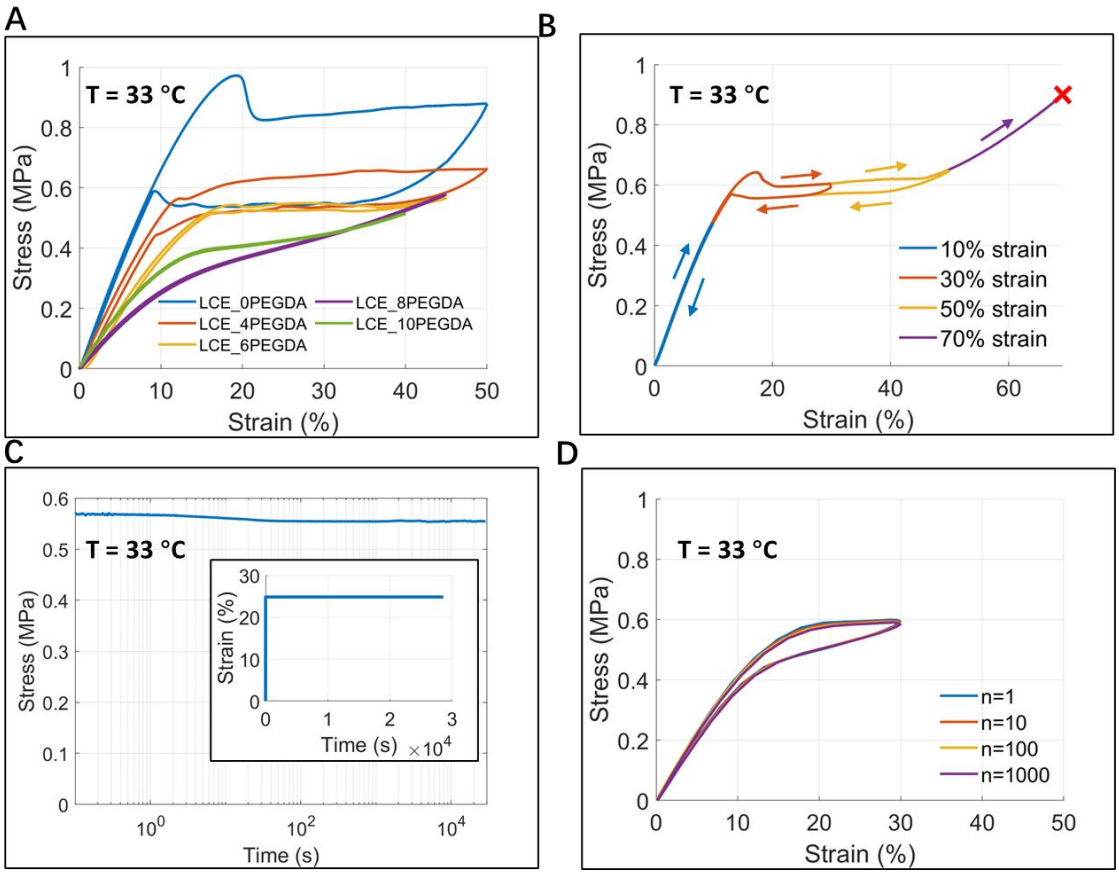

Figure 4.2 Stress-strain characterization of polydomain LCE at 33 °C.
A) Loading and unloading of a polydomain LCE with various PEGDA content. B) Loading and unloading of polydomain LCE at various strain values where LCE breaks during the 70% strain loading. C) Stress relaxation of polydomain LCE under 30% applied strain. D) Durability characterization of a polydomain LCE.

The loading and unloading of various polydomain LCE samples at 33 °C, depicted in **Figure 4.2A**, demonstrates how increasing PEGDA content influences the hysteresis loop and plateau behavior. Specifically, the number in the sample name represents the acrylate group percentage from PEGDA. For example, 'LCE_4PEGDA' indicates that the PEGDA contributes 4% of the total acrylate groups among all the chemicals.The chemical composition of the following samples are:

LCE_0PEGDA: $2n_{C6BAPE}$: $2n_{PEGDA}$: $3n_{TAC}$: $4n_{PETMP}$: $2n_{EDDET}$=0.90:0.00:0.1:0.5:0.5

LCE_4PEGDA: $2n_{C6BAPE}$: $2n_{PEGDA}$: $3n_{TAC}$: $4n_{PETMP}$: $2n_{EDDET}$=0.86:0.04:0.1:0.5:0.5

LCE_6PEGDA: $2n_{C6BAPE}$: $2n_{PEGDA}$: $3n_{TAC}$: $4n_{PETMP}$: $2n_{EDDET}$=0.84:0.06:0.1:0.5:0.5

LCE_8PEGDA: $2n_{C6BAPE}$: $2n_{PEGDA}$: $3n_{TAC}$: $4n_{PETMP}$: $2n_{EDDET}$=0.82:0.08:0.1:0.5:0.5

LCE_10PEGDA: $2n_{C6BAPE}$: $2n_{PEGDA}$: $3n_{TAC}$: $4n_{PETMP}$: $2n_{EDDET}$=0.80:0.10:0.1:0.5:0.5.

As the PEGDA content increases from the LCE_0PEGDA to the LCE_10EPGDA sample, we can observe the area of the hysteresis loop and plateau value decrease and eventually disappear for the LCE_6PEGDA sample. As a result, we selected LCE_6PEGDA for the LCE-based static stocking due to its demonstrated stress plateau and reduced hysteresis loop, which are advantageous for accommodating application errors, fitting various limb sizes, and mitigating pressure reduction associated with limb deswelling.

As shown in **Figure 4.2B**, we conducted loading and unloading tensile tests of the LCE_6PEGDA sample at various strain levels. During the loading of the LCE sample, the stress first increases with strain and then reaches a stress plateau around 0.6 MPa, followed by a further increase in stress and eventually fails. Polydomain LCE exhibits elastic deformation, which is

usually desired for static compression stocking[89]. **Figure 4.2C** presents the stress relaxation behavior of polydomain LCE when subjected to a 25% strain and maintained for around 8 hours, showing minimal stress relaxation and indicating the ability of the material to sustain pressure within the stocking. We further conducted durability assessments through cyclic loading and unloading tests on polydomain LCE as shown in **Figure 4.2D**. The results indicate a decay in the magnitude of the plateau stress after 1000 cycles of less than 2%. The good durability of polydomain LCE is comparable to other elastic components in common elastic knitted fabrics, such as spandex and elastane[90], highlighting its potential for long-term use in compression therapy applications.

4.2.2.2 Performance of LCE-based static stocking

The chemical composition of LCE can be tailored to exhibit particular mechanical properties so that it can meet specific interfacial pressure requirements for compression stocking applications. The hoop stress *s* defines the interfacial pressure generated by the LCE stocking as:

$$P = \frac{2st}{D} \quad , \tag{1}$$

where *P* is the interfacial pressure applied by the stocking, *t* represents the thickness of the LCE layer, D is the diameter of the limb or stocking, and *s* is the hoop stress in the LCE, which is a function of D. By adjusting the chemical composition of LCE, it is possible to modulate *s* under various working temperatures, consequently, tailor *P* to meet the desired compression therapeutic objectives. The ability to fine-tune the thermomechanical properties of LCE underscores the adaptability of the material and potential utility in creating effective compression therapies, both static and dynamic.

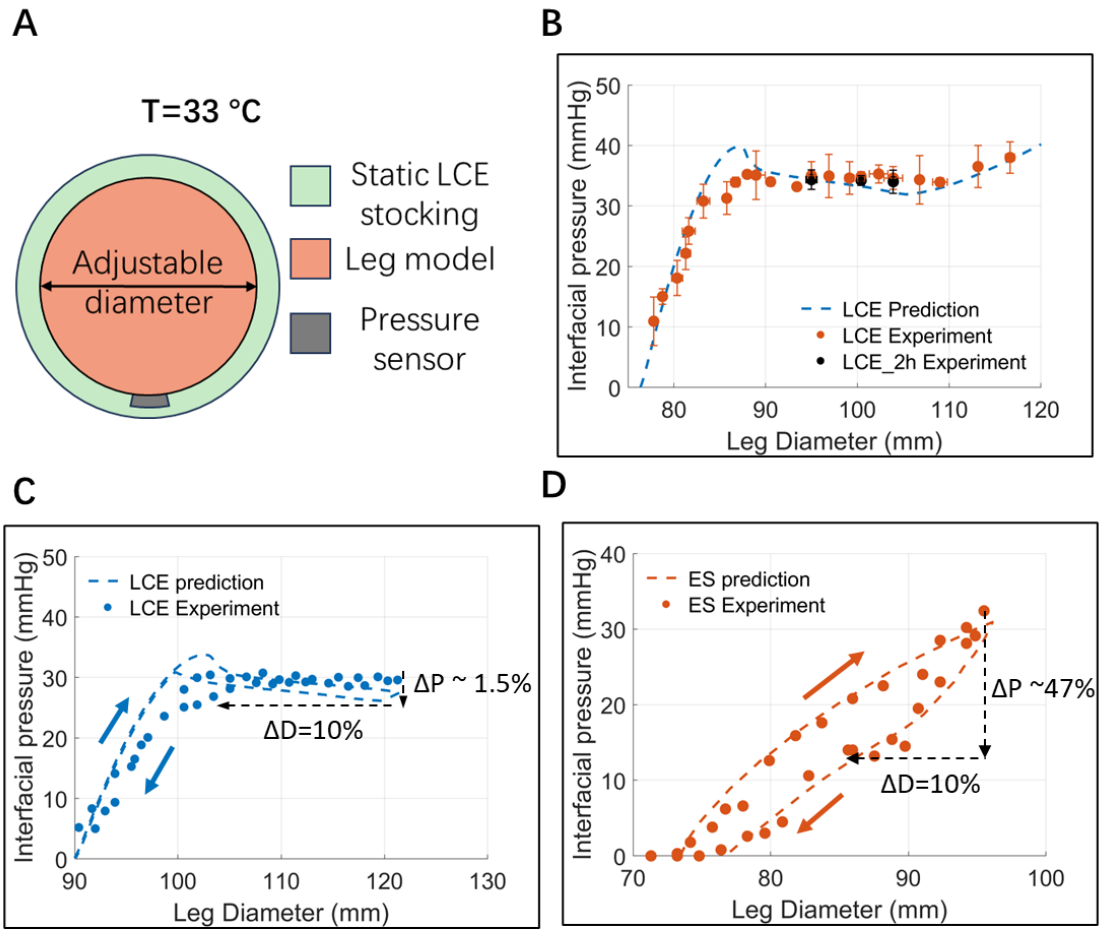

Figure 4.3 Performance of LCE-based static stocking.
A) Schematics of the measurement of interfacial pressure generated by the stocking. B) Prediction and measurement of interfacial pressure over a wide range of leg diameters of LCE-based static stocking. Prediction and measurement of interfacial pressure drop during the unloading of C) LCE-based static stocking and D) commercial elastic stocking.

With the understanding of the stress plateau and small hysteresis of polydomain LCE under human skin temperature, we characterized the interfacial pressure of the LCE-based static stocking as a function of stocking diameter. **Figure 4.3A** illustrates the experimental setup, where a leg model with adjustable diameters was utilized, by using rubber bands to secure removable rods and ensure a consistent circular profile. We took the interfacial pressure measurements using a 1mm-thick homemade pressure sensing pouch placed between the LCE

and the leg model, guaranteeing minimal distortion of the stocking's curvature. The experimental pictures of pressure measurement can be found in **Figure 4.4**.

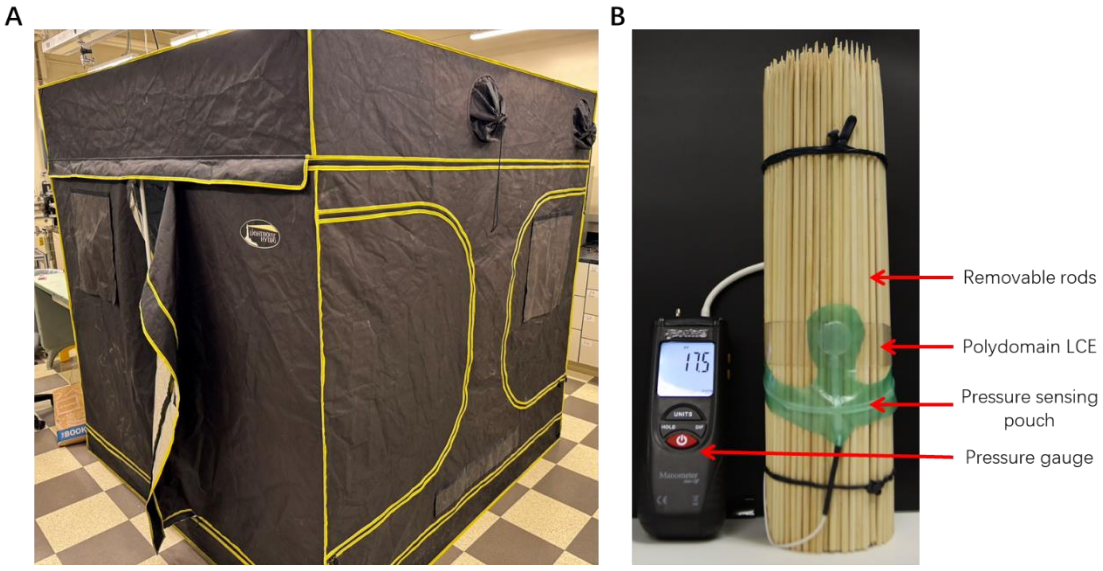

Figure 4.4 Experimental setup of the static LCE stocking characterization.
A) the home-made tent with controllable temperature to mimic the human skin temperature which is around 33 °C. B) A bundle of removable rods is used to represent different diameters of leg. A differential pressure gauge and a home-made air pouch were placed between static LCE stocking and the bundle to measure the interfacial pressure.

To understand the performance of the LCE-based static stocking, we predicted the interfacial pressure using Equation (1), where the stress s in LCE is a function of the circumference of a LCE stocking πD, where D is the leg diameter. Compression therapy requires 30 to 40 mmHg interfacial pressure to have a therapeutic effect[91]. Therefore, we chose 30 mmHg as the target interfacial pressure level for the study. By using the theoretical model in Eq. (1) and the LCE stress plateau magnitude s, we can calculate the thickness of the LCE stocking and fabricate accordingly. Additionally, we chose a representative leg diameter of 105 mm for the study since it is close to the average calf size for humans[92]. To generate consistent interfacial pressure levels within a wide range of leg diameter change, the strain value of the applied

polydomain LCE should fall within the corresponding strain range of the stress plateau, which is 20% to 50%, according to Figure 2B. Therefore, the initial diameter and thickness of the LCE-based static stocking can be determined and applied in both theoretical and experimental assessments.

Figure 4.3B illustrates the comparison between predicted and measured interfacial pressures generated by the LCE stocking on the leg model with varying diameters. We used a LCE stocking with a length of 234.2 mm and thickness of 0.36 mm in the prediction and experiment. Both the predicted and measured interfacial pressure are approximately a constant for the leg diameter ranging from 89 mm to 115 mm, a span sufficient to cover typical errors in the bandage application and the size range of commercial elastic stockings. We have also measured the consistency of the generated interfacial pressure over two hours for the leg model with diameters of 95 mm, 100.5 mm, and 104 mm. Our measurements show minimal pressure reduction, which implies the great stability of the LCE-based static stocking.

As shown in **Figure 4.3C**, to characterize the pressure drop during the leg deswelling, we predicted and measured the interfacial pressure generated by the LCE stocking with first increase and then decrease of the diameter of the leg model. The LCE-based static stocking exhibited only a 1.5% pressure drop with a 10% reduction in diameter. We further conducted similar experiments and predicted the interfacial pressure for the commercial elastic stocking (ES in Figure 3D). To predict the pressure as a function of leg diameter for ES, we conducted a tensile test on the ES calf area along the course direction. The material property of the elastic stocking was obtained from a tensile test of the calf area of a commercial elastic stocking in the course

direction, where the data can be found in **Figure 4.5**. As illustrated in **Figure 4.3D**, contrary to the LCE stocking, the commercial elastic stocking showed a 47% pressure drop under the same experimental conditions, which is significantly larger than that of the LCE-based static stocking. The error bars of **Figure 4.3C** and **Figure 4.3D** are detailed in **Figure 4.6**.

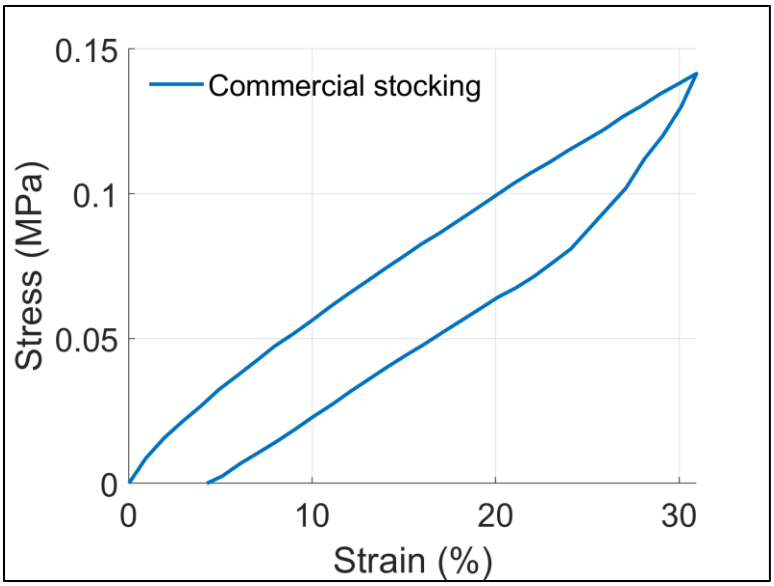

Figure 4.5 Tensile test of commercial elastic stocking on the calf area along the course direction

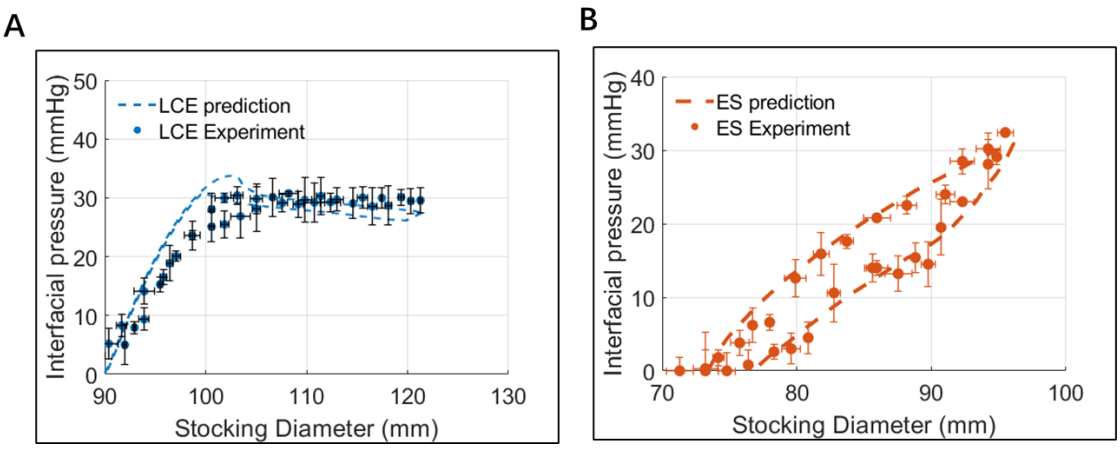

Figure 4.6 Figure 4.3C and Figure 4.3C with error bar.

To further understand the pressure drop during the unloading of the stocking, we generalized the model to different material properties, which can be found as following:
For a stocking material, we assume the nominal stress:

$$s(\lambda) \tag{2}$$

is a function of stretch λ. By rearranging the hoop stress:

$$P = \frac{2st}{d} \tag{3}$$

where P is the interfacial pressure, t is the stocking thickness, d is the leg diameter. We assume the stocking is under λ_1 right after the application with interfacial pressure of P_1. After a certain period, the leg deswell and diameter reduces, resulting in λ_2 for the stocking with interfacial pressure of P_2, so that

$$\lambda_2 = \alpha\lambda_1 \tag{4}$$

where α is the deswelling coefficient. Therefore, the pressure drop can be derived as:

$$\frac{P_1 - P_2}{P_1} = 1 - \frac{s(\alpha\lambda_1)}{\alpha s(\lambda_1)} \tag{5}$$

Therefore, LCE static stocking is a good candidate for maintaining the pressure level during leg deswelling compared to commercial elastic stockings.

4.2.3 LCE-based dynamic stocking

4.2.3.1 Actuation stress of a constrained monodomain LCE

We select monodomain LCE as the active material to construct the LCE-based dynamic stocking. In contrast to polydomain LCE, we did not include PEGDA in the polymer network so that we could fully take advantage of the phase transition of liquid crystal mesogen to generate a

large actuation force[47]. To understand the actuating behavior of the monodomain LCE, we conducted a series of thermomechanical characterizations.

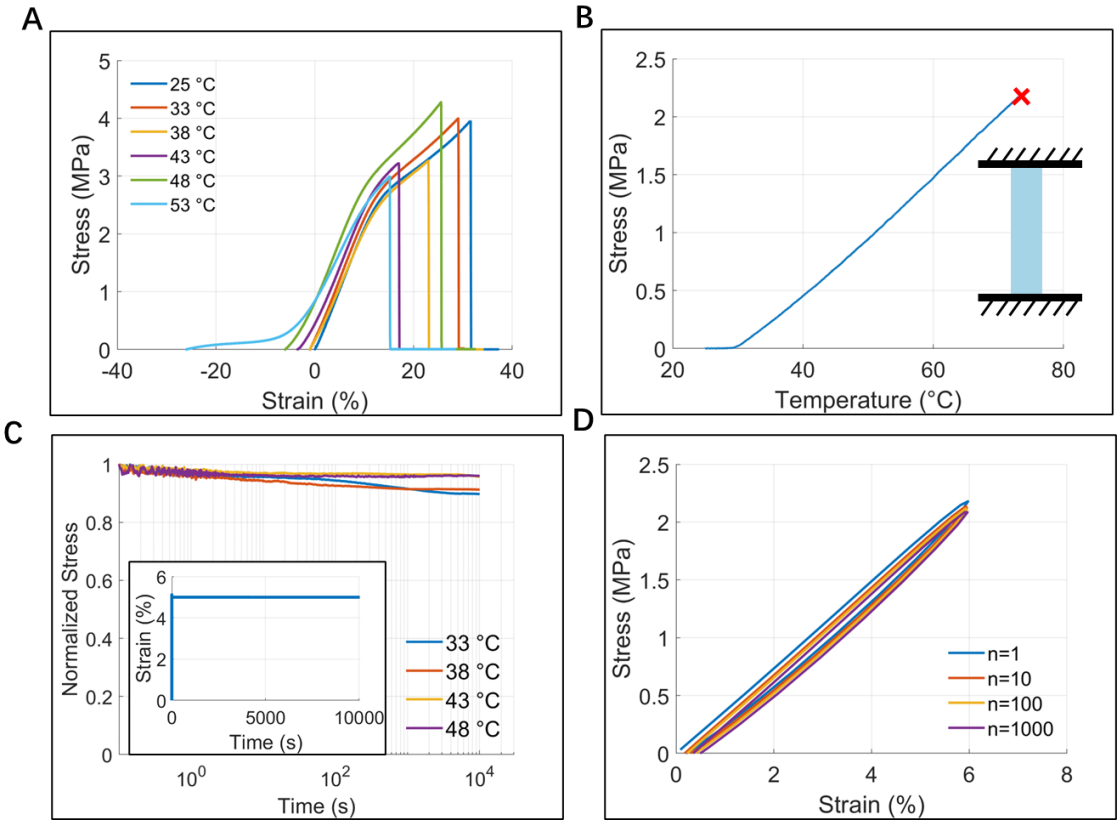

Figure 4.7 Thermomechanical characterization of monodomain LCE.
A) Stress-strain relationships of monodomain LCEs at various temperatures. The length of a freestanding LCE sample at 25 °C is used as the reference to calculate the strain. B) The thermal actuation stress of monodomain LCE increases with increasing temperature when the length is fixed at the initial state. C)Stress relaxation of monodomain LCE with 5% strain under various temperatures. D) Loading and unloading stress-strain curves of monodomain LCE after different numbers of loading cycles.

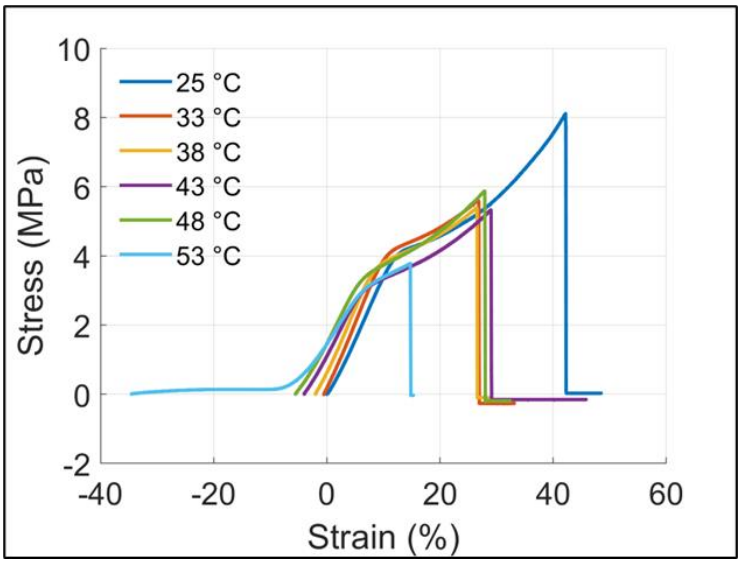

Figure 4.8 Additional characterization stress-strain relationships of monodomain LCE at various temperatures.

Figure 4.7A presents the thermomechanical properties of monodomain LCE, depicting its response to uniaxial tensile tests across various temperatures from 25 °C to 48 °C. To calculate the strain, we took the length of a free-standing LCE sample at 25 °C as the reference, so negative and positive strain represent material contraction and elongation, respectively. **Figure 4.8** shows the repeatability of the stress-strain curves of the monodomain LCEs. The material maintains similar modulus and strength across this temperature range. The stress-strain curves provide essential insights, allowing for the prediction of LCE behavior under different thermomechanical conditions, which is important for the design of LCE-based dynamic stockings.

Figure 4.7B illustrates the temperature-dependent actuation stress of a monodomain LCE with a fixed length. When the length of monodomain LCE is fixed, the actuation stress increases

monotonically with the temperature and eventually results in a material failure at around 1.7MPa. This behavior aligns with the testing results of the stress-strain curves in Figure 4A.

Figure 4.7C shows the stress relaxation of monodomain LCEs at different temperatures, indicating a stress decrease of less than 10% over 3 hours. This duration is longer than the typical length of a compression massage session, which usually lasts between 30 minutes to an hour[93].

Lastly, **Figure 4.7D** shows the durability of monodomain LCE through 1000 times of loading and unloading cycles, simulating the repeated application and removal of the stocking. The observed stress degradation is less than 10%, which highlights the robustness of the material, affirming its suitability for dynamic compression therapy applications.

4.2.3.2 Stretchable heater

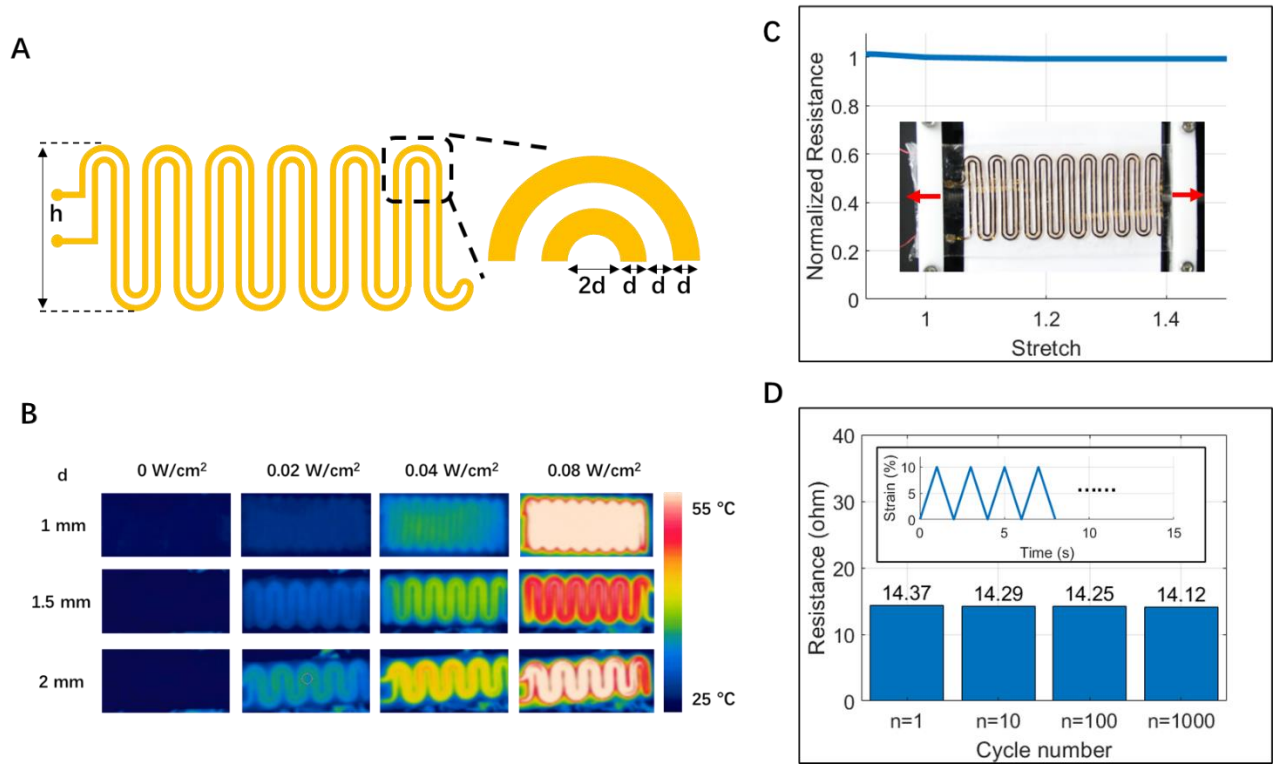

Figure 4.9 Thermomechanical characterizations of the flexible heating element. A) Design and dimensions of the heating pattern. The number of serpentines is for illustration purposes and less than the actual design. B) IR images of heating pattern with line widths d from 1mm to 2mm with different heating power. C) The heating pattern with d=1 mm maintains its electrical resistance with the stretch between 0.9 and 1.4. The inserted picture shows the testing setup with a house-made uniaxial stretcher to precisely control the stretch. D) The change of the electrical resistance of the heater as a function of the cycle number with the pattern width d= 1mm.

Another essential component of the LCE-based dynamic stocking is its heating element, which was fabricated from a thin copper film using a contour cutter to achieve the desired serpentine shape. We then sandwiched the heater between two monodomain LCE sheets, forming the actuating segment of the stocking. The serpentine design and dimensions of the heating pattern are shown in **Figure 4.9A**, where we kept the h=40 mm and varied the line width d in this study. The number of serpentines in **Figure 4.9A** is only for illustration purposes and it

may vary for different line width *d* and the overall dimension of the LCE-based dynamic stocking.

Figure 4.9B illustrates the temperature evaluation of the heating pattern with the copper line widths ranging from 1 to 2 mm, sandwiched between two monodomain LCE layers and fixed in length. An IR camera assessed the temperature distribution across these patterns at varying input powers. The design with a 1 mm line width was identified as the heater due to its uniform temperature distribution between 25 °C and 50 °C. Therefore, we chose the heating pattern with *d=1* mm for the study and the rest of the characterizations.

As depicted in **Figure 4.9C**, we assessed the mechanical durability of the heating element with d=1 mm under compression and tension. In the tests, we sandwiched the heating pattern between 2 stretched Very High Bonding (VHB) sheets and used a custom uniaxial stretcher, shown in the insert, for precise manipulation of the assembly. The heating element demonstrated consistent electrical resistance through 10% compression to 50% tension, affirming its robustness as a heating component.

Durability testing of the heating element, shown in **Figure 4.9D**, involved 1000 loading cycles to 10% strain. We chose the loading rate of 10%/s to mimic the practical LCE-based static stocking application. The electrical resistance of the heating element remained unchanged throughout the 1000 cycles, confirming its suitability for repeated use in the LCE-based dynamic stocking.

4.2.3.3 Performance of LCE dynamic stocking

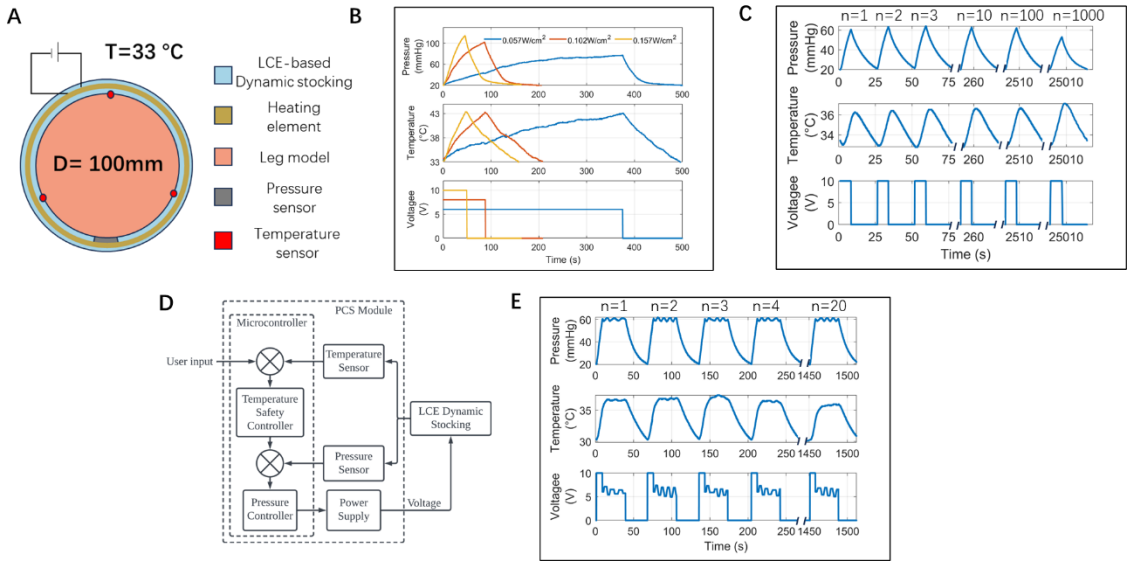

Figure 4.10 Characterization of the performance of LCE-based dynamic stocking. A) Schematics of the experimental setup. B) Characterization of interfacial pressure of LCE-based dynamic stocking at 43 °C, with various DC power inputs. C) Under cyclic voltage input, the dynamic stocking generates intermittent compression cycles, where the interfacial pressure and temperature are measured as a function of time. The pressure cycles remain consistent for up to 1000 cycles. D) Block diagram of closed loop pressure feedback control for controlling the interfacial pressure profile of the LCE-based dynamic stocking. E) With pressure feedback control, the interfacial pressure profile of the LCE-based dynamic stocking can be programmed. The temperature and holding voltage were measured as a function of time.

We constructed the LCE-based dynamic stocking with a DC power module (V_p) and a layered structure comprising two monodomain LCE sheets and one stretchable heater, with the LCE layers covalently bonded during the second step crosslink of monodomain LCE synthesis. As shown in **Figure 4.10A**, the experimental setup for the characterization of LCE-based dynamic stocking consists of a rigid leg model of 100 mm diameter and, a pressure sensor and three thermistors. We conducted the characterization by securing both ends of the LCE-based dynamic stocking to the leg model. To mimic the working environment of the dynamic compression treatment, prior to each characterization, we heated up the stocking to 33 °C, which is around human skin temperature. The detailed experimental setup can be found in **Figure 4.11**.

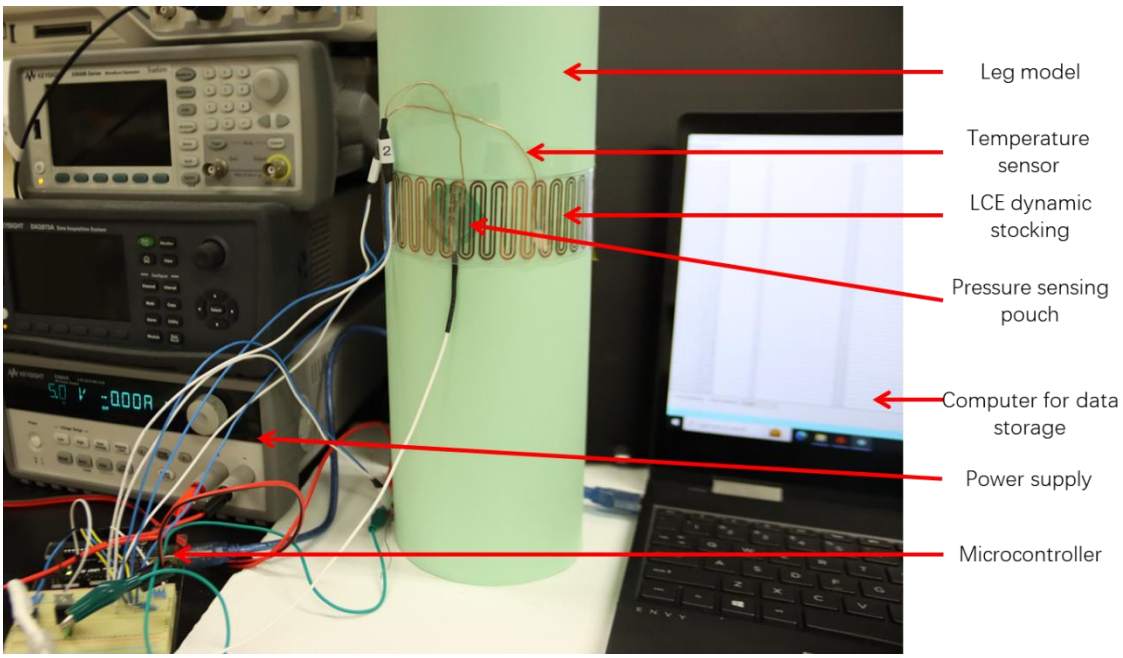

Figure 4.11 Experimental setup of the dynamic LCE stocking characterization

Figure 4.10B illustrates the capability of LCE-based dynamic stocking to modulate interfacial pressure through joule heating with varying power inputs. We set the temperature threshold to 43 °C, which is the approximately maximum skin temperature humans can endure for up to 8 hours without sustaining damage[94]. As the power input increases from 0.157 W/cm^2 to 0.057 W/cm^2, the time needed to heat the LCE-based dynamic stocking from 33 °C to 43 °C reduces from 375 s to 49 s, indicating that the compression cycle can be significantly shortened by increasing the power consumption. More importantly, the peak pressure increases from 76.9 mmHg to 113.7 mmHg, allowing the LCE-based dynamic stocking to achieve higher pressure within a shorter time, which is a desired property of the dynamic compression device. Therefore, 0.057 W/cm^2 was selected for the LCE-based dynamic stocking, balancing performance with energy conservation.

As illustrated in **Figure 4.10C**, we wrapped the LCE-based dynamic stocking around the leg model to exert an initial interfacial pressure of 20 mmHg. Periodic power input was applied to the LCE-based dynamic stocking, where V_p =10V, t_{on} =8s, and t_{off} = 20s. Cyclic pressure profiles and temperature profiles were measured. With this power input, the heating and cooling cycle takes about 30 seconds, similar to intermittent pneumatic devices[93]. Noticeably, the peak pressure of 60 mmHg is consistently maintained across hundreds of cycles, demonstrating the good performance of the stocking for elastomer-based smart compression therapy. The device temperature remained stable throughout these cycles, indicating safe operation within a comfortable range for human skin.

Figure 4.10E illustrates the controllability of the pressure profile generated by LCE-based dynamic stocking enabled by pressure feedback control (**Figure 4.10D**). **Figure 4.10E**, we demonstrated that the dynamic stocking can maintain a constant pressure level at 60 mmHg for 30 seconds for each compression cycle. We used the interfacial pressure as a feedback signal to control the voltage input, therefore changing the applied temperature to regulate the pressure level close to the prescribed value. This capability suggests that more complicated pressure profiles could be designed by utilizing the measured thermomechanical properties of monodomain LCE and the theoretical model in Eq. (1), enhancing the system's adaptability for various therapeutic needs.

4.2.3.4 Demonstration of untethered LCE compression device on human leg

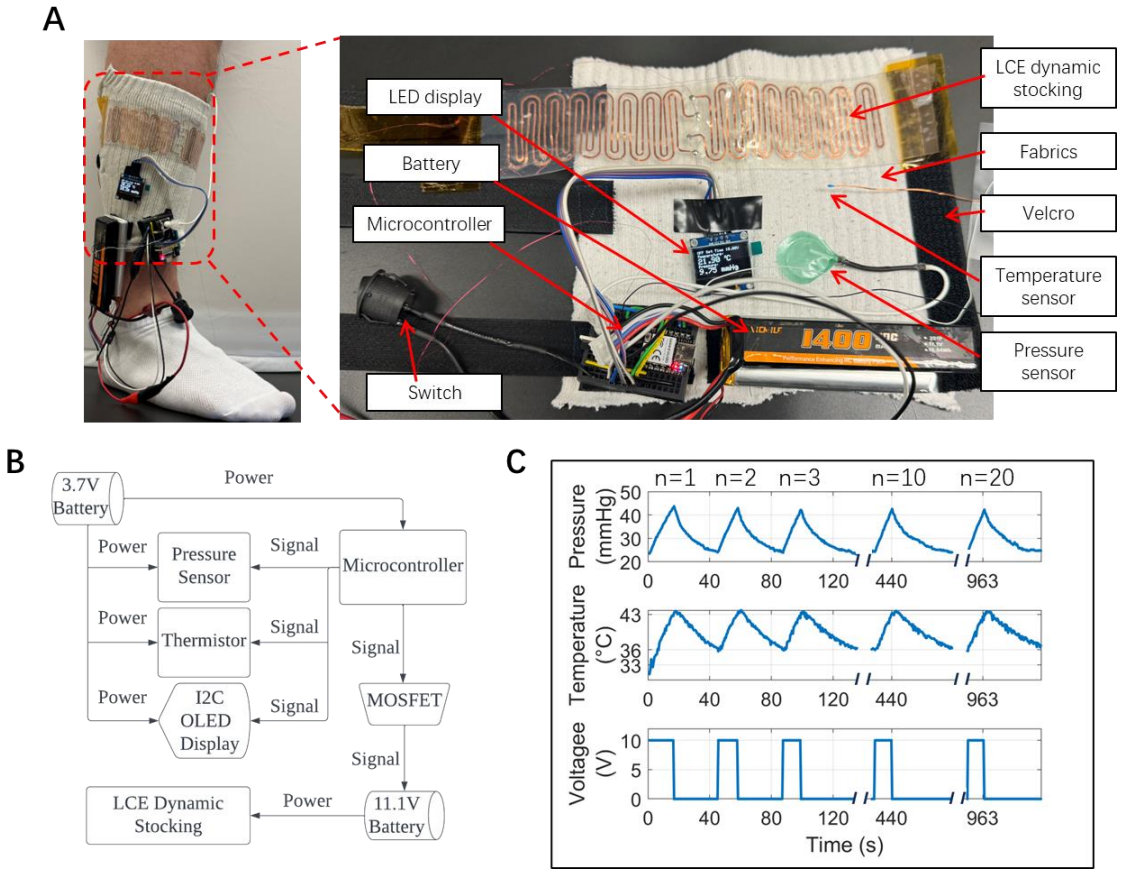

Figure 4.12 Application of untethered LCE compression device on a human leg.
A) Design of the untethered LCE compression device and its application on the human leg. The LCE dynamic stocking and the PCS module are attached to a piece of fabric with Velcro straps. B) The working principle and electronic design of the PCS module. C) The untethered LCE dynamic stocking performance on the human leg for 20 cycles, exerting interfacial pressure from 23 to 43 mmHg. The working temperature was kept under 43 °C.

With the understanding of LCE-based dynamic stocking from the characterization, we developed an untethered and wearable LCE compression device that generates intermittent pressure cycles. As illustrated in **Figure 4.12A**, the compression device is applied to a human calf. The LCE-based dynamic stocking, PCE module, and Velcro straps are secured to a fabric substrate, allowing easy application of the integrated device. This design not only allows patients to easily apply and adjust the device to fit various leg sizes by themselves but also incorporates a

fabric layer as a thermal insulating layer, preventing the skin against potential heat damage. In contrast to conventional pneumatic compression devices that are typically stationary and cumbersome, the wearable LCE compression device only weighs 186 grams including the batteries to support mobility, thereby not interfering with the daily activities of the patients.

Figure 4.12B details the working principle of the PCS module used for the dynamic compression stocking. A microcontroller is programmed to manage the power from an 11.1 V lithium polymer battery, activating the stocking on demand. The pressure sensor monitors real-time interfacial pressure between the fabric and the leg, while the temperature sensor monitors the interface temperature between the LCE-based dynamic stocking and the fabric. The LED display provides real-time data on pressure, temperature, and voltage, enhancing user interaction.

Finally, we demonstrated the performance of wearable LCE-based dynamic compression device on a human leg. As shown in **Figure 4.12C**, by controlling the temperature between 36 to 43 °C, the compression device can exert an interfacial pressure from 23 to 43 mmHg on the leg. The microcontroller receives the temperature feedback signal from the temperature sensor and controls the applied voltage to the compression device. The peak interfacial pressure remained consistent for at least 20 cycles, indicating a consistent performance of the device. Each intermittent compression cycle was less than 50 seconds, which is comparable to pneumatic-based compression devices that is typically around 1 minute[95]. This timescale is much shorter than other thermally responsive compression devices, such as shape memory polymer-based compression devices that take over half an hour for one cycle. With a 1400 mAh battery, the device can function up to 296 cycles that equivalent to around 4-hour of compression session.

The electrical resistance *R* of the heating element is 11.5 ohms. The battery used to power the heating elements has a capacity of *It=1400 mAh* at *U=11.1 V*. By using the Ohm's law:

$$I = \frac{U}{R}. \quad (5)$$

we calculated that the battery can continuously power the heating element for around *t=1.45h*. For each compression cycle of the untethered and wearable LCE-base compression device, the average heating time and cooling time are $t_{heating}$*=17s* and $t_{cooling}$*=28s*, respectively. Therefore, the total running time t_{total}=3.84 for the compression device can be calculated as follows:

$$t_{total} = t \times \frac{t_{heating}+t_{cooling}}{t_{heating}}. \quad (5)$$

In the experiments shown in **Figure 4.10** and **Figure 4.12**, we used the same LCE-based dynamic stocking in the rigid leg model and real human leg. We have noticed that although the temperature increase in the stocking is higher for the human leg demonstration, a smaller interfacial pressure was generated. This is due to the higher compliance of the human leg. As the temperature increases, the diameter of the human leg decreases in response to the LCE actuation, leading to the shortening of the LCE. As a result, the actuation stress of LCE is smaller in human leg experiments. Such reduction of the interfacial stress can be easily compensated by slightly increasing LCE thickness.

4.3 Conclusion

Though various solutions have been proposed for compression therapy in the past, intrinsic limitations still exist. Both static and dynamic compression therapies often fail to

maintain optimal pressure levels over the required duration, affecting therapeutic efficacy. In this study, we successfully addressed the challenges of both static compression and dynamic compression therapy by using LCE as the primary material due to its unique thermomechanical properties.

For static compression stocking, we developed a polydomain LCE with incorporated PEGDA as a flexible backbone to the polymer network. The resulted polydomain LCE exhibits stress plateau over a large range of strain and negligible mechanical hysteresis, which can be harnessed to accommodate error of stocking application and various limb sizes and also reduce interfacial pressure drop due to the deswelling of a leg. Moreover, the polydomain LCE shows negligible stress relaxation and good repeatability for over 1000 cycles of loading to 30% strain, which offers consistent and prolonged interfacial pressure from the LCE-based static stocking.

For dynamic compression stocking, we introduced monodomain LCE for the actuation, harnessing its reversible thermal actuation properties. The nematic-isotropic phase transition of LCE enables the LCE to exert enough pressure around the leg when it is heated slightly above human skin temperature. The embedded heater was carefully designed and characterized to ensure high temperature homogeneity and durability.

Our experiments have shown that LCE-based dynamic stocking can generate interfacial pressure from 20 to 60 mmHg with a temperature increase from 33 to 38 °C for over 1000 cycles. We further demonstrated that a controlled pressure profile can be achieved by using pressure feedback control. The untethered and wearable LCE-based compression device

composed of a PCS module, fabric and Velcro straps, successfully applied up to 43 mmHg of pressure to the human leg over 20 cycles. With a single battery charge, the device could support continuous intermittent pressure cycles for approximately four hours.

4.4 Experimental section

4.4.1 Materials:

4-(6-(acryloyloxy)hexyloxy)phenyl-4-(6- (acryloyloxy)hexyloxy)benzoate (C6BAPE, Chemfish, 97%), 2,4,6-Triallyloxy-1,3,5-triazine (TAC, Sigma-Aldrich, 97%), Poly(ethylene glycol) diacrylate (PEGDA, Mn 500, Sigma-Aldrich, 95%), 2,2'-(ethylenedioxy) diethanethiol (EDDET, Sigma-Aldrich, 95%), pentaerythritol tetrakis (3-mercaptopropionate) (PETMP, Sigma-Aldrich, 95%), dipropylamine (DPA, Sigma-Aldrich, 98%), (2-hydroxyethoxy)-2-methylpropiophenone (HHMP; Sigma-Aldrich; 98%), and all the solvents were used as received without further purification. All the chemical structures can be found in Figure S6. The commercial stocking was purchased from Amazon Basic Care in medium size.

4.4.2 Fabrication of LCE-based static stocking:

The polydomain LCE film was prepared via base-catalyzed thiol-acrylate Michael addition reaction followed by a second-stage photopolymerization. Firstly, C6BAPE (10.0000 g), PEGDA (0.7396), and TAC (0.3673g) were dissolved in toluene (3.1000 g) at 80 °C for 30 minutes. Secondly, add a mixture of chain extender EDDET (1.9018 g) and crosslinker PETMP (1.5293 g) to the solution. For the above chemicals, we maintained a stoichiometry of

$$2n_{C6BAPE}: 2n_{PEGDA}: 3n_{TAC}: 4n_{PETMP}: 2n_{EDDET}=0.84:0.06:0.1:0.5:0.5 \quad . \qquad (6)$$

After the mixture above is fully dissolved, the photo-initiator HHMP (0.0772 g) and catalyst DPA solution (1 wt%, 3.24 g) were sequentially added to the solution. Thirdly, the solution was vigorously mixed and vacuumed for 5 minutes to remove the air trapped in the solution. Then, the solution was poured into a compression-assisted mold for 24 hours in a dark environment and dried at 80 °C for another 24 hours. Finally, the loosely crosslinked LCE was placed on a 0 °C cold plate, and the LCE was left under UV (365nm) for 60 minutes to obtain polydomain LCE.

The LCE-based static stocking was fabricated by bonding polydomain LCE-based and Velcro strips (hook and loop) with VHB tape, as shown in Figure 1A. To achieve a 30 mmHg pressure with a 100 mm leg diameter, the dimensions of polydomain LCE need to be carefully designed. When the LCE-based static stocking generates 30 mmHg interfacial pressure, the polydomain should be at the stress plateau, so that it can stable pressure. When the LCE-based static stocking is worn on a leg with a 100 mm diameter, the polydomain LCE should be stretched to the middle of the plateau so that it can tolerate a wide range of displacement. Therefore, the initial length and thickness of the LCE-based static stocking were chosen as 234.2 mm and 0.36mm, respectively.

4.4.3 Fabrication of LCE-based dynamic stocking:

Firstly, we adopted a similar method of polydomain LCE synthesis to the monodomain LCE film, where the chemical ratio was kept at:

$$2n_{C6BAPE}: 3n_{TAC}: 4n_{PETMP}: 2n_{EDDET}=0.9:0.1:0.5:0.5 \quad (7)$$

After the loosely crosslinked LCE was obtained, the LCE was stretched and fixed at $\lambda=1.8$ on a copper plate to avoid LCE temperature increase. To fabricate the heating pattern, we used a contour cutter (Maker 3, Cricut, USA) equipped with a fine point blade (30-degree blade angel) to cut a copper–polyimide bilayer sheet (Bate Electronics, China) on an adhesive mat (Cricut, USA). The copper–polyimide bilayer sheet consists of a copper layer of 2 microns and a polyimide layer of 25 microns. Then, we soldered two 30 cm-long copper wires (36AWG, BNTECHGO, China) to the heating element and transferred the heating element using water-soluble tape (AQUASOL, USA) to the pre-stretched LCE sheet. After gently washing off the water-soluble tape and drying the water at room temperature, another layer of pre-stretched LCE sheet was carefully put on top of the first layer. Finally, the LCE-heater-LCE sandwich structure was left under UV (365nm) for 60 minutes to obtain the LCE-heater-LCE sandwich structure as the LCE-based dynamic stocking.

We used a sewing machine (3160QOV, Janome, Japan) to stitch the Velcro (hook and loop) straps onto a piece of cotton fabric as the substrate material for the wearable LCE-based dynamic compression device. As shown in Figure 7A, the LCE-based dynamic stocking, OLED display, and PCS module were attached to the cotton fabrics in different positions with Velcro on the back.

4.4.4 Design of PCS (Power, Control, Sensor) module:

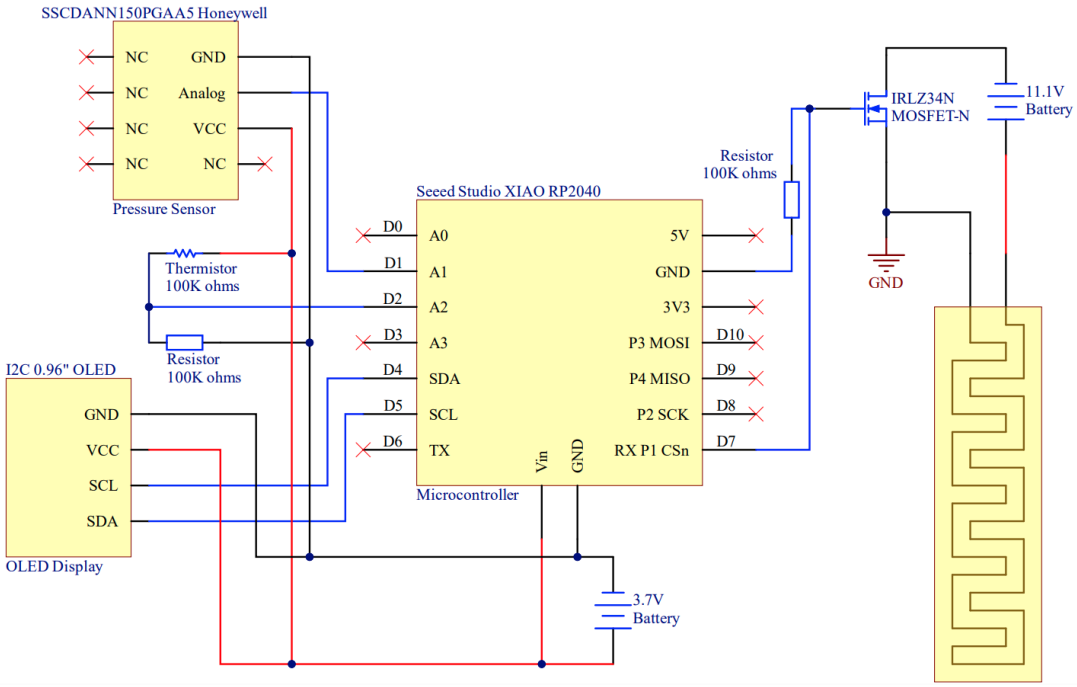

Figure 4.13 The electronics design of PCS module.

Figure 4.13 shows the circuit design of the Power, Control, Sensing (PCS) module for the LCE-based dynamic stocking. The Seeed Xiao RP2040 microcontroller is responsible for continuously monitoring and processing data from the connected sensors. The microcontroller dynamically adjusts the control of the heating element and displays the temperature and pressure readings on the display. The temperature of the heating element is measured using a negative temperature coefficient (NTC) thermistor (100k ohm), whose resistance decreases with increasing temperature. The pressure between the stocking and the skin is measured using a

piezoresistive silicon pressure sensor(SSCDANN150PGAA5, Honeywell), which outputs an analog voltage proportional to the pressure inside a sealed pouch. The heating element of the stocking is controlled via an N-channel metal-oxide-semiconductor field-effect transistor (MOSFET) (IRLZ34N), which acts as a switch to manage power delivery from the 11.1V Lithium Polymer battery based on commands from the microcontroller. A 0.96-inch I2C organic light-emitting diode (OLED) display is used for presenting real-time temperature, pressure, and voltage readings. A 3.7V Lithium Polymer battery powers the microcontroller, sensors, and display, while a separate 11.1V Lithium Polymer battery supplies power to the heating element. Each power system is equipped with its own physical switch for user operation.

The connections of the circuit are detailed below:

Thermistor Connection: The thermistor is connected in a voltage divider configuration with a 100k ohms resistor. The junction between the thermistor and the fixed resistor is connected to an analog input pin (A2) on the Seeed Xiao RP2040. The thermistor is powered by the 3.7V one-cell Lithium Polymer battery.

Pressure Sensor Connection: The pressure sensor's analog output is connected to an analog input pin (A1) on the Seeed Xiao RP2040. The pressure sensor is powered by the 3.7V one-cell Lithium Polymer battery.

MOSFET Control: The gate of the N-channel MOSFET is connected to a digital output pin (D7) on the Seeed Xiao RP2040. The source is connected to the ground, and the drain is connected to the negative terminal of the 11.1V three-cell Lithium Polymer battery. The positive terminal of the 11.1V three-cell Lithium Polymer battery is connected to the heating wire.

I2C OLED Display Connection: The SDA (data) and SCL (clock) pins of the OLED display are connected to the corresponding I2C pins (SDA and SCL) on the Seeed Xiao RP2040. The I2C OLED display is powered by the 3.7V one-cell Lithium Polymer battery.

Heating Element Connection: The heating element connection in this system is designed to interface with an 11.1V three-cell Lithium Polymer battery. The MOSFET is used as a switching device to control the power flow to the heating element. Additionally, a power switch is incorporated to offer user control, allowing for the safe activation and deactivation of the heating element.

To ensure accurate and reliable measurements in experimental tests, it is essential to perform a linear calibration of both the pressure and temperature sensors using a pressure gauge (LEX1, Keller, Switzerland) and a k-type thermocouple thermometer prior to each test. For the pressure sensor: Apply a series of known pressure values between 0-80 mmHg to the sensor by connecting it to a pressure meter using a push-in T-connector. These values should cover the entire range of the sensor and be evenly spaced. For the temperature sensor: Expose the sensor to a series of known temperature points between 0-100°C using a thermocouple thermometer. These points should be evenly distributed across the operating range. To perform the calibration: Plot the recorded sensor outputs versus the known values of pressure or temperature. Perform a linear regression analysis to determine the best-fit line through the data points. This line represents the calibration curve for the sensor. From the linear regression, determine the slope and intercept of the calibration curve. These constants will be used to convert the sensor's raw data into meaningful units during the tests. To verify the accuracy of the calibration, apply a few

known values again and compare the sensor readings with the expected results based on the calibration curve. Adjustments may be required if there are significant discrepancies.

The compression device is equipped with critical safety features, including a temperature safety setting of 46 °C to prevent overheating and a pressure safety setting of 80 mmHg to avoid excessive compression, ensuring both the efficacy and safety of the device during operation. We used a suitable MOSFET that can handle the voltage and current requirements of the external load.

4.4.5 Characterization:

The uniaxial tensile and cyclic loading tests were performed by a tensile tester (5965, Instron) with a 10N static load cell. The 1%/s strain rate was used for this study to mimic the real-life application timescale.

The uniaxial tensile tests above room temperature and stress relaxation tests were performed using a dynamic mechanical analyzer (RSA-G2, TA Instrument) at specified temperatures. A 1%/s strain rate was maintained for the tensile tests.

The IR images and videos were captured by the IR camera (C3-X, FLIR), where the temperature reading was calibrated to match the actual temperature measured by a separate thermocouple.

The resistance measurement was done by applying a 5V DC voltage to the heating pattern and recording the current value. The resistance was then calculated accordingly using Ohm's law:

$$R = \frac{U}{I} \quad , \tag{8}$$

where U is the applied voltage and I is the current.

4.5 Reference

(1) Wang, L.; Iida, F. Deformation in Soft-Matter Robotics: A Categorization and Quantitative Characterization. *IEEE Robot. Automat. Mag.* **2015**, *22* (3), 125–139. https://doi.org/10.1109/MRA.2015.2448277.

(2) Laschi, C.; Mazzolai, B.; Cianchetti, M. Soft Robotics: Technologies and Systems Pushing the Boundaries of Robot Abilities. *Sci. Robot.* **2016**, *1* (1), eaah3690. https://doi.org/10.1126/scirobotics.aah3690.

(3) Hao, Y.; Zhang, S.; Fang, B.; Sun, F.; Liu, H.; Li, H. A Review of Smart Materials for the Boost of Soft Actuators, Soft Sensors, and Robotics Applications. *Chin. J. Mech. Eng.* **2022**, *35* (1), 37. https://doi.org/10.1186/s10033-022-00707-2.

(4) Chen, Z.-J.; Gao, F.; Pan, Y. Novel Door-Opening Method for Six-Legged Robots Based on Only Force Sensing. *Chin. J. Mech. Eng.* **2017**, *30* (5), 1227–1238. https://doi.org/10.1007/s10033-017-0172-7.

(5) Carpentier, J.; Mansard, N. Multicontact Locomotion of Legged Robots. *IEEE Trans. Robot.* **2018**, *34* (6), 1441–1460. https://doi.org/10.1109/TRO.2018.2862902.

(6) Shian, S.; Bertoldi, K.; Clarke, D. R. Dielectric Elastomer Based "Grippers" for Soft Robotics. *Advanced Materials* **2015**, *27* (43), 6814–6819. https://doi.org/10.1002/adma.201503078.

(7) Mazzolai, B.; Margheri, L.; Cianchetti, M.; Dario, P.; Laschi, C. Soft-Robotic Arm Inspired by the Octopus: II. From Artificial Requirements to Innovative Technological Solutions. *Bioinspir. Biomim.* **2012**, *7* (2), 025005. https://doi.org/10.1088/1748-3182/7/2/025005.

(8) Shen, Q.; Wang, T.; Liang, J.; Wen, L. Hydrodynamic Performance of a Biomimetic Robotic Swimmer Actuated by Ionic Polymer–Metal Composite. *Smart Mater. Struct.* **2013**, *22* (7), 075035. https://doi.org/10.1088/0964-1726/22/7/075035.

(9) Keplinger, C.; Sun, J.-Y.; Foo, C. C.; Rothemund, P.; Whitesides, G. M.; Suo, Z. Stretchable, Transparent, Ionic Conductors. *Science* **2013**, *341* (6149), 984–987. https://doi.org/10.1126/science.1240228.

(10) Lee, E.; Kim, D.; Kim, H.; Yoon, J. Photothermally Driven Fast Responding Photo-Actuators Fabricated with Comb-Type Hydrogels and Magnetite Nanoparticles. *Sci Rep* **2015**, *5* (1), 15124. https://doi.org/10.1038/srep15124.

(11) Bassik, N.; Abebe, B. T.; Laflin, K. E.; Gracias, D. H. Photolithographically Patterned Smart Hydrogel Based Bilayer Actuators. *Polymer* **2010**, *51* (26), 6093–6098. https://doi.org/10.1016/j.polymer.2010.10.035.
(12) Shin, B.; Ha, J.; Lee, M.; Park, K.; Park, G. H.; Choi, T. H.; Cho, K.-J.; Kim, H.-Y. Hygrobot: A Self-Locomotive Ratcheted Actuator Powered by Environmental Humidity. *Sci. Robot.* **2018**, *3* (14), eaar2629. https://doi.org/10.1126/scirobotics.aar2629.
(13) Poojary, U. R.; Gangadharan, K. V. Material Modeling of Frequency, Magnetic Field and Strain Dependent Response of Magnetorheological Elastomer. *J Mater Sci* **2021**, *56* (28), 15752–15766. https://doi.org/10.1007/s10853-021-06307-0.
(14) Dong, G.; He, Q.; Cai, S. Magnetic Vitrimer-Based Soft Robotics. *Soft Matter* **2022**, *18* (39), 7604–7611. https://doi.org/10.1039/D2SM00893A.
(15) De Gennes, P.; Hébert, M.; Kant, R. Artificial Muscles Based on Nematic Gels. *Macromolecular Symposia* **1997**, *113* (1), 39–49. https://doi.org/10.1002/masy.19971130107.
(16) Brazel, C. S. Magnetothermally-Responsive Nanomaterials: Combining Magnetic Nanostructures and Thermally-Sensitive Polymers for Triggered Drug Release. *Pharm Res* **2009**, *26* (3), 644–656. https://doi.org/10.1007/s11095-008-9773-2.
(17) Thévenot, J.; Oliveira, H.; Sandre, O.; Lecommandoux, S. Magnetic Responsive Polymer Composite Materials. *Chem. Soc. Rev.* **2013**, *42* (17), 7099. https://doi.org/10.1039/c3cs60058k.
(18) Kuang, X.; Wu, S.; Ze, Q.; Yue, L.; Jin, Y.; Montgomery, S. M.; Yang, F.; Qi, H. J.; Zhao, R. Magnetic Dynamic Polymers for Modular Assembling and Reconfigurable Morphing Architectures. *Advanced Materials* **2021**, *33* (30), 2102113. https://doi.org/10.1002/adma.202102113.
(19) Kim, Y.; Yuk, H.; Zhao, R.; Chester, S. A.; Zhao, X. Printing Ferromagnetic Domains for Untethered Fast-Transforming Soft Materials. *Nature* **2018**, *558* (7709), 274–279. https://doi.org/10.1038/s41586-018-0185-0.
(20) Cheng, Y.; Chan, K. H.; Wang, X.-Q.; Ding, T.; Li, T.; Zhang, C.; Lu, W.; Zhou, Y.; Ho, G. W. A Fast Autonomous Healing Magnetic Elastomer for Instantly Recoverable, Modularly Programmable, and Thermorecyclable Soft Robots. *Advanced Functional Materials* **2021**, *31* (32), 2101825. https://doi.org/10.1002/adfm.202101825.
(21) Matxain, J. M.; Asua, J. M.; Ruipérez, F. Design of New Disulfide-Based Organic Compounds for the Improvement of Self-Healing Materials. *Phys. Chem. Chem. Phys.* **2016**, *18* (3), 1758–1770. https://doi.org/10.1039/C5CP06660C.
(22) Maeda, T.; Otsuka, H.; Takahara, A. Dynamic Covalent Polymers: Reorganizable Polymers with Dynamic Covalent Bonds. *Progress in Polymer Science* **2009**, *34* (7), 581–604. https://doi.org/10.1016/j.progpolymsci.2009.03.001.
(23) Ruff, Y.; Lehn, J. Glycodynamers: Dynamic Analogs of Arabinofuranoside Oligosaccharides. *Biopolymers* **2008**, *89* (5), 486–496. https://doi.org/10.1002/bip.20885.
(24) Otsuka, H.; Muta, T.; Sakada, M.; Maeda, T.; Takahara, A. Scrambling Reaction between Polymers Prepared by Step-Growth and Chain-Growth Polymerizations: Macromolecular Cross-Metathesis between 1,4-Polybutadiene and Olefin-Containing Polyester. *Chem. Commun.* **2009**, No. 9, 1073. https://doi.org/10.1039/b818014h.
(25) Guimard, N. K.; Oehlenschlaeger, K. K.; Zhou, J.; Hilf, S.; Schmidt, F. G.; Barner-Kowollik, C. Current Trends in the Field of Self-Healing Materials. *Macro Chemistry & Physics* **2012**, *213* (2), 131–143. https://doi.org/10.1002/macp.201100442.

(26) Bergman, S. D.; Wudl, F. Mendable Polymers. *J. Mater. Chem.* **2008**, *18* (1), 41–62. https://doi.org/10.1039/B713953P.
(27) Cordier, P.; Tournilhac, F.; Soulié-Ziakovic, C.; Leibler, L. Self-Healing and Thermoreversible Rubber from Supramolecular Assembly. *Nature* **2008**, *451* (7181), 977–980. https://doi.org/10.1038/nature06669.
(28) Burattini, S.; Colquhoun, H. M.; Fox, J. D.; Friedmann, D.; Greenland, B. W.; Harris, P. J. F.; Hayes, W.; Mackay, M. E.; Rowan, S. J. A Self-Repairing, Supramolecular Polymer System: Healability as a Consequence of Donor–Acceptor π–π Stacking Interactions. *Chem. Commun.* **2009**, No. 44, 6717. https://doi.org/10.1039/b910648k.
(29) Burnworth, M.; Tang, L.; Kumpfer, J. R.; Duncan, A. J.; Beyer, F. L.; Fiore, G. L.; Rowan, S. J.; Weder, C. Optically Healable Supramolecular Polymers. *Nature* **2011**, *472* (7343), 334–337. https://doi.org/10.1038/nature09963.
(30) Ritz, D.; Beckwith, J. Roles of Thiol-Redox Pathways in Bacteria. *Annu. Rev. Microbiol.* **2001**, *55* (1), 21–48. https://doi.org/10.1146/annurev.micro.55.1.21.
(31) Wedemeyer, W. J.; Welker, E.; Narayan, M.; Scheraga, H. A. Disulfide Bonds and Protein Folding. *Biochemistry* **2000**, *39* (15), 4207–4216. https://doi.org/10.1021/bi992922o.
(32) Spillmann, C. M.; Naciri, J.; Martin, B. D.; Farahat, W.; Herr, H.; Ratna, B. R. Stacking Nematic Elastomers for Artificial Muscle Applications. *Sensors and Actuators A: Physical* **2007**, *133* (2), 500–505. https://doi.org/10.1016/j.sna.2006.04.045.
(33) Zeng, H.; Wani, O. M.; Wasylczyk, P.; Kaczmarek, R.; Priimagi, A. Self-Regulating Iris Based on Light-Actuated Liquid Crystal Elastomer. *Advanced Materials* **2017**, *29* (30), 1701814. https://doi.org/10.1002/adma.201701814.
(34) Rogóż, M.; Zeng, H.; Xuan, C.; Wiersma, D. S.; Wasylczyk, P. Light-Driven Soft Robot Mimics Caterpillar Locomotion in Natural Scale. *Advanced Optical Materials* **2016**, *4* (11), 1689–1694. https://doi.org/10.1002/adom.201600503.
(35) Ahn, C.; Liang, X.; Cai, S. Inhomogeneous Stretch Induced Patterning of Molecular Orientation in Liquid Crystal Elastomers. *Extreme Mechanics Letters* **2015**, *5*, 30–36. https://doi.org/10.1016/j.eml.2015.09.007.
(36) Bisoyi, H. K.; Li, Q. Light-Driven Liquid Crystalline Materials: From Photo-Induced Phase Transitions and Property Modulations to Applications. *Chem. Rev.* **2016**, *116* (24), 15089–15166. https://doi.org/10.1021/acs.chemrev.6b00415.
(37) Boothby, J. M.; Kim, H.; Ware, T. H. Shape Changes in Chemoresponsive Liquid Crystal Elastomers. *Sensors and Actuators B: Chemical* **2017**, *240*, 511–518. https://doi.org/10.1016/j.snb.2016.09.004.
(38) Yakacki, C. M.; Saed, M.; Nair, D. P.; Gong, T.; Reed, S. M.; Bowman, C. N. Tailorable and Programmable Liquid-Crystalline Elastomers Using a Two-Stage Thiol–Acrylate Reaction. *RSC Adv.* **2015**, *5* (25), 18997–19001. https://doi.org/10.1039/C5RA01039J.
(39) Kotikian, A.; Truby, R. L.; Boley, J. W.; White, T. J.; Lewis, J. A. 3D Printing of Liquid Crystal Elastomeric Actuators with Spatially Programed Nematic Order. *Advanced Materials* **2018**, *30* (10), 1706164. https://doi.org/10.1002/adma.201706164.
(40) Wang, Z.; Wang, Z.; Zheng, Y.; He, Q.; Wang, Y.; Cai, S. Three-Dimensional Printing of Functionally Graded Liquid Crystal Elastomer. *Sci. Adv.* **2020**, *6* (39), eabc0034. https://doi.org/10.1126/sciadv.abc0034.
(41) He, Q.; Wang, Z.; Wang, Y.; Song, Z.; Cai, S. Recyclable and Self-Repairable Fluid-Driven Liquid Crystal Elastomer Actuator. *ACS Appl. Mater. Interfaces* **2020**, *12* (31), 35464–35474. https://doi.org/10.1021/acsami.0c10021.

(42) He, Q.; Wang, Z.; Song, Z.; Cai, S. Bioinspired Design of Vascular Artificial Muscle. *Adv Materials Technologies* **2019**, *4* (1), 1800244. https://doi.org/10.1002/admt.201800244.
(43) He, Q.; Wang, Z.; Wang, Y.; Minori, A.; Tolley, M. T.; Cai, S. Electrically Controlled Liquid Crystal Elastomer–Based Soft Tubular Actuator with Multimodal Actuation. *Sci. Adv.* **2019**, *5* (10), eaax5746. https://doi.org/10.1126/sciadv.aax5746.
(44) Wang, C.; Sim, K.; Chen, J.; Kim, H.; Rao, Z.; Li, Y.; Chen, W.; Song, J.; Verduzco, R.; Yu, C. Soft Ultrathin Electronics Innervated Adaptive Fully Soft Robots. *Advanced Materials* **2018**, *30* (13), 1706695. https://doi.org/10.1002/adma.201706695.
(45) Bauman, G. E.; McCracken, J. M.; White, T. J. Actuation of Liquid Crystalline Elastomers at or Below Ambient Temperature. *Angew Chem Int Ed* **2022**, *61* (28), e202202577. https://doi.org/10.1002/anie.202202577.
(46) McCracken, J. M.; Donovan, B. R.; Lynch, K. M.; White, T. J. Molecular Engineering of Mesogenic Constituents Within Liquid Crystalline Elastomers to Sharpen Thermotropic Actuation. *Adv Funct Materials* **2021**, *31* (16), 2100564. https://doi.org/10.1002/adfm.202100564.
(47) Shaha, R. K.; Torbati, A. H.; Frick, C. P. BODY-TEMPERATURE S HAPE-SHIFTING Liquid Crystal Elastomers. *J of Applied Polymer Sci* **2021**, *138* (14), 50136. https://doi.org/10.1002/app.50136.
(48) Sui, C.; Pu, J.; Chen, T.-H.; Liang, J.; Lai, Y.-T.; Rao, Y.; Wu, R.; Han, Y.; Wang, K.; Li, X.; Viswanathan, V.; Hsu, P.-C. Dynamic Electrochromism for All-Season Radiative Thermoregulation. *Nat Sustain* **2023**, *6* (4), 428–437. https://doi.org/10.1038/s41893-022-01023-2.
(49) Tang, K.; Dong, K.; Li, J.; Gordon, M. P.; Reichertz, F. G.; Kim, H.; Rho, Y.; Wang, Q.; Lin, C.-Y.; Grigoropoulos, C. P.; Javey, A.; Urban, J. J.; Yao, J.; Levinson, R.; Wu, J. Temperature-Adaptive Radiative Coating for All-Season Household Thermal Regulation. *Science* **2021**, *374* (6574), 1504–1509. https://doi.org/10.1126/science.abf7136.
(50) *Radiative human body cooling by nanoporous polyethylene textile | Science*. https://www.science.org/doi/10.1126/science.aaf5471 (accessed 2024-02-15).
(51) Wei, H.; Gu, J.; Ren, F.; Zhang, L.; Xu, G.; Wang, B.; Song, S.; Zhao, J.; Dou, S.; Li, Y. Smart Materials for Dynamic Thermal Radiation Regulation. *Small* **2021**, *17* (35), 2100446. https://doi.org/10.1002/smll.202100446.
(52) Ulpiani, G.; Ranzi, G.; Shah, K. W.; Feng, J.; Santamouris, M. On the Energy Modulation of Daytime Radiative Coolers: A Review on Infrared Emissivity Dynamic Switch against Overcooling. *Solar energy* **2020**, *209*, 278–301.
(53) Kats, M. A.; Sharma, D.; Lin, J.; Genevet, P.; Blanchard, R.; Yang, Z.; Qazilbash, M. M.; Basov, D. N.; Ramanathan, S.; Capasso, F. Ultra-Thin Perfect Absorber Employing a Tunable Phase Change Material. *Applied Physics Letters* **2012**, *101* (22), 221101. https://doi.org/10.1063/1.4767646.
(54) Zeng, S.; Shen, K.; Liu, Y.; Chooi, A. P.; Smith, A. T.; Zhai, S.; Chen, Z.; Sun, L. Dynamic Thermal Radiation Modulators via Mechanically Tunable Surface Emissivity. *Materials Today* **2021**, *45*, 44–53. https://doi.org/10.1016/j.mattod.2020.12.001.
(55) Schultz, P. H.; Hermalyn, B.; Colaprete, A.; Ennico, K.; Shirley, M.; Marshall, W. S. The LCROSS Cratering Experiment. *Science* **2010**, *330* (6003), 468–472. https://doi.org/10.1126/science.1187454.

(56) Xu, C.; Stiubianu, G. T.; Gorodetsky, A. A. Adaptive Infrared-Reflecting Systems Inspired by Cephalopods. *Science* **2018**, *359* (6383), 1495–1500. https://doi.org/10.1126/science.aar5191.
(57) Song, J.; Lu, L.; Li, B.; Zhang, B.; Hu, R.; Zhou, X.; Cheng, Q. Thermal Routing via Near-Field Radiative Heat Transfer. *International Journal of Heat and Mass Transfer* **2020**, *150*, 119346.
(58) Xuan, Y. An Overview of Micro/Nanoscaled Thermal Radiation and Its Applications. *Photonics and Nanostructures - Fundamentals and Applications* **2014**, *12* (2), 93–113. https://doi.org/10.1016/j.photonics.2014.02.003.
(59) Goetzler, W.; Guernsey, M.; Young, J.; Fujrman, J.; Abdelaziz, A. *The Future of Air Conditioning for Buildings*; Navigant Consulting, Burlington, MA (United States), 2016. https://www.osti.gov/biblio/1420235 (accessed 2024-01-22).
(60) Li, Z.; Chen, W. Progress in Dynamic Emissivity Regulation: Control Methods, Material Systems, and Applications. *Mater. Chem. Front.* **2021**, *5* (17), 6315–6332. https://doi.org/10.1039/D1QM00624J.
(61) Zhao, H.; Sun, Q.; Zhou, J.; Deng, X.; Cui, J. Switchable Cavitation in Silicone Coatings for Energy-Saving Cooling and Heating. *Advanced Materials* **2020**, *32* (29), 2000870. https://doi.org/10.1002/adma.202000870.
(62) Mandal, J.; Du, S.; Dontigny, M.; Zaghib, K.; Yu, N.; Yang, Y. Li4Ti5O12: A Visible-to-Infrared Broadband Electrochromic Material for Optical and Thermal Management. *Advanced Functional Materials* **2018**, *28* (36), 1802180. https://doi.org/10.1002/adfm.201802180.
(63) Zhang, X. A.; Yu, S.; Xu, B.; Li, M.; Peng, Z.; Wang, Y.; Deng, S.; Wu, X.; Wu, Z.; Ouyang, M.; Wang, Y. Dynamic Gating of Infrared Radiation in a Textile. *Science* **2019**, *363* (6427), 619–623. https://doi.org/10.1126/science.aau1217.
(64) Lu, L.; Wu, Z.; Ji, C.; Song, M.; Feng, H.; Ma, X.; Jiang, Y. Effect of Fe Doping on Thermochromic Properties of VO2 Films. *J Mater Sci: Mater Electron* **2018**, *29* (7), 5501–5508. https://doi.org/10.1007/s10854-018-8518-1.
(65) Athanasopoulos, N.; Siakavellas, N. J. Programmable Thermal Emissivity Structures Based on Bioinspired Self-Shape Materials. *Sci Rep* **2015**, *5* (1), 17682. https://doi.org/10.1038/srep17682.
(66) Paik, T.; Hong, S.-H.; Gaulding, E. A.; Caglayan, H.; Gordon, T. R.; Engheta, N.; Kagan, C. R.; Murray, C. B. Solution-Processed Phase-Change VO_2 Metamaterials from Colloidal Vanadium Oxide (VO_x) Nanocrystals. *ACS Nano* **2014**, *8* (1), 797–806. https://doi.org/10.1021/nn4054446.
(67) Ohm, C.; Brehmer, M.; Zentel, R. Liquid Crystalline Elastomers as Actuators and Sensors. *Advanced Materials* **2010**, *22* (31), 3366–3387. https://doi.org/10.1002/adma.200904059.
(68) Wang, Y.; He, Q.; Wang, Z.; Zhang, S.; Li, C.; Wang, Z.; Park, Y.-L.; Cai, S. Liquid Crystal Elastomer Based Dexterous Artificial Motor Unit. *Advanced Materials* **2023**, *35* (17), 2211283. https://doi.org/10.1002/adma.202211283.
(69) Berszakiewicz, A.; Kasperczyk, J.; Sieroń, A.; Krasiński, Z.; Cholewka, A.; Stanek, A. The Effect of Compression Therapy on Quality of Life in Patients with Chronic Venous Disease: A Comparative 6-Month Study. *pdia* **2021**, *38* (3), 389–395. https://doi.org/10.5114/ada.2020.92277.
(70) Zarchi, K.; Jemec, G. B. E. Delivery of Compression Therapy for Venous Leg Ulcers. *JAMA Dermatol* **2014**, *150* (7), 730. https://doi.org/10.1001/jamadermatol.2013.7962.

(71) Todd, M. Compression Bandaging: Types and Skills Used in Practical Application. *Br J Nurs* **2011**, *20* (11), 681–687. https://doi.org/10.12968/bjon.2011.20.11.681.
(72) Webb, E.; Neeman, T.; Bowden, F. J.; Gaida, J.; Mumford, V.; Bissett, B. Compression Therapy to Prevent Recurrent Cellulitis of the Leg. *N Engl J Med* **2020**, *383* (7), 630–639. https://doi.org/10.1056/NEJMoa1917197.
(73) Keller, A.; Müller, M. L.; Calow, T.; Kern, I. K.; Schumann, H. Bandage Pressure Measurement and Training: Simple Interventions to Improve Efficacy in Compression Bandaging. *International Wound Journal* **2009**, *6* (5), 324–330. https://doi.org/10.1111/j.1742-481X.2009.00621.x.
(74) Mosti, G.; Cavezzi, A.; Partsch, H.; Urso, S.; Campana, F. Adjustable Velcro® Compression Devices Are More Effective than Inelastic Bandages in Reducing Venous Edema in the Initial Treatment Phase: A Randomized Controlled Trial. *European Journal of Vascular and Endovascular Surgery* **2015**, *50* (3), 368–374. https://doi.org/10.1016/j.ejvs.2015.05.014.
(75) Mosti, G.; Picerni, P.; Partsch, H. Compression Stockings with Moderate Pressure Are Able to Reduce Chronic Leg Oedema. *Phlebology* **2012**, *27* (6), 289–296. https://doi.org/10.1258/phleb.2011.011038.
(76) Kumar, B.; Das, A.; Alagirusamy, R. Study on Interface Pressure Generated by a Bandage Using *in Vitro* Pressure Measurement System. *Journal of the Textile Institute* **2013**, *104* (12), 1374–1383. https://doi.org/10.1080/00405000.2013.807020.
(77) Feldman, J. L.; Stout, N. L.; Wanchai, A.; Stewart, B. R.; Cormier, J. N.; Armer, J. M. Intermittent Pneumatic Compression Therapy: A Systematic Review. *Lymphology* **2012**, *45* (1), 13–25.
(78) Morris, R. J.; Woodcock, J. P. Intermittent Pneumatic Compression or Graduated Compression Stockings for Deep Vein Thrombosis Prophylaxis?: A Systematic Review of Direct Clinical Comparisons. *Annals of Surgery* **2010**, *251* (3), 393–396. https://doi.org/10.1097/SLA.0b013e3181b5d61c.
(79) Hakala, T.; Puolakka, A.; Nousiainen, P.; Vuorela, T.; Vanhala, J. Application of Air Bladders for Medical Compression Hosieries. *Textile Research Journal* **2018**, *88* (19), 2169–2181. https://doi.org/10.1177/0040517517716907.
(80) Rahimi, M.; Blaber, A. P.; Menon, C. Motorized Adaptive Compression System for Enhancing Venous Return: A Feasibility Study on Healthy Individuals. *Medical Engineering & Physics* **2017**, *50*, 65–74. https://doi.org/10.1016/j.medengphy.2017.10.005.
(81) Yang, S. T.; Ryu, J. W.; Park, S.-H.; Lee, Y. B.; Koo, S. H.; Park, Y.-L.; Lee, G. An Active Compression Sleeve with Variable Pressure Levels Using a Wire-Fabric Mechanism and a Soft Sensor. *Smart Mater. Struct.* **2019**, *28* (11), 114002. https://doi.org/10.1088/1361-665X/ab3f56.
(82) Pourazadi, S.; Ahmadi, S.; Menon, C. Towards the Development of Active Compression Bandages Using Dielectric Elastomer Actuators. *Smart Mater. Struct.* **2014**, *23* (6), 065007. https://doi.org/10.1088/0964-1726/23/6/065007.
(83) Ross, L. T. Intelligent Compression Wrap. US11154453B2, October 26, 2021. https://patents.google.com/patent/US11154453B2/en (accessed 2024-04-29).
(84) Kumar, B.; Hu, J.; Pan, N. Smart Medical Stocking Using Memory Polymer for Chronic Venous Disorders. *Biomaterials* **2016**, *75*, 174–181. https://doi.org/10.1016/j.biomaterials.2015.10.032.

(85) Ahmad, M.; Luo, J.; Miraftab, M. Feasibility Study of Polyurethane Shape-Memory Polymer Actuators for Pressure Bandage Application. *Science and Technology of Advanced Materials* **2012**, *13* (1), 015006. https://doi.org/10.1088/1468-6996/13/1/015006.
(86) Kumar, B.; Hu, J.; Pan, N.; Narayana, H. A Smart Orthopedic Compression Device Based on a Polymeric Stress Memory Actuator. *Materials & Design* **2016**, *97*, 222–229. https://doi.org/10.1016/j.matdes.2016.02.092.
(87) Narayana, H.; Hu, J.; Kumar, B.; Shang, S.; Han, J.; Liu, P.; Lin, T.; Ji, F.; Zhu, Y. Stress-Memory Polymeric Filaments for Advanced Compression Therapy. *J. Mater. Chem. B* **2017**, *5* (10), 1905–1916. https://doi.org/10.1039/C6TB03354G.
(88) Narayana, H.; Hu, J.; Kumar, B.; Shang, S.; Ying, M.; Young, R. J. Designing of Advanced Smart Medical Stocking Using Stress-Memory Polymeric Filaments for Pressure Control and Massaging. *Materials Science and Engineering: C* **2018**, *91*, 263–273. https://doi.org/10.1016/j.msec.2018.05.026.
(89) Alavi, A.; Sibbald, R. G.; Phillips, T. J.; Miller, O. F.; Margolis, D. J.; Marston, W.; Woo, K.; Romanelli, M.; Kirsner, R. S. What's New: Management of Venous Leg Ulcers. *Journal of the American Academy of Dermatology* **2016**, *74* (4), 643–664. https://doi.org/10.1016/j.jaad.2015.03.059.
(90) Jovanović, T.; Penava, Ž.; Vrljičak, Z. Impact of the Elastane Percentage on the Elastic Properties of Knitted Fabrics under Cyclic Loading. *Materials* **2022**, *15* (19), 6512. https://doi.org/10.3390/ma15196512.
(91) Murphree, R. W. Impairments in Skin Integrity. *Nursing Clinics of North America* **2017**, *52* (3), 405–417. https://doi.org/10.1016/j.cnur.2017.04.008.
(92) *Nutrition and Functional Foods for Healthy Aging*; Watson, R. R., Ed.; Academic Press: London San Diego Cambridge Oxford, 2017.
(93) Berliner, E.; Ozbilgin, B.; Zarin, D. A. A Systematic Review of Pneumatic Compression for Treatment of Chronic Venous Insufficiency and Venous Ulcers. *Journal of Vascular Surgery* **2003**, *37* (3), 539–544. https://doi.org/10.1067/mva.2003.103.
(94) Wienert, V.; Sick, H.; zur Mühlen, J. [Local thermal stress tolerance of human skin]. *Anasth Intensivther Notfallmed* **1983**, *18* (2), 88–90.
(95) Coelho Rezende, G.; O'Flynn, B.; O'Mahony, C. Smart Compression Therapy Devices for Treatment of Venous Leg Ulcers: A Review. *Adv Healthcare Materials* **2022**, *11* (17), 2200710. https://doi.org/10.1002/adhm.202200710.

Acknowledgements

Chapter 4, in full, is a reprint of the material as it appears in “Liquid crystal elastomer for smart compression therapy”, submitted, by Gaoweiang Dong, Fangchen Zhao, Zongyu Gao, Shengqiang Cai. The dissertation author was the primary investigator and first author of this paper.

Chapter 5 Conclusion

5.1 Summary of the dissertation

Stimuli-responsive polymers have been intensively explored to broaden the scope of actuating devices, that were traditionally contracted with rigid components. Herein, we design and fabricate magnetic-responsive vitrimer-based and thermal-responsive LCE-based actuating devices for soft robotics, thermal management, and compression therapy. It was clearly shown that the actuating devices we developed filled in the literature lap and demonstrated the advantages of using stimuli-responsive polymers as the foundation of actuating devices. The main results of each chapter are summarized as follows:

In this study, we developed MV-based soft robots capable of drastic reconfigurations. The reaction activity of the dynamic covalent bonds exchange within the MV increases at higher temperatures, allowing the soft robot to undergo significant and irreversible alterations when subjected to an applied magnetic field. This ability enables the MV-based soft robot to navigate through confined spaces effectively. Additionally, by leveraging laser-induced local heating and an external magnetic field, precise control over the robot's shape change is achieved. Furthermore, the self-healing capability of MV without any external physical contact is enabled by incorporating the magnetic particles and employing the dynamic bonds exchange reaction. At room temperature, the MV behaves similarly to a standard elastomer, facilitating rapid catching, releasing, and locomotion capabilities for the MV-based soft robotic gripper.

In chapter 3, we systematically investigate the design, functionality, and thermal regulation potential of the Au-LCE thermal modulator, demonstrating an innovative approach to

adaptable thermal management. It has been shown that the Au-LCE modulator can efficiently alternate between "low thermal resistance" and "high thermal resistance" states in reaction to changes in environmental temperature. This capability is made possible by its unique material composition and structural design. The reversible transition of the Au-LCE, induced by the formation of microcracks in the gold layer above the nematic-isotropic transition temperature and the creation of insulating air pockets below it, highlights the modulator's dynamic adaptation of its thermal properties. Additionally, the modulator's flexibility, combined with its fixed device dimensions, extends its utility across diverse surface configurations. These findings underscore the potential of the Au-LCE thermal modulator in a wide range of applications, from energy-efficient building materials to wearable technology necessitating active temperature regulation.

In chapter 4, we effectively tackled the challenges of traditional static compression and intelligent dynamic compression therapy by employing LCE as a viable solution, given its distinctive mechanical and thermomechanical attributes. Firstly, we developed a polydomain LCE incorporated with PEGDA into the polymer network as a flexible backbone. This resulted in a polydomain LCE with stress plateau, minimal hysteresis, and superelasticity. These attributes allow for the accommodation of application errors and various limb sizes, minimal pressure drop during leg deswelling, and excellent reusability, respectively. Additionally, the polydomain exhibits negligible stress relaxation and strong repeatability across over 1000 loading cycles to 30% strain, ensuring consistent and prolonged interfacial pressure from the LCE static stocking. Secondly, we introduced monodomain LCE to dynamic compression therapy, leveraging its reversible thermal actuation properties for therapeutic benefits. The nematic-isotropic phase transition of LCE enables the material to exert sufficient actuation stress

around the leg when heated slightly above human skin temperature. Minimal stress relaxation and robust cyclability of over 1000 loading cycles to 6% strain underscore the material's durability. The embedded heater was designed and characterized to ensure uniform temperature distribution and durability. By sandwiching the heating element between two LCE sheets, the LCE dynamic stocking can generate interfacial pressure ranging from 20 to 60 mmHg with a temperature increase from 33 to 38 °C over 1000 cycles. Furthermore, we demonstrated that a controlled pressure profile can be attained using pressure feedback control. Finally, we fabricated an untethered LCE compression device. The wearable compression device with a PCS module, fabric, and Velcro straps, can effectively apply up to 43 mmHg of pressure to the human leg over 20 cycles. With a single battery charge, the device supports continuous intermittent pressure cycles for approximately four hours and remains highly portable.

5.2 Outlook for future work

For the magnetic-responsive vitrimer-based soft robots, several challenges exist, potentially limiting the application scope of these robots. While the magnetic vitrimer can be effectively controlled under an applied magnetic gradient, a notable limitation arises from the requirement for the magnetic field source to be in proximity to the robot. This limitation stems from the intrinsic property of magnetic-responsive polymers, where the magnetic field strength diminishes significantly over distance. Future endeavors may focus on developing more robust and controllable magnetic field sources to enhance the actuation capabilities of magnetic-responsive robots.

For the thermal-responsive LCE-based devices, the energy efficiency of LCEs remains relatively low (<1%) compared to other actuating mechanisms such as motors. This challenge could potentially be addressed by optimizing the thermal management of the device. Additionally, these devices typically rely on natural convection in air for cooling, resulting in long cooling times, often several minutes, depending on the size of the LCE. Future research may concentrate on reducing the cooling time through design enhancements aimed at increasing heat conduction or convection. Alternatively, employing active cooling methods such as thermoelectric devices could present a viable solution.